Photothermal studies of single molecules and gold nanoparticles : vapor nanobubbles and conjugated polymers

Hou, L.

Photothermal Studies of Single Molecules and Gold Nanoparticles: Vapor Nanobubbles and Conjugated Polymers

Photothermal Studies of Single Molecules and Gold Nanoparticles: Vapor Nanobubbles and Conjugated Polymers

PROEFSCHRIFT

ter verkrijging van
de graad van Doctor aan de Universiteit Leiden,
op gezag van de Rector Magnificus prof.mr. C. J. J. M. Stolker,
volgens besluit van het College voor Promoties
te verdedigen op dinsdag 14 juni 2016
klokke 10:00 uur

door

Lei HOU

geboren te Liaoning, China
in 1987

Promotor:	Prof. dr. M. A. G. J. Orrit	(Universiteit Leiden)
Promotiecommissie:	Prof. dr. D. Lohse	(Universiteit Twente)
	Prof. dr. F. Cichos	(Universität Leipzig)
	Prof. dr. E. J. J. Groenen	(Universiteit Leiden)
	Prof. dr. E. R. Eliel	(Universiteit Leiden)
	Prof. dr. M. van Hecke	(Universiteit Leiden)
	Prof. dr. T. Schmidt	(Universiteit Leiden)

Casimir PhD series, Delft-Leiden, 2016-15

ISBN 978-90-8593-257-4

An electronic version of this thesis can be found at the Leiden University Repository: `http://openaccess.Leidenuniv.nl/`.

The work reported in this thesis was carried out at the 'Leids Instituut voor Onderzoek in de Natuurkunde (LION)'. Financial support of China Scholarship Council is kindly acknowledged.

To my family

"...I seem to have been only like a boy playing on the seashore, and diverting myself in now and then finding a smoother pebble or a prettier shell than ordinary, whilst the great ocean of truth lay all undiscovered before me."
— ISAAC NEWTON

Contents

1

Introduction

In this thesis, we report properties and dynamics of vapor nanobubbles in liquid (first-order phase transition) around a laser-heated single gold nanoparticle (plasmon-mediated vapor nanobubbles), and we measure the absorption and emission of single conjugated polymer molecules poly[2- methoxy- 5 -(2-ethylhexyloxy)-1,4 - phenylenevinylene] (MEH-PPV) using near-critical xenon (second-order phase transition) to enhance the absorption signal. In this chapter, we will give an overview and motivation of our research and outline the contents of this thesis.

1.1. First-order and second-order phase transitions

In our daily life, phase transitions of water are observed everywhere: liquid water boils into vapor in the saucepan; frost forms at the surface of a window in a cold winter. If you look at the phase diagram of water as shown in Fig.1.1, phase transitions take place at different temperatures and pressures between adjacent regions in the diagram. The curve between liquid and vapor in the diagram is the saturation curve where liquid and vapor phases coexist. Normal boiling of water happens when the liquid is heated up at ambient pressure and crosses the saturation curve along the horizontal line at $p = 1$bar. We can also find the critical point of water above which liquid and vapor phases are not distinguishable, and a single phase supercritical water forms. People use "thermodynamic state functions" to describe the thermodynamics of phase transitions. For instance, the internal energy of a system U is a state function $U(S,V)$ where S is the entropy, V is the volume. Other common thermodynamic state functions include the enthalpy $H(S,P) = U + pV$, the Gibbs potential or Gibbs

free energy $G(T,P) = H - TS$ (T is the temperature), and the Helmholtz potential or Helmholtz free energy $F(T,V) = U - TS$. In the transformation of two phases such as from liquid to vapor, there often is finite discontinuity in the first derivative of the Gibbs potential $G(T,P)$ ($\partial G/\partial T = -S, \partial G/\partial P = V$) [1]. This process is called a first-order phase transition. Obviously the first-order transition is accompanied with a discontinuity in entropy and exchange of latent heat. Correspondingly, the second-order phase transition refers to the continuity in the first derivative of the Gibbs potential and discontinuity in the second-order derivative with respect to an external variable such as temperature or pressure. Above the critical point, one can convert liquid to vapor or vice versa continuously without crossing the coexistence curve. An important feature of a second-order phase transition is that response functions such as the heat capacity and the compressibility diverge at the critical point. This effect causes large fluctuations in the density in response to a little change of temperature and pressure, and can be useful in some circumstances. We will discuss the first-order transition of water at nanometer scale, which is the vapor nanobubbles' formation around a nano-size absorber such as a gold nanoparticle in Chapters 2, 3 and 4. We utilize the second-order transition of xenon to enhance the photothermal contrast (absorption signal) of single conjugated polymer molecules, which will be discussed in Chapters 5 and 6.

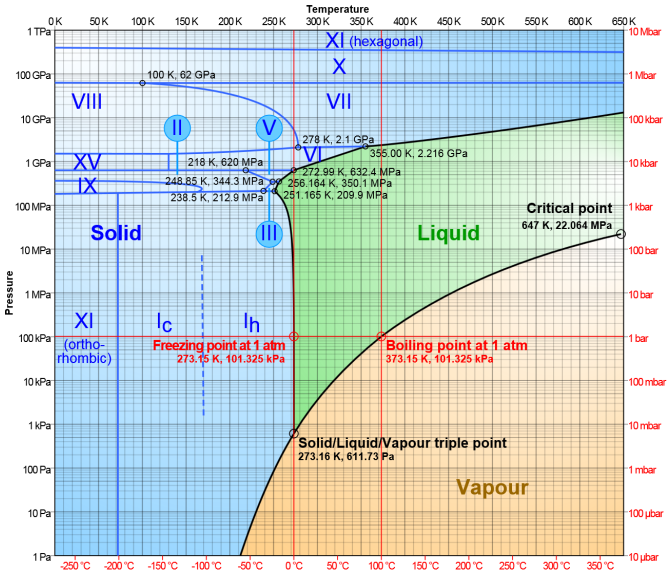

Figure 1.1: Pressure-temperature phase diagram of water [2]. The Roman numerals indicate various ice phases.

1.2. Vapor nanobubbles and applications

Properties of bubbles in a liquid with different sizes, from centimeters to nanometers, and different contents (dissolved gas or vapor) have been extensively studied over the past years [3–5], and research in this field remains active nowadays. This is not only because bubbles show complex physical behaviors (such as sonoluminescence and shock-wave release), but they also are potentially useful or detrimental for various applications (for cleaning and ship-propeller erosion through cavitation). In particular, we are interested in the vapor nanobubbles that arise upon crossing the saturation line of liquid-vapor coexistence and with a size of typically a few tens to hundreds of nanometers. Due to the confinement of temperature and pressure at nanometer scales, high compressibility and large optical scattering cross section, vapor nanobubbles are believed to be useful in many applications such as photothermal therapy [6], drug delivery [7], enhancing catalytic reactions and enhancing coupling between optical and acoustic waves [8]. For example, Lukianova-Hleb *et al.* have showed that by generating small vapor nanobubbles specifically in malaria parasites using laser pulses, one can diagnose and get rid of infected blood red cells in a patient's body without any labeling and invasive treatment [9]. Goy *et al.* have shown that generation of vapor nanobubbles improves the resolution of photoacoustic imaging by a factor of two [10]. Adleman *et al.* demonstrated that vapor bubbles generated by plasmonic heating facilitate catalytic reactions [11].

Since vapor nanobubbles are so useful in many circumstances, the main motivation of this thesis is to study the physical properties and dynamics of such tiny vapor bubbles in order to gain a better understanding of their nature, as well as to seek a way to control and make use of them for applications. Because of their small size, vapor nanobubbles need to overcome a large Laplace pressure in order to nucleate and grow. Thus a bubble requires more heat and energy to form at nanometer scale, and temperature and pressure will shift to much higher values than at ambient conditions. Classical nucleation theory and experimental observation point out that when the liquid is heated up to a high enough temperature, boiling and phase transition show explosive nature [12]. The small nanometer size also means that the time scale for transient vapor nanobubbles becomes very short [13]. All these factors add up and make the study of vapor nanobubbles quite challenging. In this thesis, we aim for the answer to a number of key questions regarding the physical properties of vapor nanobubbles such as temperature and pressure upon bubble formation; whether vapor nanobubbles are in equilibrium with the surrounding liquid or highly dynamical; how vapor nanobubbles interact with local surroundings such as nearby interfaces and how vapor nanobubbles behave during for-

mation and collapse on different time scales. Since a gold nanoparticle is an efficient local-heat absorber under optical excitation, we constrain our discussion to the plasmon-mediated steam nanobubbles that form in a liquid around an optically heated single gold nanoparticle. The advantage of an all-optical detection is its speed, sensitivity and non-invasive character.

1.3. Theoretical models to describe vapor bubble physics

In order to gain a better understanding of the physics of vapor nanobubbles and to explain existing results, a number of models and simulation methods have been proposed and applied to bubble studies [3]. Here we briefly introduce some of the common modeling methods used in the theoretical study of bubble dynamics, covering both continuum approaches and numerical simulations.

1.3.1. Rayleigh-Plesset equation

In 1917, Rayleigh derived an equation to describe the problem of cavitation and bubble dynamics with spherical geometry in an infinite liquid [14]. In his model, he considered the collapse of a void cavity in an infinite liquid, neglecting the surface tension and liquid viscosity presumably because only large bubbles were considered at that time. He also assumed that the liquid is incompressible and pressure far away from the bubble keeps constant. The equation is written as:

$$R(t)\frac{d^2R(t)}{dt^2}+\frac{3}{2}\left[\frac{dR(t)}{dt}\right]^2=\frac{1}{\rho}\{P[R(t)]-P_\infty\} \tag{1.1}$$

where $R(t)$ is the bubble radius; the pressure in the bubble is $P(R)$; the pressure at the place of infinity in the liquid is P_∞, and ρ is the liquid density. Later Plesset modified Rayleigh's equation, taking into account the surface tension and liquid viscosity, and rewrote the Rayleigh equation and got the well-known "Rayleigh-Plesset" equation, which is widely used in cavitation modeling and bubble dynamics simulations [15]. It is written as:

$$R(t)\frac{d^2R(t)}{dt^2}+\frac{3}{2}\left[\frac{dR(t)}{dt}\right]^2=\frac{1}{\rho}\left\{P(t)-P_\infty(t)-\frac{2\gamma}{R(t)}-\frac{4\mu}{R(t)}\frac{dR(t)}{dt}\right\} \tag{1.2}$$

The terms on the right-hand side of the equation 1.2 are the bubble internal pressure, the pressure at infinity, the Laplace pressure (γ is the surface tension) and μ is the liquid viscosity, respectively. In this equation, the liquid is still assumed to be incompressible. The Rayleigh-Plesset equation can be derived from a continuum theory [3].

Since then, the Rayleigh-Plesset equation has been applied to many problems regarding the temporal evolution of bubble size and has given satisfactory results on a number of bubble phenomena such as bubble bouncing after collapse [16], the emission of acoustic waves after a bubble's collapse, bubble oscillation in the acoustic field [4], and the natural oscillation frequency of a gas bubble, also known as the "Minnaert" frequency [17]. When modeling the cavitation and vapor bubble dynamics, compressibility of the liquid, mass and heat transfers, momentum and energy conservation should be considered as well. Nevertheless, modeling with the Rayleigh-Plesset equation seems quite successful in explaining many experimental data [18].

1.3.2. Gilmore equation

Another modeling approach to bubble dynamics was introduced by Gilmore in 1952, based on the hypothesis of Kirkwood and Bethe [19]. In his expression, Gilmore includes the effects of surface tension, viscosity, and the second power of the ratio of bubble wall velocity to the sound velocity (he called higher order compressibility terms), because compressibility of the liquid becomes significant and non-negligible when bubble wall velocity gets close to the speed of sound during bubble collapse. The equation is written as follows:

$$R\frac{d^2R}{dt^2}\left(1-\frac{1}{C}\frac{dR}{dt}\right)+\frac{3}{2}\left(\frac{dR}{dt}\right)^2\left(1-\frac{1}{3C}\frac{dR}{dt}\right)=H\left(1+\frac{1}{C}\frac{dR}{dt}\right)+\frac{R}{C}\left(1-\frac{1}{C}\frac{dR}{dt}\right)\frac{dH}{dt} \tag{1.3}$$

where H and C are the specific enthalpy of the surrounding liquid and the sound velocity at the bubble-liquid interface. Normally an equation of state is also needed to relate H and C with the pressure at the bubble wall, which is essentially a function of bubble radius and time. The Gilmore equation can be used for bubble dynamic modeling, but often it is used in the description of phenomena related to under-water explosions and in the calculation of radiated acoustic energy [20]. Note that the modeling of acoustic radiation is not restricted to the Gilmore equation, and it can be incorporated into Rayleigh-Plesset equation as well [21].

1.3.3. Molecular dynamics simulation

With the increase of computing power, molecular dynamics (MD) simulation can be exploited to simulate the bubble behavior and to predict real measurements. The idea behind MD is straightforward: given a number of interacting molecules, their interatomic potentials and certain boundary conditions, the trajectories of molecules can be solved numerically using the classical Newton

law of motion. The overall response can be obtained by integrating all equations [22]. For example, MD simulation has been applied to bubbles in a confined nano-channel to explain the nanobubble nucleation process [23]. MD simulation has its own limitations. It heavily depends on the parameters set in the simulation, and the number of molecules cannot be arbitrarily set; in some potential models, dielectric properties of the environment are not properly considered [22].

1.4. Methods to generate and probe vapor nanobubbles

Over the past decades, many techniques and methods have been applied to the study of vapor nanobubbles. In the following, we will briefly introduce some common methods used in research for generating and detecting vapor bubbles in liquid. In general, the methods used to form bubbles in liquid include: 1) applying negative pressure to the liquid at constant temperature with acoustic waves; 2) electric discharging in the liquid; 3) focusing a laser beam into the liquid with or without absorbing ions or nanoparticles. Correspondingly, the detection of bubbles can be achieved by: 1) monitoring the response of acoustic transducers; 2) monitoring a conductance change across a device; 3) monitoring wide-field optical image or scattering of bubbles. Different combinations of these methods are also widely used in the vapor bubble research. Other techniques such as AFM, in principle, can be used to study bubble's size and morphology. But the time resolution of AFM seems too slow to follow the dynamics of transient vapor bubbles, so we will not discuss it any further. For simplicity, we classify all these methods into three types: acoustical, electrical and optical, as shown in the schemes of Fig.1.2.

Acoustical: vapor bubbles can form in a liquid when the liquid pressure falls below the vapor (saturation) pressure. This process is normally called "cavitation" in the literature [3], even though there is no fundamental physical difference when it is compared with "boiling" where the temperature of liquid is raised above the (saturated) vapor temperature. When the liquid is subjected to a negative acoustic pressure which stretches liquid molecules apart, a nucleation can form at a "weak" site and develop into a bubble. Acoustic cavitation and associated bubbles are widely used in biomedical applications such as drug delivery and ultrasound imaging [24]. A common feature accompanying bubble's formation and collapse is the release of acoustic waves. The pressure waves released by bubbles can be picked up by some acoustic transducers and further amplified to produce a typical bubble signal [25]. The drawback of acoustic detection is the slow response of acoustic detectors. Most acoustic transducers have a resonant frequency around 10 MHz where sensitivity is

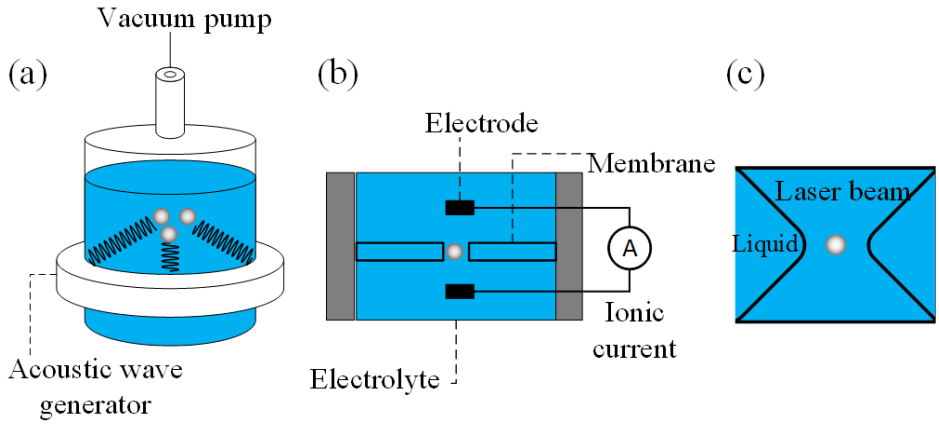

Figure 1.2: Schemes of methods used in the vapor bubble studies. a) acoustical; b) electrical; c) optical methods.

optimal. But the transient time of vapor nanobubbles can be as short as a few nanoseconds [26]. Thus, acoustic detectors are not fast enough to follow the dynamics of vapor nanobubbles.

Electrical: another common method of generating vapor bubbles in a liquid is to discharge a capacitance into a circuit containing two electrodes close to each other in an electrolyte. Vapor bubbles can form at a point of low conductance because of the high Joule heating of the electrolyte when a high current pulse is applied to the electrodes [27]. Nanostructures such as nanopores made of silicon nitride can be used to further confine Joule heat in a small volume [28]. This method can be easily implemented in the lab and does not require expensive optics and lasers of the optical method. The main challenge of this method is the difficulty of putting electrodes at the desired sites. Detection of vapor bubbles can be achieved by monitoring the conductance of the electrolyte in the pore in real time with high time resolution, up to ns [28].

Optical: optical generation of nanobubbles in liquid can be done simply by focusing a laser beam into the solution. Depending on the delivered optical influence and physical mechanism, nanobubble formation can be classified into two types [29]: thermally induced vapor bubbles (the liquid is heated up to a temperature above the boiling temperature) and direct break-down of the liquid (liquid molecules are ionized and generate a hot plasma, which expands to form a bubble). Various nanoparticles, such as metallic nanoparticles [30–32], quantum dots [33, 34], core-shell hybrid nanostructures [35], and ions dissolved in the liquid [36] can be exploited to enhance the absorption of liquid at a specific wavelength and the heating efficiency. Pulsed laser sources give

rise to a high confinement of heat around the excited volume, whereas a continuous laser leads to a more extended steady-state temperature profile in the liquid [37]. In the latter situation, liquid superheating and explosive boiling are often involved [36].

Detection of optically generated vapor bubbles can be achieved by wide-field optical imaging [25] with a fast camera. For vapor nanobubbles, the size is beyond the optical diffraction limit. But we can study the vapor nanobubbles by looking at the scattering intensity of a probe laser beam with low intensity [25, 32], or by total internal reflection microscopy (TIRF) [38], or by looking at the shifts of the surface plasmon resonance (SPR) of gold nanoparticles if gold nanoparticles are used as local heat sources to form vapor bubbles, because the SPR is sensitive to the change in the local refractive index [39]. X-ray scattering can also be used to monitor the liquid-vapor transition and bubble dynamics because X-ray scattering is sensitive to changes in structure and interactions of molecules in matter [26].

In our research, we propose to generate and study vapor nanobubbles all optically with the high spatial resolution of photothermal microscopy and the high temporal resolution of pump-probe microscopy. We illuminate a single gold nanoparticle in a liquid with a wavelength in resonance with the absorption of the particle. Dynamics of vapor nanobubbles are monitored through the intensity change of a second beam with a different wavelength and relatively low power. The advantage of single particle measurements is that averaging is excluded and vapor nanobubbles can be studied under various conditions with good reproducibility. The advantages of an all-optical study are its fast response, high spatial and temporal sensitivity and the low invasiveness.

1.4.1. Photothermal microscopy

Photothermal microscopy is an indirect method for probing the non-radiative energy dissipation of an object under excitation [40]. Normally two continuous laser beams are involved in such an experiment. The heating beam is intensity-modulated at high frequency, and used to heat up the object and create a temperature and refractive index profile in its nearby medium [41]. The probe beam, which is spatially overlapped with the heating beam, is scattered by the local index gradient and interferes with a reference field, such as a reflection of the incident probe beam by a nearby interface or the transmitted probe beam. The interfering signal is then picked up by a photodiode, and the small changes in probe intensity are isolated by demodulating the signal with a lock-in amplifier. The photothermal signal is proportional to the heating and probe powers, the absorption cross section of the small object, and the thermal

properties of the transducing medium. It can be written as [42]:

$$S \approx \frac{1}{\pi\omega_0} n \left.\frac{\partial n}{\partial T}\right|_p \frac{1}{C_p \lambda^2 \Omega} \frac{\sigma_{abs}}{A} P_{heat} P_{probe} \Delta t \tag{1.4}$$

From the above equation, we can see a number of ways that can further improve the photothermal signal [42]. For example by increasing both heating and probe powers, by matching the index of sample and substrate to reduce the laser noise, by integrating for longer times, by using a transducing medium with good thermal properties, and by putting an isolating layer to further confine the heat around the sample. It has been shown that photothermal microscopy has a sensitivity capable of probing 1.4 nm gold nanoparticles [43, 44] and single organic molecules [45]. The detected temperature change can be as small as 80 mK [42].

1.4.2. Time-resolved pump-probe spectroscopy

Time-resolved pump-probe spectroscopy exploits two synchronized short pulses with different wavelengths. The pump pulse is used as a trigger to excite the sample out of its equilibrium state; then the transient relaxation of excited species such as electrons is monitored with the probe pulse as a function of time through changes in the absorbance or transmittance of the sample. The time interval Δt between pump and probe pulses is controlled by varying the optical delay between these pulses with a linear mechanical stage. Then the "snapshots" and dynamics of excited species are recorded as a function of time delay. In the pump-probe spectroscopy, the time resolution is limited by the pulse width, provided no time jitter takes place between excitation and relaxation. Because the low signal to noise ratio in single-shot measurements with the pump-probe method, accumulation of many pulsed events is necessary, so that jitter leads to a loss of time resolution. Modulation of pump intensity at higher frequency and picking up of small variations in the probe intensity with a lock-in amplifier will remove the slow-varying backgrounds and thus significantly increase the signal to noise ratio and sensitivity of experiments. This technique has been widely used in studies such as electron-phonon coupling in metallic nanoparticles [46].

1.4.3. Optical contrast

Now we discuss the optical signals measured in photothermal microscopy and pump-probe spectroscopy. In both schemes, the total intensity detected by the

photodetector is given by the following equation if the heating beam is completely rejected from the detection [47]:

$$I = \left| E_{ref} + E_{sca} \right|^2 . \tag{1.5}$$

We write the complex reference field E_{ref} and the scattered field E_{sca} as:

$$E_{ref} = rE_0, \tag{1.6}$$

$$E_{sca} = sE_0 e^{i\varphi}, \tag{1.7}$$

where r, s are real quantities; E_0 is the complex incident electric field; φ is the phase difference between the reference field and the scattered field. Substituting Eq.1.6 and Eq.1.7 into Eq.1.5, we get the total intensity detected by the detector:

$$I = |E_0|^2 (r^2 + 2|r||s| cos\varphi + s^2). \tag{1.8}$$

For the small nano-objects considered here, the last term in Eq.1.8 (intensity scattered by the object) is much weaker than the strong reference intensity, and can be safely neglected. The first term is just a constant bright "background" and is removed by the lock-in detection. Then the contrast of detected signal mainly arises from the cross term of interference [48]. From this equation, we can see that the scattered field should be coherent with the reference field, and the spatial modes should be largely overlapped, otherwise the cross term will average to zero. The reference field can be implemented in different ways. For example, it can be the probe beam reflected by a nearby interface, the transmitted probe beam passing through the particle in the forward direction [49], an auxiliary beam in a differential interference contrast microscope (DIC) [44], in a Michelson interferometer [50], or in a common-path polarization interferometer [51]. If we assume that the total noise is shot-noise limited and proportional to the square root of the total number of photons on the detector, which is essentially the square root of the probe intensity, $\sqrt{r^2 |E_0|^2}$, the signal to noise ratio (SNR) becomes:

$$SNR = \frac{2|E_0|^2 |r||s| cos\varphi}{\sqrt{r^2 |E_0|^2}} = 2Re(E_{sca}), \tag{1.9}$$

which is actually independent of the reference field, as long as this field remains much stronger than the scattered field. This implies that the strength of the reference field can be arbitrarily tuned according to specific experimental conditions without losing signal to noise ratio.

1.5. Second-order phase transition and supercritical fluid

As mentioned at the beginning of this chapter, a second-order phase transition occurs at the critical point and a discontinuity in the second derivative of Gibbs' free energy is found. The phase transition between liquid and vapor phases takes place smoothly/continuously without crossing the saturation curve above the critical point. A supercritical fluid is a substance at a temperature and pressure above the critical point, where liquid and vapor phases cannot be distinguished anymore. At the critical point, the correlation length (which defines the characteristic distance where microscopic variables such as density start to differ from their initial values) and the time scale for molecular reorganization become infinite. Another interesting property of a critical fluid is that the singular behavior in the vicinity of the critical point is only characterized by a set of "critical exponents", regardless of the chemical components [52]. Close to the critical point, a supercritical fluid exhibits large fluctuations in quantities such as the density in response to small changes in temperature and pressure, thus making many properties of supercritical fluids finely tunable. For example, carbon dioxide is commonly used in industry as a supercritical fluid to extract, dissolve, and decompose substances [53].

1.6. Gold nanoparticle as a nanoabsorber

In order to increase the absorbing efficiency of the liquid for incident light and create localized vapor nanobubbles, we use gold nanoparticles (mainly spheres) in this thesis as the absorbing agent in liquid. The optical properties of gold nanoparticles have been extensively studied for many years [54]. Due to their superior photo-stability, large extinction cross section compared with organic molecules and biocompatibility, gold nanoparticles are used in numerous applications in many disciplines [55–59]. The optical properties of gold nanoparticles are related to the localized surface plasmon resonance (SPR), which is the collective oscillation motion of electrons in the conduction band of gold driven by an external electromagnetic field. The SPR often manifests itself by a resonance peak in the extinction (sum of absorption and scattering) spectrum. The resonance position depends on the size and shape of gold nanoparticles and on the refractive index of the surrounding medium. In the current study, gold nanoparticles are chosen as efficient light absorbers and localized heating sources because of the resonant absorption in the visible range, high thermal conductivity, very high bulk melting point and fast heating process within gold upon optical excitation. Phase transitions such as vapor bubble formation around gold nanoparticle can be further "amplified" by the shift of the SPR

in response to a refractive index change. Apart from that, gold nanoparticles can be anchored on the specific site of targets by surface functionalization. All these factors make gold nanoparticles excellent agents for the study of vapor nanobubbles.

1.7. Conjugated polymers

Conjugated polymers are one type of organic molecules consisting of many alternating double and single carbon-carbon bonds. Just as in a semiconductor, photon absorption or emission are associated to the transition of a delocalized π electron between the highest occupied and the lowest unoccupied molecular orbitals. Therefore, the optoelectronic properties of conjugated polymers resemble those of semiconducting materials. Conjugated polymers are widely used in organic light-emitting devices [60], thin-film transistors, and solar energy harvesting devices [61]. The optical properties of conjugated polymers strongly depend on their conformation and microscopic structure, which have been intensively studied with single-molecule fluorescence microscopy [62, 63]. Many factors influence the properties of conjugated polymers, including the distribution of molecular weights, the polarity of solvents used in the sample preparation, the sample annealing conditions, the embedding matrix and the spin-coating parameters, leading to very complex behavior. A direct measurement of the conformation of a single conjugated molecule seems challenging, if not impossible. However, a measurement of the heat dissipated by a molecule upon excitation can determine the number and orientation of absorbing monomer units, and therefore provide indirect information about the polymer's conformation. This will help us to evaluate the quantum yield of single conjugated molecules, thus to shed light on the conjugated polymers used in devices and applications.

1.8. Outline of this thesis

To facilitate the reading of this thesis, we list the main contents of each chapter:

Chapter 2: We provide a simple model for the thermo-dynamical analysis of a vapor nanobubble assuming the vapor nanobubble is in equilibrium with the surrounding liquid. We calculated the minimal temperature as well as the pressure for different sizes of vapor nanobubbles. We also estimated the optical power required to deliver into the system in order to form a vapor bubble around a continuous laser-heated gold nanosphere, and the optical signal change due to the presence of a vapor nanobubble. The information obtained

from this model paves the way for our experimental study.

Chapter 3: We experimentally investigated the dynamics of vapor nanobubbles in liquids around a continuous laser-heated gold nanosphere. A number of interesting phenomena were observed in our measurements, such as the instability of the nanobubble under constant heating, and the explosive and echo-triggered formations of nanobubbles. We characterized the behavior of nanobubbles and estimated the temperature, pressure and size of nanobubbles based on the optical signal.

Chapter 4: Combining time-resolved pump-probe spectroscopy and CW heating, we probed vapor nanobubbles around a single gold nanosphere with pico-second time resolution. We revealed the nanobubble evolution in the first nano-second after femto-second optical pulse excitation/triggering.

Chapter 5: We demonstrated a way to further enhance the photothermal contrast of weak absorbing nano-objects. We use xenon under supercritical phase to maximize dn/dT so that we can use much less power in order to get a good photothermal signal, compared with a normal liquid case. We characterize the enhancement factor, the dependency on modulation frequency, and compare the data with literature and with a common liquid, glycerol.

Chapter 6: We applied the enhanced photothermal technique to the simultaneous measurements of the absorption and emission of single conjugated MEH-PPV polymer molecules. We get useful information such as monomer numbers in a conjugated molecule and the apparent quantum yield of single polymer molecules.

2

Steady state of a vapor nanobubble in liquid around a continuously laser-heated gold nanoparticle

Abstract– *We provide a simple model of the thermodynamic properties of vapor nanobubbles in liquid around a continuously laser-heated gold nanosphere, assuming the system is under steady state. We calculate the minimal boiling temperature and pressure for different sizes of vapor nanobubbles, the optical power to be delivered into the system for vapor nanobubble formation, and the optical signal change due to the scattering by the bubble.*

Parts of this chapter have been published in New J. Phys. **17**, 013050 (2015) [30].

2.1. Introduction

Fluid dynamics and phase transitions have been extensively studied since the time of Gibbs [3]. They are both fundamentally important and practically useful. When temperature and pressure of a liquid reach and cross the coexistence saturation curve where two phases are in equilibrium, transformation from liquid to vapor can take place, and vapor bubbles can form in the liquid. In the phase diagram, there also exists a region where liquid and vapor can be in "metastable" states. The limit to which a metastable liquid can be superheated without boiling is called "liquid spinodal line", while the limit to which metastable vapor can be "subcooled" is called "vapor spinodal line" [36]. Superheated liquids are found to be extremely unstable, and homogeneous nucleation and explosive boiling are often observed [64]. The maximum superheating temperature measured experimentally is about 88-90% of the critical temperature, in good agreement with the temperature predicted by classical nucleation theory [12]. In this chapter, we will focus on the first-order phase transition from liquid to vapor and vapor bubble formation at the surface of a continuously laser-heated gold nanosphere. We assume that liquid and vapor are in equilibrium. We provide a simple model to describe the thermal properties of a vapor nanobubble under steady state.

2.2. The boiling temperature T_b as a function of bubble radius

Our system is described as follows, as is shown in the scheme Fig.2.1(a). A gold nanosphere is immersed in a liquid. A continuous-wave (CW) laser with a wavelength close to the absorption maximum of the gold nanosphere is focused on the gold particle. Due to the high optical absorption, the gold nanoparticle becomes hot and can bring the surrounding liquid to ebullition if the illumination power is high enough. Then, a vapor shell can form around the particle. We set out our discussions with a few assumptions. First, the vapor nanobubble has a spherical symmetry; Second, the vapor and liquid phases are in equilibrium; Third, thermal parameters of liquid and vapor are taken from their macroscopic values; Last, the thermal conductivity of gold is approximated as infinite. We assume that the radius of the vapor bubble is just equal to the radius of the gold nanoparticle. Under steady state, there is equilibrium between the vapor and the surrounding liquid. That is, the pressure inside the vapor bubble should be equal to the liquid pressure plus the Laplace pressure induced by the surface tension:

$$P_{vapor}(T) = P_0 + \frac{2\gamma(T)}{R_{bubble}} \tag{2.1}$$

P_0 = 1 atm is the ambient pressure. For two liquids, water and n-pentane, the temperature- dependent vapor pressure $P_{vapor}(T)$ and surface tension $\gamma(T)$ are plotted in Fig.2.1 (b) and (c). Data are taken from Ref.[65]. According to Eq.2.1, we get the minimum (critical) temperature required for the boiling as a function of the bubble/particle radius (the bubble size is just equal to the size of particle), as shown in Fig.2.1 (d). Below the critical temperature, there is no vapor bubble. The particle is surrounded by a temperature gradient of hot water. We call this steady state regime I. Above a critical temperature, we expect to reach a second steady state, regime II, with a steam bubble around the nanoparticle. Close to the critical temperature, we can see that the boiling temperature is significantly shifted to a higher value with respect to the boiling temperature at ambient pressure (For water, the normal boiling point is 373.12 K; for pentane, it is 309.21 K, as shown by the dashed lines in Fig.2.1 (d), due to the large Laplace pressure of small bubble sizes. Similarly, the critical pressure for vapor nanobubble formation can be calculated and is plotted in Figure 2.2. For small particles, diameter < 10 nm, the interface approaches the critical temperature (647 K for water, 469.8 K for n-pentane), and no clear interface appears anymore [66].

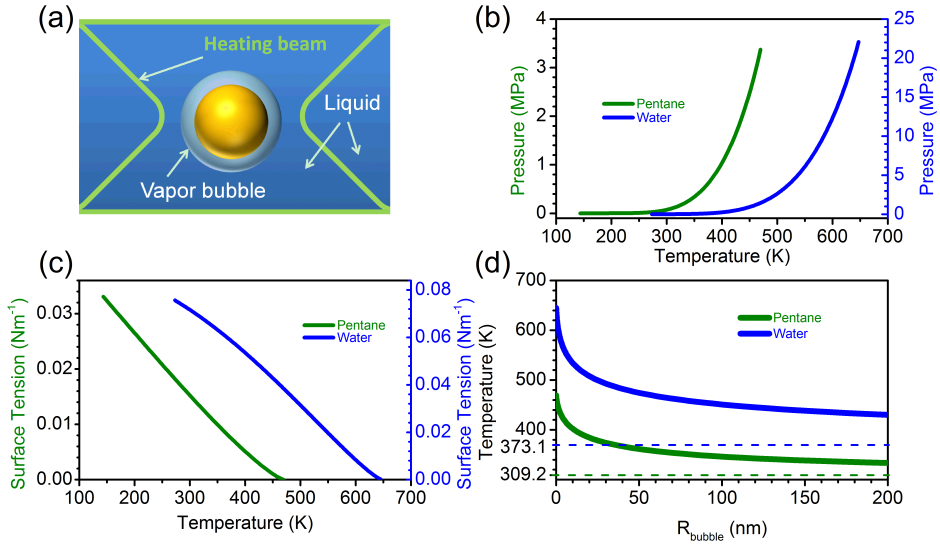

Figure 2.1: Phase diagram of a vapor nanobubble. (a): Scheme of the system under study; (b): Temperature-dependent pressure of the vapor phase at saturation for two different liquids, water and pentane; (c): Surface tensions of the two liquids at saturation as a function of temperature; (d): Minimum (critical) temperature to reach the boiling as a function of bubble/particle radius, assuming the size of the vapor bubble is just equal to the size of the particle.

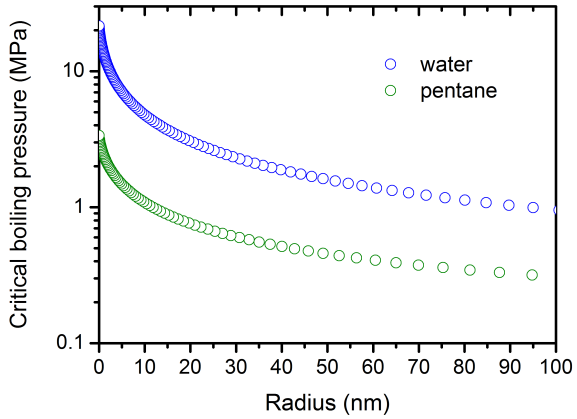

Figure 2.2: Critical boiling pressure for vapor nanobubble formation as a function of particle/bubble radius.

2.3. Temperature profiles under different absorbed powers

Under steady state, the temperature distribution can be calculated by solving the Poisson equation. We assume the temperature inside the gold particle to be homogeneous, because the thermal conductivity of gold is much higher than the thermal conductivities of liquid water and water vapor. Below the critical boiling temperature, there is no vapor bubble around the gold nanoparticle, the temperature distribution around a gold nanoparticle is written as follows [44, 67]:

$$T(r) = \begin{cases} T_0 + \dfrac{P_{abs}}{4\pi\kappa_l r_p} & \text{for} \quad r \le r_p \\ T_0 + \dfrac{P_{abs}}{4\pi\kappa_l r} & \text{for} \quad r > r_p \end{cases} \tag{2.2}$$

where κ_l is the thermal conductivity of the liquid, T_0 the ambient temperature and P_{abs} is the power absorbed by the gold nanoparticle. Using this equation, we can calculate the minimal (critical) power that is required to reach the boiling by setting the bubble radius equal to the particle radius and demanding that the bubble temperature is equal to the minimal (critical) temperature in Fig.2.1 (d). The results are shown in Fig.2.3. Above the critical temperature, a vapor bubble can form around the gold nanoparticle, and the thermodynamic properties of a vapor bubble are governed by the following two equations:

$$\begin{cases} p_0 + \dfrac{2\gamma(T_b)}{r_b} = p_{vap}(T_b) \\ T_b = T_0 + \dfrac{P_{abs}}{4\pi\kappa_l r_b} \end{cases} \tag{2.3}$$

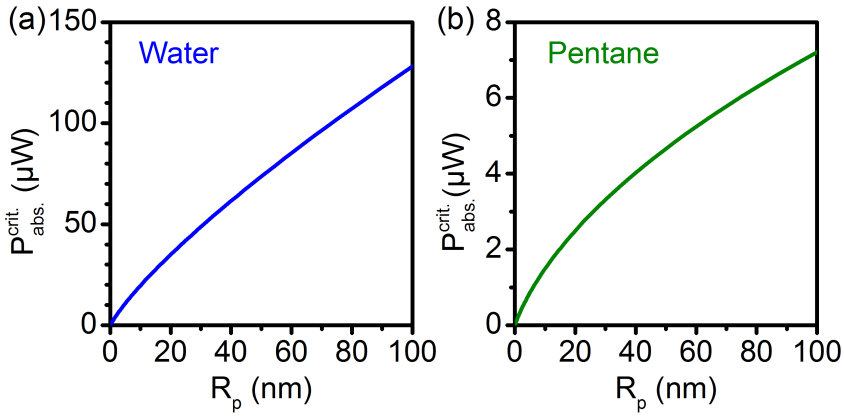

Figure 2.3: Minimal (critical) absorbed powers for the boiling as a function of particle radius, (a) in water; (b) in pentane.

where r_b is the radius of the vapor bubble, p_0 is the ambient pressure, $p_{vap}(T_b)$ is the temperature dependent vapor pressure, $\gamma(T_b)$ is the bubble-temperature dependent surface tension, and T_b is the temperature of the vapor bubble for vanishing thickness, the same as the minimum/critical boiling temperature.

The steady-state temperature profile when a vapor bubble forms around the particle under various absorbed powers is given by [30]:

$$T(r) = \begin{cases} T_0 + \dfrac{P_{abs}}{4\pi r_b}\left(\dfrac{1}{\kappa_l} - \dfrac{1}{\kappa_v}\right) + \dfrac{P_{abs}}{4\pi\kappa_v r_p} & \text{for} \quad r \le r_p \\ T_0 + \dfrac{P_{abs}}{4\pi r_b}\left(\dfrac{1}{\kappa_l} - \dfrac{1}{\kappa_v}\right) + \dfrac{P_{abs}}{4\pi\kappa_v r} & \text{for} \quad r_p \le r \le r_b \\ T_0 + \dfrac{P_{abs}}{4\pi\kappa_l r} & \text{for} \quad r \ge r_b \end{cases} \tag{2.4}$$

where the first line describes the temperature inside the gold particle, the second line describes the temperature in the vapor bubble and the third line describes the temperature outside the vapor bubble. In this equation κ_v is the thermal conductivity of the vapor, assumed to take its macroscopic value (the heat conduction in the thin high-pressure vapor shell reaches the Knudsen regime only at thicknesses less than 10 nm [68]). The thermal conductivities that were used in the calculations are given in table 2.1 and their slight temperature dependence was neglected. Figure 2.4 shows calculated temperature profiles for particles in water and pentane heated above or below the critical heating powers. At the critical power, the particle is surrounded by a hot liquid layer with temperature higher than the boiling point at ambient pressure. Thermal energy is thus stored in this hot liquid layer. Once the bubble forms, we can see

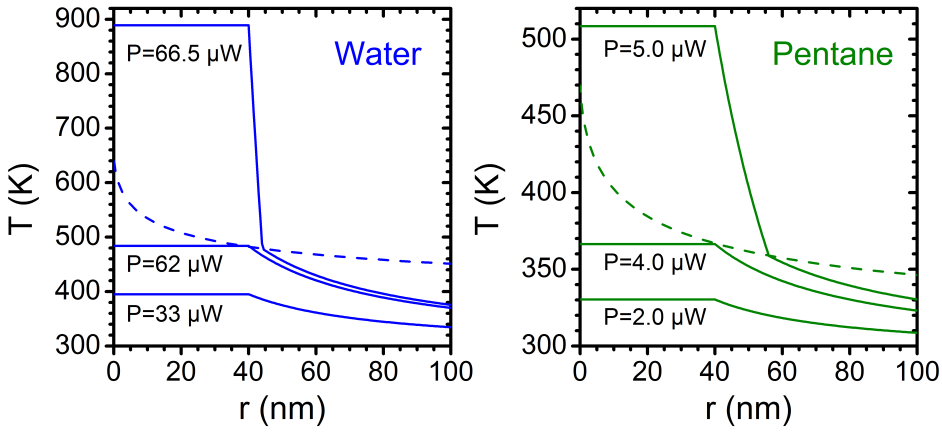

Figure 2.4: Temperature profiles around a gold nanosphere with 80 nm diameter under various absorbed powers in two liquids: (a) in water; (b) in pentane. The dashed curves in (a) and (b) are the temperatures of the boiling phase transition as a function of particle radius.

that the temperature of the nanoparticle rises by hundreds of Kelvin due to the poor thermal conductivity of the steam with respect to the liquid. This high temperature might degrade or cause surface melting of the nanoparticle. So the heating power should be carefully tuned in the experiment to ensure the reproducibility.

Table 2.1: Thermal conductivity of water and pentane in liquid and vapor phase

$(\mathrm{Wm^{-1}K^{-1}})$	κ_l	κ_v
Water	0.65	0.03
Pentane	0.11	0.019

Based on the above results, we can briefly discuss the stability of vapor nanobubbles. Below the critical boiling temperature, there is no vapor bubble formation. The temperature decreases as the inverse distance r in the liquid. As the absorbed power increases, the surrounding liquid becomes hotter and hotter, and approaches the threshold temperature (the dashed curve in Fig.2.4) for vapor bubble formation. Once the absorbed power is high enough, the surrounding liquid could cross the liquid-vapor saturation curve and a vapor bubble can form around the particle. Under steady state, we can see from Fig.2.4 that the liquid temperature outside the vapor bubble is always below the equilibrium temperature $T_{eq.}(r)$. That means that the liquid temperature decreases steeply enough with radius to remove the heat from the vapor bubble, so that

the hot water layers outside the bubble remain stable, as shown by the crossing curves in Fig.2.4. On the other hand, when a very thin vapor shell forms quickly before the steady state is established, it can push the hot liquid outside the vapor. Then the equilibrium temperature will drop below the temperature of the liquid surrounding the vapor. As a consequence, the liquid will become superheated, and explosive boiling can set in. In this situation, the excess heat in the liquid cannot be removed sufficiently quickly and will raise the temperature of the vapor bubble. Thus the vapor bubble becomes unstable and grows to a bigger size. These effects will be seen in Chapter 3 since we could not pass continuously from liquid phase to stable vapor bubbles in the measurements. The vapor nanobubble's formation seems to be explosive even though the heating remains constant.

2.4. Linear variation analysis of bubble radius as a function of heating power

Because we are increasing the laser power only by a small amount above the critical power for the formation of a nanobubble, it may be useful to linearize the relationship between the steady state bubble radius and the absorbed power.

By making a small variation in the power P_{abs}, we change the bubble radius by an amount δr_b. For small enough variations Eq.2.3 leads to:

$$\begin{cases} \dfrac{d\gamma}{dT}\dfrac{2\delta T_b}{r_b} - \dfrac{2\gamma(T_b)}{{r_b}^2}\delta r_b = \dfrac{dp_{vap}}{dT}\delta T_b \\ \delta T_b = \dfrac{\delta P_{abs}}{4\pi\kappa_l r_b} - \dfrac{P_{abs}}{4\pi\kappa_l {r_b}^2}\delta r_b \end{cases} \tag{2.5}$$

Then we get the bubble radius change δr_b:

$$\frac{\delta r_b}{r_b} = \frac{\delta P_{abs}}{P_{abs}}\left[\frac{8\pi\gamma(T_b)}{P_{abs}}\left(\frac{2}{r_b}\frac{d\gamma}{dT} - \frac{dp_{vap}}{dT}\right)^{-1} + 1\right]^{-1} \tag{2.6}$$

The required values at threshold for a gold nanoparticle in water are given in Table 2.2. The slope at the threshold is 0.8 nm/μW for water. We note that the bracket in the denominator may in principle change sign, which would make it impossible to have a stable bubble. However, we checked that this cannot happen in the parameter region corresponding to our experiments.

Table 2.2: Numbers required for a linear variation analysis for the formation of a vapor bubble around a particle in water (first line) and pentane (second line). T_b is boiling temperature at the surface of a 40 nm radius particle.

liquid	r_p (nm)	r_b (nm)	P_{abs} (μW)	T_b (K)	$\gamma(T_b)$ ($\mathrm{N\,m^{-1}}$)	$d\gamma/dT$ ($\mathrm{N\,m^{-1}\,K^{-1}}$)	p_{vap} (MPa)	dp_{vap}/dT ($\mathrm{MPa\,K^{-1}}$)
H_2O	40	40	62.13	483.2	3.571×10^{-2}	-2.28×10^{-4}	1.889	3.768×10^{-2}
C_5H_{12}	40	40	4.0	366.9	8.269×10^{-3}	-9.9×10^{-5}	0.514	1.198×10^{-2}

2.5. Photothermal signals with and without nanobubbles

In principle, the photothermal signal is proportional to the integrated change of refractive index surrounding the absorber over the volume of heat diffusion.

$$S \sim \int \Delta n dV \tag{2.7}$$

We now consider the photothermal signal in two cases.

I. Gold nanoparticle surrounded by liquid:
Under steady state, we have

$$\Delta n = \frac{dn}{dT}\Delta T = \frac{dn}{dT}\cdot\frac{P_{abs}}{4\pi\kappa}\frac{1}{r} \tag{2.8}$$

P_{abs} is the power absorbed by the absorber; n, κ are the refractive index and thermal conductivity of the surrounding medium; dn/dT is determined by the properties of the medium; r is the radius as measured from the center of the absorber. Substituting Eq.2.8 into Eq.2.7, we get the photothermal signal of a gold nanoparticle in liquid as follows:

$$S_1 \sim \int \Delta n \cdot exp\left(-\frac{r^2}{a^2}\right) dV = \frac{P_{abs}}{4\pi\kappa}\frac{dn}{dT}\cdot 2\pi a^2 \tag{2.9}$$

where $a^2 = \int e^{-\frac{r^2}{a^2}} dr^2 = 2\kappa/\omega C_p$, a is the heat diffusion length related to the heating modulation frequency; κ is the thermal conductivity of liquid; ω is the modulation frequency and C_p is the heat capacity per unit volume. The slope of the signal with respect to the absorbed power is:

$$\frac{d|S_1|}{dP_{abs}} = \frac{1}{4\pi\kappa_L}\left|\frac{dn}{dT}\right| 2\pi a^2 \tag{2.10}$$

II. Gold nanoparticle surrounded by a thin vapor shell in liquid:
In this case, heat diffuses through both the thin vapor shell and the outside liquid . So the integration in Eq.2.7 should have two photothermal contributions

corresponding to the steam and the liquid:

$$S_2 = S_V + S_L \tag{2.11}$$

for a thin vapor shell, S_V is approximately $(n_v - n_L) \cdot 4\pi R^2 d$, where n_v and n_L are the refractive index of vapor steam and liquid ($n_v \approx 1, n_L = 1.3$), R is the particle radius and d is the thickness of the vapor shell. The derivative of S_V over absorbed power can be calculated from the analysis in Section 2.4:

$$\frac{d|S_V|}{dP_{abs}} = (n_L - n_V) \cdot 4\pi R^2 \frac{dh}{dP_{abs}} = (n_L - n_V) \cdot 4\pi R^2 \frac{\delta r_b}{\delta P_{abs}} \tag{2.12}$$

Then the slope ratio between vapor shell and liquid is:

$$\frac{d|S_V|}{dP_{abs}} \Big/ \frac{d|S_1|}{dP_{abs}} = 8\pi\kappa_L \frac{\delta r_b}{\delta P_{abs}} \frac{R^2}{a^2} (n_L - n_V) \cdot \left|\frac{dn}{dT}\right|^{-1} \tag{2.13}$$

Consider $n_L - n_V = 0.3$, $\left|\frac{dn}{dT}\right| \approx 10^{-4}\mathrm{K}^{-1}$, $R = 40$ nm, $a \approx 100$ nm, $\frac{\delta r_b}{\delta P_{abs}} \approx 1$ nm/μW at the threshold, the slope ratio is about 8. In chapter 3, we will see that this number is close to the data measured with photothermal microscopy.

2.6. Conclusions

In this chapter, we provide a simple thermodynamic model of vapor nanobubbles assuming steady state. Based on the standard physical data from NIST, we calculated the minimum/critical boiling temperature and pressure of a vapor nanobubble around a CW laser-heated gold nanoparticle. We also consider the temperature distribution with and without vapor nanobubbles under various absorbed powers, and the optical signal change due to the presence of vapor bubbles. Even though this model is very simple, it provides insight into the thermodynamic properties of vapor bubbles as well as into the experimental conditions for vapor nanobubble studies.

3

Explosive formation and dynamics of vapor nanobubbles around a continuously heated gold nanosphere

Abstract– *We form sub-micrometer-sized vapor bubbles around a single laser-heated gold nanoparticle in a liquid and monitor those through optical scattering of a probe laser. Bubble formation is explosive even under continuous-wave heating. The fast, inertia-governed expansion is followed by a somewhat slower contraction and disappearance after some tens of nanoseconds. In a narrow range of illumination powers, bubble time traces show a clear echo signature. We attribute it to sound waves released upon the initial explosion and reflected by flat interfaces, hundreds of microns away from the particle. Echoes can trigger new explosions. A nanobubble's steady state (with a vapor shell surrounding the heated nanoparticle) can be reached by a proper time profile of the heating intensity. Stable nanobubbles could have original applications for light modulation and for enhanced optical-acoustic coupling in photoacoustic microscopy.*

The contents of this chapter are based on:
L. Hou, M. Yorulmaz, N.R. Verhart and M. Orrit. *"Explosive formation and dynamics of vapor nanobubbles around a continuously heated gold nanosphere"*. New J. Phys. **17**, 013050 (2015).

3.1. Introduction

Gas bubbles in liquids are involved in many processes and applications [4]. Cavitation bubbles cause mechanical damage [3], and even can produce high-energy electromagnetic radiation, an effect called sonoluminescence [5]. The dynamics of bubbles driven by acoustic waves is highly nonlinear and displays many complex phenomena including chaos [4]. In the present chapter, we consider nanobubbles, i.e., bubbles with diameters of a few tens to hundreds of nanometers. Compared to earlier experiments on microbubbles (a few microns to tens of microns in diameter), nanobubbles are more difficult to observe, study and manipulate. However, they may give rise to simpler or different properties, for example because liquid flows around nanobubbles present lower Reynolds numbers [16].

The standard method to form a gas bubble optically is to illuminate an absorbing liquid with a (sub-)picosecond laser pulse [69, 70]. Alternatively, the energy absorbed by a metal nanoparticle is transferred to the liquid by conduction. Because of the fast excitation and of the high heat conductivity of the metal, the particle's temperature is raised within a few picoseconds to well above the boiling temperature of the liquid, whose sudden vaporization leads to a necessarily explosive expansion of hot steam, pushing the liquid away and launching bubble dynamics in the nanosecond time regime. Transient nanobubbles produced by short laser pulses have been monitored [25, 31, 71] i) by optical imaging with short pulses, giving direct access to bubble size, ii) through the time dependence of probe light scattered off the bubble, giving time-resolved information, iii) by acoustic detection of emitted sound waves [25], or by the combination of electric conductivity through a nanopore and optical detection [28]. The environment change upon boiling can be detected via the particle's plasmon resonance [39], or by photothermal detection [72] but with limited time resolution. Ensembles of nanobubbles were studied by light scattering and by small-angle X-ray scattering of short X-ray pulses [32], or by pump-probe spectroscopy [73, 74], but these methods do not apply to single nanobubbles. Baffou *et al.* [75] used an imaging microscope to create microbubbles with continuous illumination of a single gold nanoparticle, also with low time resolution. Cichos' group modulated a probe beam by an isotropic bubble in a nematic liquid crystal close to its phase transition [76], but this process is much slower than the liquid-vapor equilibria considered here.

Stable nanobubbles are interesting for their fundamental properties [77, 78] and may have useful applications [79]. A nanobubble is an efficient two-way transducer between acoustic and optical waves because of its large compressibility and optical scattering cross-section. A stable nanobubble could be an

attractive beacon, source, or detector in photoacoustic microscopy [80].

Thus, we set out to heat a gold nanoparticle with a continuous laser beam, striving towards a precise balance between heat production in the nanoparticle and heat loss to the surrounding liquid. We monitor bubble formation and dynamics optically, which provides high time resolution down to the nanosecond, single-shot regime. Future experiments with short probe pulses and stroboscopic detection may give access to the sub-picosecond regime. To our surprise, we could not pass continuously from regime I where the particle is surrounded by hot liquid to regime II where a stable vapor shell is present around the particle, by increasing the heating power (see Chapter 2 for details). Instead, the system undergoes an explosive transition. After characterizing this instability, we show that a proper time profile of the heating intensity allows us to create a persistent nanobubble that lasts up to a microsecond.

3.2. Methods and experimental details

One of our main concerns is the reproducibility of our experiments. We wanted to study the same nanoparticle for a long time under different experimental conditions for direct comparison. We therefore worked with gold nanospheres immobilized on a glass substrate, which can be imaged with high precision in a standard confocal microscope. To obtain large enough optical signals, the size of nanoparticles was chosen to be 80 nm in diameter. We also expect surface effects and irreversible shape changes of the particle or of the particle-substrate area to be (relatively) less important for large particles. The gold colloidal suspension is bought from a commercial company (British Biocell International). The diameter of the particle is about 78 nm on average with 4.5 nm standard deviation (see Fig.3.1.b).

For the sample preparation, we used gold nanospheres and immobilized these on a glass coverslip by spin coating. The particles and the glass substrates were cleaned from organic ligands by repeated flushing and ozone cleaning. We checked that all particles used in the present work were isolated single ones, by photothermal contrast [81]. The particles were covered with the liquid (water or n-pentane), so that bubbles could form in the half-space limited by the flat glass-liquid interface. This breaks the spherical symmetry of the nanobubble with respect to the gold nanoparticle and the interface (see the scheme in Fig.3.1.a), but the nanobubble itself could have a spherical shape. Our first experiments were done in water for convenience and because it is by far the most interesting fluid for applications. However, boiling water around a nanoparticle requires temperatures up to 550 K, and the temperature of the gold particle can easily reach several hundreds of Kelvin above the water's temperature (see

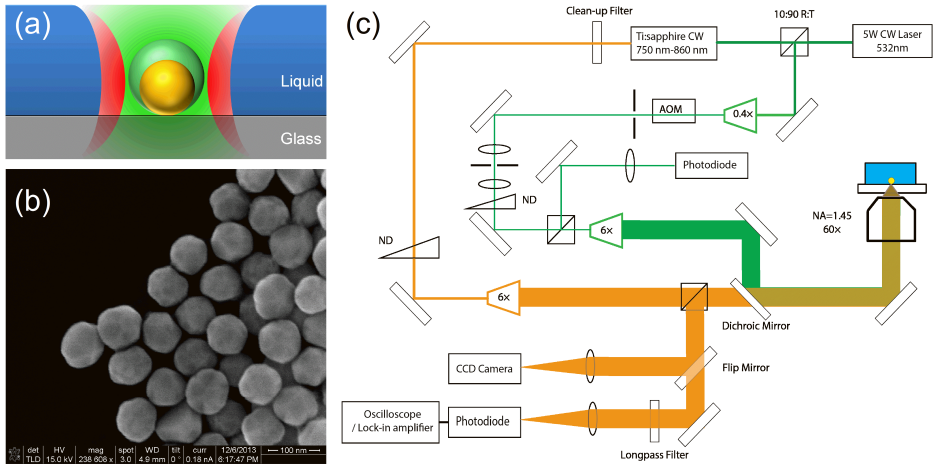

Figure 3.1: (a) Scheme of the vapor bubble formation; (b) SEM image of 80 nm gold spheres. Scale bar is 100 nm; (c) Experimental setup. AOM: acousto-optic modulator; ND: variable neutral-density filter.

Fig.2.4 in Chapter 2). Such high temperatures can lead to irreversible changes in particle shape (movement of facets and of surface atoms) and, more critically, to changes in the contact area between gold and glass. Therefore, to limit the possibility of such random or irreversible changes we used n-pentane in most experiments. Pentane has a low boiling point (309 K at atmospheric pressure), so that the estimated particle's temperature did not exceed 370 K upon boiling under our experimental conditions. This temperature remains low enough so that we can safely neglect surface rearrangements even after long illumination times.

The optical setup, shown in Fig.3.1 (c), is a typical photothermal microscope [42]. The advantages of an all-optical investigation of the nanobubble are its speed, non-invasiveness and sensitivity. Photothermal microscopy is a technique based on the absorption of small objects such as gold nanoparticles. A modulated heating beam heats the nanoparticle and creates a temperature gradient, or thermal lens, around the absorbing object. A non-resonant probe beam, which is spatially overlapped with the heating beam, is scattered by the thermal lens and interferes with a reference beam, usually the transmitted or reflected probe beam. The interfering probe beam is then collected by a photodetector such as a photodiode, and the signal is demodulated by a lock-in amplifier. We used the photothermal signal to overlap the heating (532 nm) and probe (815 nm) beams, to identify single gold nanoparticles in the sample, and also to find the critical intensity required for boiling. However, the photother-

mal signal, being produced by a lock-in amplifier with an integration time of at least 0.1 ms, was too slow to follow fast bubble kinetics in the nanosecond and microsecond domains. For those time-resolved measurements, the probe signal collected in reflection mode in bright-field scattering [82] was directly fed into the fast photodiode and the electronic signal was recorded in a fast oscilloscope with large memory.

3.3. Photothermal detection

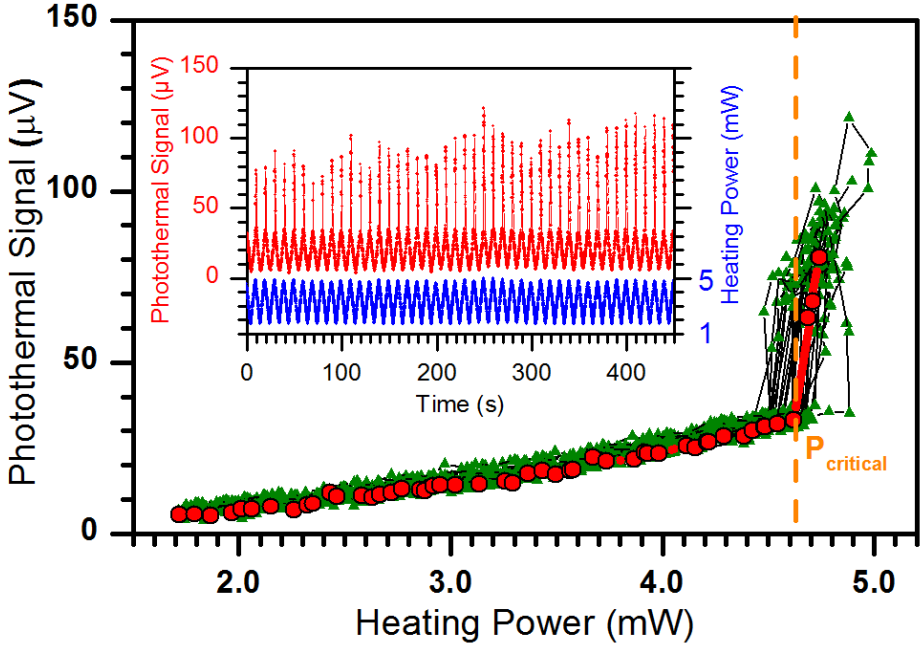

Figure 3.2: Photothermal signal of a single gold nanosphere in water as the heating intensity is increased. Until a critical power of 4.6 mW (about 0.6 MW/cm^2) the signal increases smoothly as expected for heated liquid water. Above the critical power, the signal undergoes a sudden jump to a much higher value, with large fluctuations. Red dots: a typical example of a power sweep; green triangles: accumulated data from many sweeps showing the dispersion in signal and in critical power. The data of each sweep are connected by a solid line. Insert: photothermal signal (red line, left scale) as a function of time while the heating power (blue line, right scale) is swept as a saw-tooth function between values below and above the critical power.

We started our study of single immobilized nanospheres in water with photothermal contrast. At low heating power, we find continuous heating of the liquid around the particle [83]. Above a critical pump intensity, the photothermal signal increases suddenly as shown in Fig 3.2, due to water boiling and

nanobubble formation. Repeated heating cycles around the threshold power show fluctuations of the transition power by a few percent. The particle temperature, estimated from the absorption cross section and the heat conductivity of water and glass (see Chapter 2 and Appendix C for details), corresponds well with the simple model in Chapter 2. However, this steady-state model fails to explain the strong variability of the signal and the irreproducibility of successive transitions. Even at its highest time resolution (0.1 ms) of lock-in detector, the detection is too slow to follow the dynamics of the nanobubble.

The model of Fig.2.4 in Chapter 2 shows that the particle temperature can rise by hundreds of K once the bubble forms. Such high temperatures might degrade the particle's shape and its contact area with the substrate. Therefore, we adjusted the intensity carefully to avoid damaging the particle. Moreover, we switched to a different liquid, n-pentane, which has a much lower boiling point than water, to further limit irreversible damage to the system and ensure reproducibility of the results. The physics of bubble formation and dynamics in pentane will thus serve as a model for bubble formation in water.

3.4. Direct probe detection

We directly detect the scattered probe intensity with the fast photodiode, following the bubble signal in real time. Figure 3.3 (a) shows an example of a time trace recorded at 100 μW, just above the critical power (94 μW) in liquid pentane. The complex boiling trace of Fig 3.3 (a) appears as a succession of brief and violent events lasting some tens of nanoseconds only, separated by 500 ns on average. Such violent events are characteristic of explosive boiling, which is often observed in superheated liquids [64], and which can be suppressed with superhydrophobic coatings [84]. Herein, we use the word "explosion" to describe a rapid bubble expansion on the nanosecond time scale, similar to what is customary in pulsed heating experiments [4, 13, 16, 28, 70]. Note that these explosions occur at low Reynolds numbers (defined as $Re = \rho v R_b/\mu$, where ρ and μ are the liquid density and viscosity; v and R_b are the characteristic velocity and the size of such explosions), of the order of unity. The contraction or the decay part of the nanobubble signal resembles the collapse behavior of acoustically driven gas bubbles [4]. The signal-to-noise ratio is good enough to follow individual explosions (Fig 3.3.b), which present a rise time of about 14 ± 2 ns and a decay time of about 31 ± 7 ns, longer than the detector's rise and fall times 5 and 16 ns respectably. We averaged hundreds of such events, synchronizing them with the rising edge of the signal, and obtained the averaged profile of Fig 3.3 (c), which appears only slightly broadened by the averaging to a rise time of 18 ns. The decay part of the explosion signal presents a small but reproducible

shoulder which will be discussed below. Beyond the main initial peak, the averaged trace shows further undulations at longer times, with average spacing of 500 ns, corresponding to the later explosions. They broaden with time because of the lack of exact periodicity.

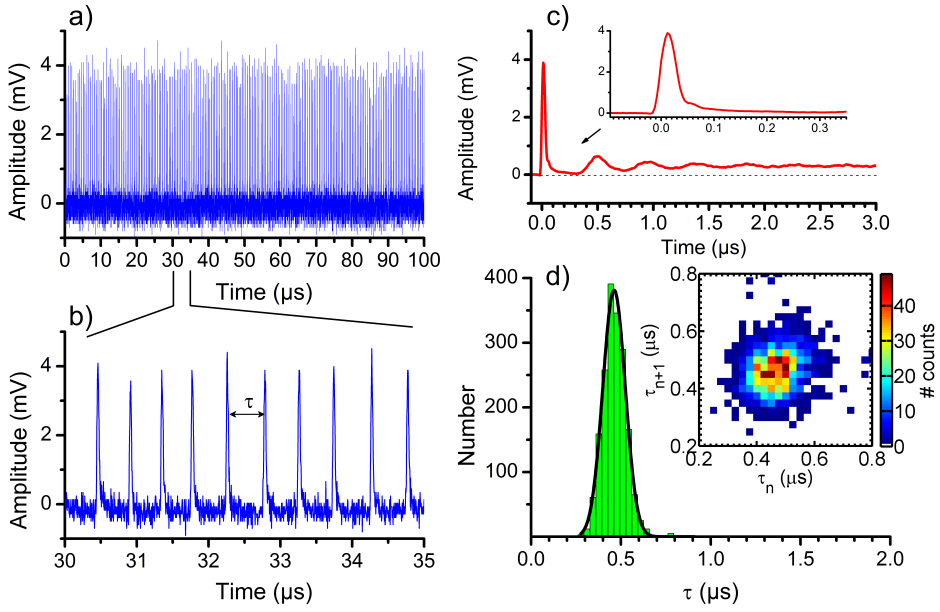

Figure 3.3: Direct probe detection of nanobubbles under constant heating (100 μW) just above the threshold for boiling. Detector gain: ×1000, bandwidth: 10 MHz. (a) Typical time trace of the scattered probe beam showing successive explosive nanobubble events. The probe power is fixed at 5 mW; (b) Further zoom-in on one part of time trace (a); (c) Average of 3,123 explosions in time trace (a), taking the half maximum of the rising edge of the signal as the time reference. Insert: zoom-in on the main peak; (d) the histogram of delay times between two successive explosions. The solid line is a Gaussian fit. Insert: scatter plot of all pairs of consecutive delays, τ_n and τ_{n+1} , from the trace in (a).

Taking a long trace with hundreds of bubble explosions, we can look at the distribution of inter-explosion delays, shown in Fig.3.3 (d). No explosion is found to occur at less than 300 ns from the previous one. The distribution is well fitted by a Gaussian, with a maximum at about 500 ns for the conditions of Fig.3.3 (d). We also present a scatter plot of the pairs of times between successive events (τ_n, τ_{n+1}) in a 2D diagram (Fig.3.3.d, insert). This plot appears compatible with a purely random succession of inter explosion times drawn at random from the Gaussian distribution of Fig.3.3 (d). We thus conclude that the random noise causing jitter, or deviations from the average inter-explosion

times, are uncorrelated between successive events. Similar jitter observations were reported in ref. [28], and attributed to randomness in the bubble nucleation process. In particular, the jitter in nanobubble dynamics is not caused by experimental imperfections such as laser intensity noise or focus drift. Note that heating intensity drifts can affect our measurements, as shown in the Appendix E.

We now propose and discuss a mechanism for this unexpected explosive boiling under continuous-wave heating conditions. As we saw in the introduction and Chapter 2, to nucleate and grow, the nanobubble needs to overcome the Laplace pressure in addition to the ambient pressure. This only happens at 367 K for an 80-nm particle in pentane (483 K in water). Once the bubble starts to grow, however, the effective boiling temperature decreases because the Laplace pressure itself decreases. When a small part of the hot liquid vaporizes, it generates a first very thin vapor shell, which pushes the remaining hot liquid just outside the bubble. This hot liquid now becomes overheated with respect to the vapor in the bubble, because of the lowered Laplace pressure. It will then feed fresh steam into the bubble, further amplifying the expansion. We have estimated the energies involved in bubble growth (see details in the Appendix D). We find three main contributions. Two of them are energy costs: i) the surface energy, which increases with bubble radius because both surface and surface tension increase, ii) the latent vaporization heat and internal vapor energy needed to expand the bubble. The third contribution is a source of energy, iii) the thermal energy stored in the overheated liquid layer. This heat can flow either to the cooler water layers at larger radii, or towards the bubble, helping its growth. For a final bubble radius of 140 nm, these contributions are - 1 fJ, -2.8 fJ, and 8.3 fJ, respectively, which indicates that bubble expansion liberates energy and is therefore thermodynamically favorable. Note that conduction through the liquid is fast enough to make this energy kinetically available during the expansion, as the diffusivity of heat in liquid pentane ($6\times10^{-8}\mathrm{m}^2/\mathrm{s}$) corresponds to 8 nm in 1 ns. Once the excess thermal energy has been consumed into surface energy and latent heat, the bubble eventually reaches a maximum radius and shrinks back under the restoring forces of surface tension and vapor condensation. Indeed, at the maximum bubble radius, cooling of the thinned hot liquid layer by the outer cold liquid is very efficient. This explains that the bubble may disappear completely upon shrinking, as the returning cold bubble wall can condensate all the vapor. The cold liquid will have to be heated again by the nanoparticle during some hundreds of nanoseconds in our conditions before a new overheated layer is established and a new explosion can take place.

We note that a similar mechanism is at work in short-pulse experiments,

where heat supplied by the hot nanoparticle first has to be conducted to the surrounding liquid before boiling can set in [32]. We can also compare our system to air bubbles in water. Those can reach very small minimal radii, with accordingly high temperatures and luminescence [85], followed by multiple afterbounces. In our case, however, the steam condensates until the bubble's surface hits the nanoparticle and the bubble disappears. Indeed, the data of Fig.3.3 (b) and Fig.3.3 (c) show that this contraction step is not followed by any clear afterbounces, apart from the small shoulder seen in Fig.3.3 (c) at 60 ns, which will be discussed hereafter. The explosion repetition rate is mainly determined by the rate at which the overheated liquid layer is heated, but it may also depend on the microscopic crossing of the nucleation barrier, as proposed recently by Nagashima et al. [28] in the bubbles produced by Joule dissipation in a nanopore. Our analysis of time traces of Fig.3.3 did not reveal any sign of a chaotic dynamics [86].

3.5. Estimation of bubble size

As the bubble is presumably smaller than the diffraction limit of the microscope, direct imaging cannot be applied. We estimated the bubble size in three independent manners:

i) From the time dependence of explosions: From published experiments [4, 25, 70] and theory [16], the bubble expansion and contraction times vary approximately linearly with bubble radius. The associated velocities are found in the range 10-15 m/s for water. The Rayleigh theory gives a similar number and ref. [25] finds that surface tension introduces a factor of about 2 with respect to Rayleigh theory. From these values and a time of about 15 ns, we estimate the bubble radius in our experiments to 150 nm.

ii) From the decreased scattered probe intensity with offset of the beam from the particle: By shifting the probe focus off the maximum overlap with the particle, we find that the signal decreases to half its value for a distance of 160 nm, which would correspond roughly to the radius of the bubble (distance of the edge to the center).

iii) From the absolute scattered probe intensity compared to reflected intensity: We compared the scattered probe intensity to the probe intensity reflected by the interface. The change upon bubble explosion is about 20%. By identifying this ratio to an area ratio between the bubble's cross section and the diffraction-limited cross section of the probe beam, we obtain a radius of about 200 nm.

Therefore, the three independent estimates above converge to a bubble radius of 100-200 nm, below the microscope's resolution.

3.6. Echo-triggered explosions

Under finely tuned experimental conditions, a large fraction of explosion events are followed by after-pulses. Figure 3.4 shows an example of what is observed with the particle studied in the experiments of Fig.3.3 but with a slightly lower heating power (97 μW), corresponding to an inter-explosion delay of about 1 μs. In contrast to Fig.3.3, the after-pulse of Fig.3.4 occurs at a well-defined delay of about 200 ns after the main explosion, which distinguishes it from the next explosion requiring a fully restored overheated layer. We propose that after-pulses are weaker explosions triggered by sound echoes of the main explosion, reflected from flat interfaces around the nanoparticle (see the scheme in Fig.3.4.c).

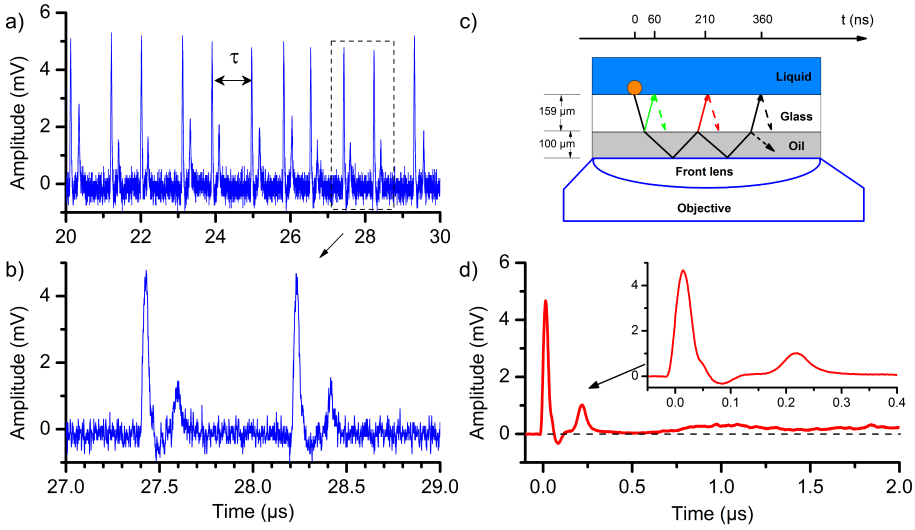

Figure 3.4: Echo-triggered nanobubble explosions under finely-tuned constant heating power above the threshold. (a) The non-averaged time trace of scattered probe presenting echo-triggered bubbles. The probe power is fixed at 5 mW; (b) zoom-in time trace on the dash-block part in (a); (c) space-time scheme showing the sound propagation and reflections in different media around the particle; (d) averaging signal of 1,108 explosions in (a) in the same way as Fig.3.3 (c). Insert: zoom-in on the main peak.

Two interfaces are possible candidates: i) the other side of the glass coverslip. With a thickness of 159 μm and a sound velocity of 5640 m/s [87], the echo arrives 56 ns after the explosion. This is precisely the delay of the shoulder seen in the decay of the bubble signal, both in Fig.3.3 (c) and Fig.3.4 (d); ii) the interface between the immersion oil and the objective lens. The distance between the lens and the oil-glass interface is 100 μm (working distance ac-

cording to the manufacturer). With a sound velocity of 1350 m/s in oil [88], this echo from the second interface should arrive about 204 ns after the main explosion, exactly as observed in Fig.3.4 (d). The after-pulse would thus be a second, weaker explosion triggered by the echo. It may feed on thermal energy left in the hot water layer after the first explosion or conducted from the hot particle. This remarkable phenomenon highlights the extreme sensitivity of a bubble to weak perturbations. Although the initial sound wave is attenuated by two transmissions through the glass-oil interface, reflection on an oil-glass interface and propagation as a spherical wave through 159 μm of glass and 100 μm of oil, this weak echo wave suffices to trigger a measurable signal 56 ns after the first explosion and even a second explosion 204 ns later. In a few cases (see Appendix F), a second after-pulse follows the first one and can be attributed to an additional reflection.

3.7. Towards the stabilization of a nanobubble

The nanobubble around the particle can be stabilized by means of a suitable time profile of the laser intensity. The instable layer of overheated liquid around the nanoparticle makes it impossible to pass smoothly from regime I to regime II mentioned in the introduction. However, the inverse process, in which the heating power is continuously decreased from a point in regime II does not generate any unstable situation. Indeed, the continuous presence of the liquid/vapor interface ensures that the two phases remain in equilibrium at all times, so that the bubble disappears in a continuous way when the heating power is reduced.

We designed the following time profile of the heating laser power to lengthen the nanobubble's persistence. We start just below the critical boiling power (0.96 P_c), then suddenly raise the heating intensity to a high value (1.1 P_c; in practice, due to the finite response time of our acousto-optic modulator, the rise in heating lasts about 100 ns). We then keep the intensity at this high level for a variable duration, 1 μs in the case of Fig.3.5, before reducing it back to the initial level. The result of this cycle for the scattered light is shown in Fig.3.5 together with the heating intensity profile. The measurements were done in liquid pentane.

Averaged probe signal traces following a raise in heating power are presented in Fig.3.5 (see single-shot traces in Appendix G). Again, the individual single-shot traces were averaged by synchronizing them on the mid-rising edge of the probe signal. The averaged trace clearly shows an initial explosion of about 30 ns duration and of lower amplitude than those in Figs.3.3 and 3.4, followed by a plateau at a high scattering value. The probe signal after the ex-

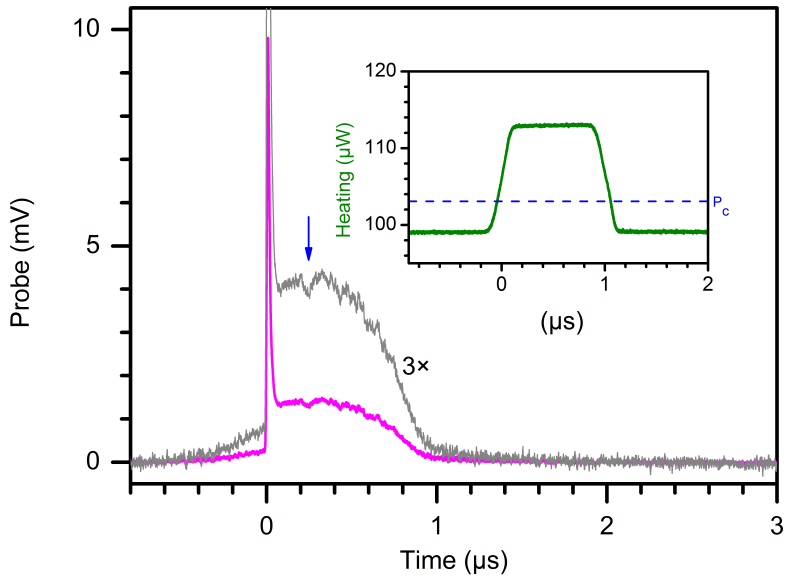

Figure 3.5: Formation of a persistent nanobubble. The pink line shows the probe signal averaged over 200 explosive events following triggering by a raise in heating power. Detector gain: ×10,000, bandwidth: 200 MHz. The events have been averaged by synchronizing at mid-rising edge of the probe transient signal. Insert: The averaged heating profile (green), synchronized at mid-rising edge of the periodic heating pulse as delivered by the acousto-optic modulator. The dashed line is the critical heating power. After explosive formation, the nanobubble persists for up to 800 ns. The heating beam is modulated by a block pulse profile with a frequency of 100 kHz and a duty cycle of 10% (1 μs on-time in a 10 μs period).

plosion is much higher than before, when it was due to the liquid's temperature change alone. This high value indicates the presence of the bubble, and its persistence for as long as the heating power is kept at the high level. The bubble disappears as soon as the heating power is reduced. We therefore conclude that, in the few hundred ns following the explosion, the bubble reaches the steady-state extent discussed and calculated in chapter 2. After the shrinking phase of the initial explosion, the bubble remains as a stable shell because enough heating power is provided, and the energy received by the vapor shell from the particle balances the energy lost by conduction to the cooler liquid outside. This experiment shows the feasibility of reaching and maintaining steady state II, once the barrier of bubble formation is passed. Much longer times than 1 μs could be achieved by optimizing the time profile and intensity stability of the heating power or by a proper, fast enough feedback mechanism from the scat-

tered signal. A reproducible feature (shown with a blue arrow) appears on the trace of Fig.3.5, about 200 ns after the initial explosion. We assign this feature to the reaction of the nanobubble to the sound echo reflected by the oil-lens interface discussed in the previous section.

In some measurements with the same protocol in water, we observed self-oscillations of the nanobubble. Figure 3.6 shows a single-shot observation of a nanobubble formed in water upon a 1 μs raise of heating power. The particle size is still 80 nm in diameter. This bubble appears without an initial explosion and starts to oscillate after a few hundreds of ns. The oscillations damp out when the power is decreased again below the critical value. The oscillation period is roughly consistent with the time given by the Minnaert oscillation period of a bubble [17]. The possible mechanism of this self-oscillation is still unclear and requires additional investigation in the future.

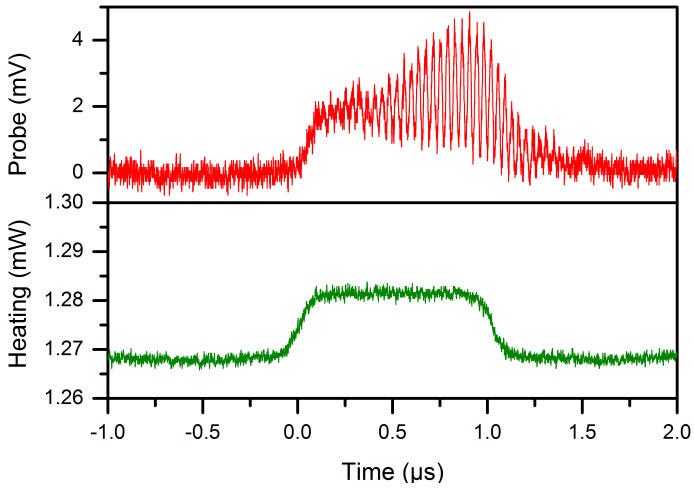

Figure 3.6: A single-shot time trace showing the self-oscillating behavior of a nanobubble. Above: probe signal; Below: heating profile. In this measurement, the gold particle is in pure water and on BK7 glass substrate. The duration of the heating 'pulse' is 1 μs. The oscillation period of the bubble is about 30 ns, corresponding to 33 MHz.

3.8. Conclusions and outlook

Boiling of a liquid around a heated metal nanoparticle can be controlled and detected with high sensitivity and fast time response. Even under continuous-wave heating, nanobubble formation is explosive. No after-bounce could be detected upon bubble shrinking, presumably because all kinetic energy is dis-

sipated upon vapor condensation. The fast time response (less than 15 ns for the expansion and 20-30 ns for the contraction) could be used for all-optical light modulation with a bandwidth of about 100 MHz, several orders of magnitude faster than with liquid crystals [76]. Within a narrow range of heating power, the nanobubble becomes extremely sensitive to weak perturbations such as sound waves reflected from far-away interfaces. Acoustic wave fronts released in an initial explosion could trigger a new explosion, or even lead to self-oscillations. We have shown that a steam nanobubble can be stabilized with a suitable heating intensity profile, and by controlling the heating laser power during the shrinking phase.

In this work, we did not provide a proper theoretical modeling. Compared to the inertial Rayleigh-Plesset theory and its refined versions including surface tension [19] and heat and mass transfer [5], the present system requires consideration of the thermodynamic and kinetic features of the liquid-gas phase transition [16] at nanometer scales. Moreover, the geometry of our experiment excludes spherical symmetry and calls for a full 3D model. Such a complex theory is well beyond the scope of the present work. Our results suggest using bubbles as nanoscale generators and detectors of acoustic waves, much as radars are used at macroscopic scales for electromagnetic waves.

3.9. Acknowledgments

This work is supported by the Foundation for Fundamental Research on Matter (FOM) with funding from NWO. L.H. acknowledges the financial support of China Scholarship Council. Advice from Dr. P. Zijlstra and programming assistance of A. Carattino are kindly acknowledged.

4

Time-resolved study of vapor nanobubbles in water around a continuously laser-heated gold nanoparticle

Abstract– *We apply picosecond pump-probe spectroscopy to investigate the formation of vapor nanobubbles around a continuously heated gold nanoparticle in water. The aim of this experiment is to simulate the explosions observed under continuous heating, but by triggering the explosions by a short pump pulse. We obtain time traces of vapor bubbles with picosecond time resolution, apparently synchronized with the pump pulse. We observe a characteristic interference feature in the time trace and a strong modification of the signature of acoustic vibrations of the gold nanoparticle.*

4.1. Introduction

Studies of vapor nanobubbles have attracted more attention in recent years not only because their transient nature and thermodynamics have not been fully understood [22], but also because nanobubbles could be useful in applications such as photothermal therapy [6, 9, 89], drug delivery [7], solar steam generation [35], as contrast agents to enhance photo-acoustic couplings [10] and for chemical reactions [11, 90]. One way of generating vapor nanobubbles is to heat a liquid locally using a laser beam in the presence of nanoabsorbers such as gold nanoparticles to enhance the absorption efficiency [91]. Due to the fast excitation and relaxation of electrons and phonons and to the high thermal conductivity of the metal, a homogeneous temperature distribution is established in the gold nanoparticle after a few picoseconds. Subsequent heat transfer into the surrounding liquid in a few hundred picoseconds can initiate boiling of the liquid in the vicinity of the gold nanoparticle. The dynamics of the ensuing vapor bubble has not been characterized at the single bubble level on the sub-nanosecond timescale. Liquid superheating has been observed in many rapid heating processes [26, 28, 66] and is often accompanied by explosive boiling. Experiments with pulsed or continuous lasers have been extensively carried out to uncover the physical and thermal properties of vapor nanobubbles [8, 36, 92]. For example, vapor nanobubbles around gold nanoparticles have been studied using photothermal microscopy [30], bright-field optical scattering [73, 93], and dark-field spectroscopy [39] with time resolutions down to nanoseconds. Time-resolved pump-probe spectroscopy with picosecond lasers has been applied to study the spectral changes due to vapor bubbles around gold particles as a function of time delay [74], but the measurements were done in solution with several particles in the excitation volume. Pump-probe experiments with pulsed X-rays as the probe beam were performed to resolve the dynamics of vapor bubbles [26, 32, 94], providing the high sensitivity of X-ray scattering and diffraction to the structural changes of gold nanoparticles and of the surrounding water molecules, but the time resolution was limited to 100 ps because of the width of the electron beam, and the measurements are still done at the ensemble level, with several particles in the excitation focus.

Due to the fast dynamics and transient nature of vapor nanobubbles, it is quite challenging to investigate these at the single-nanoparticle level without averaging the contributions from nearby particles. The transient behavior of vapor nanobubbles also requires a high time resolution of detection in the sub-nanosecond timescale. Only then can the evolution of vapor nanobubbles during the initial stages after excitation be better resolved. In this chapter,

we combine continuous-wave (CW) heating with time-resolved pump-probe spectroscopy to study the transient behavior of vapor nanobubbles in water around a single gold nanosphere. The CW heating beam brings the temperature of the gold nanoparticle close to the boiling threshold of water, and the pump pulse drives the system out of equilibrium and triggers the dynamics of the vapor nanobubble on the picosecond timescale. We record transient traces of vapor nanobubbles upon femtosecond excitation under high CW heating and show that we can obtain picosecond time resolution in a time window of one nanosecond.

4.2. Experimental details

Time-resolved pump-probe measurements of vapor nanobubbles were done on a home-built horizontal microscope. A scheme of the optical setup is shown in Fig.4.1. A femtosecond pulse (about 300 fs) with central wavelength 785 nm from a Ti: sapphire laser (76 MHz repetition rate) is used as the pump source. The probe pulse is the synchronized frequency-doubled output of an optical parametric oscillator (OPO, tunable wavelength from 590 nm to 640 nm) [95]. This OPO is pumped by the above Ti: sapphire laser. A continuous wave (CW) laser at 532 nm is spatially overlapped with the two pulsed beams. The three beams are sent into the microscope and focused on the sample with an oil-immersion objective (Olympus, NA=1.4). The intensity of the pump beam is modulated with an acousto-optical modulator at 450 kHz. The probe wavelength is chosen around 597 nm where the surface plasmon resonance (SPR) of single gold nanospheres is most sensitive to the changes of the refractive index of the surrounding medium. The transmitted light is collected by a second objective with a numerical aperture of 0.75, and is focused on a photodiode detector (FEMTO). A set of optical filters were placed in front of the detector in order to remove both the continuous and pump beams. Time delays between pump and probe pulses are controlled with a linear mechanical stage, which can move continuously and alter the propagation delay of the pump pulse. The signal of the photodiode is demodulated at the modulation frequency of the pump by a lock-in amplifier to extract the small change ΔT in the intensity of the transmitted probe beam. This ΔT was recorded as a function of time delay by a digital-analog converter (ADwin gold) and home-built Labview software. The alignment was optimized by maximizing the photothermal signal of a single gold nanosphere in water.

Gold nanospheres are purchased from BBI (British Biocell International). Their average diameter is about 50 nm. The cover slides are rinsed in acetone, ethanol and pure water separately and are cleaned in an ozone cleaner to re-

move all the possible impurities and organic contaminants. Gold nanoparticles are then spin-coated on clean cover slides. Concentration and spin-coating parameters are adjusted so that gold nanoparticles are well isolated from each other on the cover glass. Then the cover slide coated with gold nanoparticles is attached to a home-built flow cell made of Polydimethylsiloxane (PDMS). Milli-Q water was used in all the experiments. Positions of single gold nanoparticles are determined with the pump-probe microscope and time delay set to zero.

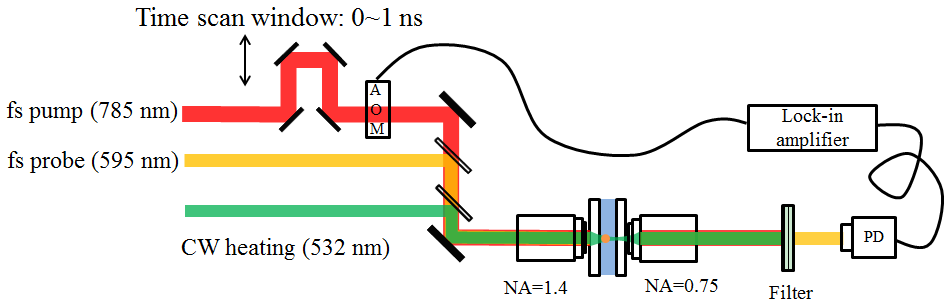

Figure 4.1: Scheme of the experimental setup for the time-resolved study of vapor nanobubbles. PD: photodiode; AOM: acousto-optic modulator.

4.3. Cooling kinetics and acoustic vibrations of a gold nanoparticle

Upon laser excitation, the following processes take place in successive steps. First, the SPR is excited by the pump pulse as a collective oscillation of the metal's conduction electrons. Subsequently, after some ten femtoseconds, the SPR relaxes through relaxation of the electrons, leading to a hot electron gas. Due to the small heat capacity of the Fermi gas, the electron temperature rises by thousands of Kelvins. Electron-electron scattering then redistributes the absorbed energy over the entire electron distribution, forming a hot electron gas on the timescale of hundreds of femtoseconds. On a longer timescale of a few picoseconds, the electrons transfer their excess energy to the gold lattice. Because of its relatively large thermal capacity, the gold lattice heats up to lower temperatures, typically some tens of Kelvin in one to a few picoseconds, as resolved by transient pump-probe spectroscopy [46]. On still longer times, which depend on the interfacial resistance and on the conductivity of the medium, the hot particle thermalizes with its environment. This time is typically a few hundred picoseconds in the case of our particles [48]. Eventually, the particle returns to the initial unperturbed state.

We adopt the modified "two-temperature model" (TTM) to describe the energy deposition into the electron system, its subsequent relaxation to the metal

lattice and the surrounding medium, and the temperature evolution in these subsystems is written as [96]:

$$\begin{cases} C_e(T_e)\dfrac{\partial T_e(t)}{\partial t} = -G(T_e - T_l) + S(t) \\ C_l(T_l)\dfrac{\partial T_l(t)}{\partial t} = G(T_e - T_l) - F \\ C_m\dfrac{\partial T_m(t)}{\partial t} = \nabla \cdot [\kappa_m \nabla T_m(r,t)] + F \end{cases} \tag{4.1}$$

where C_e, C_l, and C_m are the heat capacities of electrons, lattice, and surrounding medium (water in our case), respectively. T_e, T_l, T_m are the temperatures of electrons, lattice, and water medium; G is an electron-phonon coupling coefficient and is taken from ref.[97]; κ_m is the thermal conductivity of liquid water; $S(t)$ is the laser excitation function, and is adopted as the same function as ref.[98], assuming a 300 fs pulse width with a Gaussian intensity profile; F is the term that governs the heat exchange at the particle-liquid interface, and can be expressed as $F \approx \frac{g}{R}[T_l - T_m(r = R)]$ [98] (g is the interface thermal conductance, experimentally determined to be 105 MW m^{-2}K^{-1} for 35 nm gold in water [99], R is the particle radius. This resistance corresponds to a water thickness of 6.5 nm). The first and second lines describe the electron-phonon coupling in the gold nanoparticle. The third line is the equation of heat diffusion in the surrounding medium.

We numerically solve the above equations to see how the temperatures of these subsystems evolve with time. The result is shown in Fig.4.2. It confirms that electron-phonon coupling in the particle and phonon-phonon coupling between particle and liquid take place in subsequent time steps. The temperature of electrons shoots up by thousands of Kelvin after the excitation because of the small heat capacity of electrons. Then the electron and lattice equilibrate in a few picoseconds, while the heat exchange between hot lattice and surrounding water takes place subsequently within 100 ps because of the low water conductivity and the interfacial thermal resistance between gold nanoparticle and liquid. The temperature of the nearby liquid starts to rise around 100 ps after the excitation, and thermal energy will become available to the surrounding liquid for possible liquid ebullition and bubble formation if enough energy is injected. Therefore, in the present case of heating by the pump pulse only, the liquid cannot boil before it has received the pump energy through conduction. In our experiments described later, a major part or whole of the energy required for boiling is coming from the continuous heating beam, prior to triggering by the pump pulse.

Another interesting phenomenon accompanying lattice relaxation is the coherent vibrational motion of the gold lattice, which is excited by two main

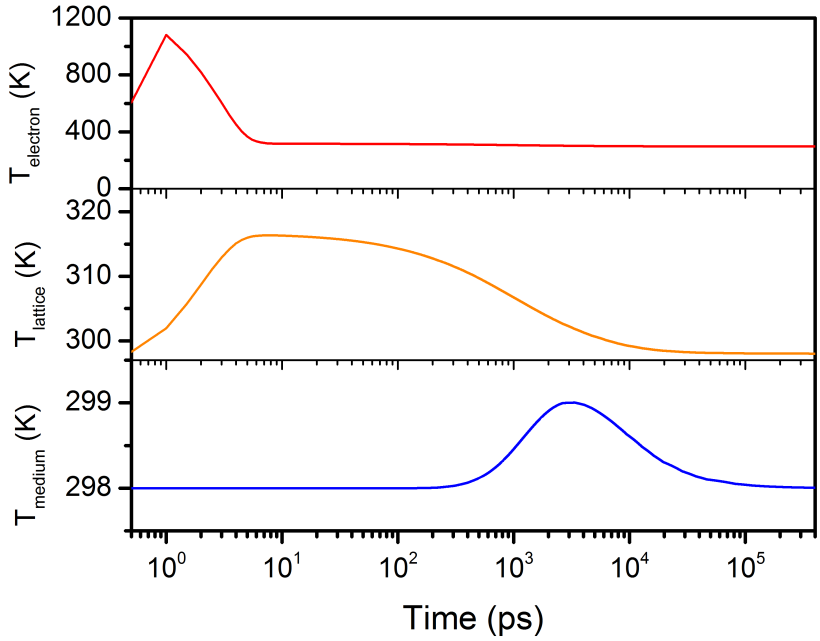

Figure 4.2: Calculated temperature evolution of the electrons (red, top), the lattice (orange, middle) and the surrounding water layer 1 nm away from the particle surface (blue, bottom) as a function of time upon femtosecond laser excitation. The fluence of the 785 nm 300 fs pulse is 5.3 mJ/cm^2. The initial temperature is set to 298 K.

mechanisms. First, the fast increase in the electronic temperature upon excitation leads to a sudden increase in Fermi pressure, which pushes the surface of the particle outward, giving an initial velocity to the expansion movement after cool down of the electrons. Second, the heating of the gold lattice consecutive to the electronic cool down leads to lattice expansion and to a new equilibrium radius. Both processes are faster than the typical period of the particle's breathing mode (about 17 ps for our 50 nm spheres). They both contribute to initial conditions different from equilibrium giving rise to the breathing oscillations of the particle.

The problem of the vibration motion of an elastic sphere has been theoretically solved by Lamb [100]. Two integers, the harmonic order n and angular momentum number l, describe the vibrational mode (n, l). For the spherical gold nanoparticles in our experiments, only the radially symmetric fundamental breathing mode (n, l)=(0, 0) will be excited. Lamb's theory may be complemented to find the vibrational frequency and the damping time of the breathing mode of an elastic gold sphere in an elastic medium according to the complex frequency model [101, 102]. These quantities are determined by the following

relations:

$$\omega_n + i\chi_n = \frac{\xi_n c_l^{(s)}}{R}, \tag{4.2}$$

$$\omega_n = Re(\xi_n)\frac{c_l^{(s)}}{R}, \qquad \chi_n = Im(\xi_n)\frac{c_l^{(s)}}{R}, \tag{4.3}$$

where ω_n is the vibration frequency; χ_n is the damping rate; R is the particle radius; $c_l^{(s)}$ is the longitudinal speed of sound in bulk gold. The complex eigenvalue ξ_n is determined by solving the following equation:

$$\xi cot\xi = 1 - (\frac{\xi^2}{\eta})\frac{1 + i\frac{\xi}{\alpha}}{\xi^2 - 4\alpha^2\zeta^2(1 - \frac{1}{\eta\beta^2})(1 + i\frac{\xi}{\alpha})}, \tag{4.4}$$

$$\alpha = c_l^{(m)}/c_l^{(s)}, \beta = c_t^{(m)}/c_t^{(s)}, \zeta = c_t^{(m)}/c_l^{(m)}, \eta = \rho^{(m)}/\rho^{(s)}, \tag{4.5}$$

where $c_{l,t}^{(m),(s)}$ are the longitudinal (l) and tranverse (t) sound velocity of matrix (m) and particle (s), $\rho^{(m),(s)}$ are the densities of water and gold.

Since the relaxation of excited electrons, lattice and nearby liquid take place in subsequent steps, we will look separately into the cooling kinetics of the gold nanoparticle, with and without a vapor nanobubble, depending on the heating power used. Note that the heating power we refer to is that of the continuous heating beam at 532 nm. The fluences of pump and probe pulses are low and kept constant during all measurements on the same particle. Control experiments show that, for the pump fluences we used, it was not possible to generate vapor bubbles without CW heating.

4.4. Results and discussion

4.4.1. Cooling kinetics of gold nanoparticle under variable CW heating power

In Fig.4.3, we show a typical pump-probe trace, measured without CW heating, of a 50 nm gold sphere immobilized on glass and immersed in pure water. The fluences of pump and probe pulses are low, and the initial temperature rise of the gold particle due to pump and probe pulsed heating are estimated according to the following equation [95]:

$$\Delta\ T|_{t=0} = \frac{\sigma_{abs} E_{pulse}}{A C_p V_p} \tag{4.6}$$

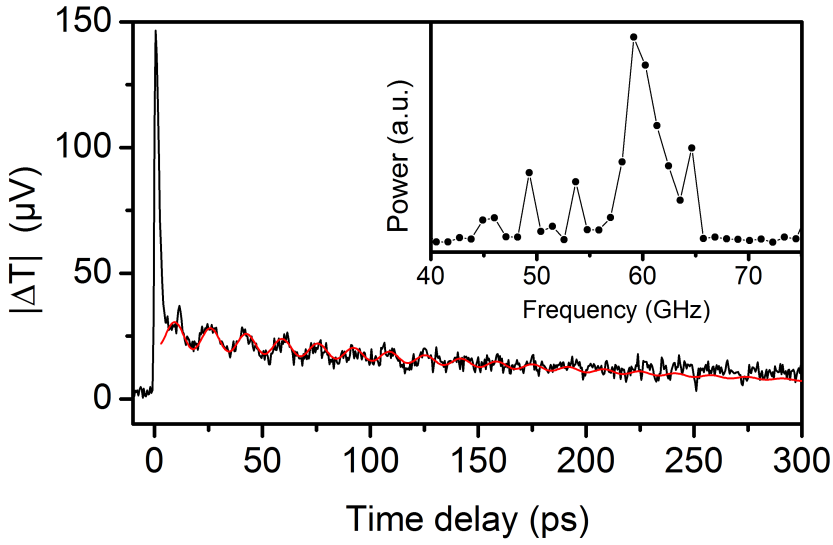

Figure 4.3: Time-resolved pump-probe trace of a 50 nm gold sphere immobilized on glass in water. There is no CW heating in this measurement. The red curve is a fitted curve showing the acoustic vibration of the single gold nanoparticle (with fitted parameters $\tau_1 = 283.3$ ps, $\tau_2 = 107.4$ ps, $A_1 = 26.5$ μV, $A_2 = 5.6$ μV, $T_{br} = 16.7$ ps, $\varphi = 2.7$ rad). The absolute value of the transmission change $|\Delta T|$ in the plot is the amplitude of the lock-in output. Insert: the power spectrum of the oscillatory part of the trace. The pump pulse energy at 785 nm with linear polarization is 26 pJ per pulse (average power is about 2 mW without transmission correction. The fluence is about 7.1 mJ/cm^2, assuming a diffraction-limited focal spot); the probe pulse energy at 597 nm is about 0.26 pJ (average power is 20 μW, fluence is about 0.1 mJ/cm^2). The integration time is 30 ms. All the powers and fluences mentioned in this chapter are measured before the objective.

where σ_{abs} is the absorption cross section of the gold particle, calculated from Mie theory, E_{pulse} is the energy of the incident pulse, A is the focus area assumed to have a diffraction-limited size; the absorbed energy E_{abs} is equal to $\sigma_{abs} E_{pulse}/A$; C_p and V_p are the specific heat capacity and the volume of the 50 nm diameter gold particle ($C_p = 24.9 \times 10^5$ J K^{-1}m^{-3}). The calculated temperature rises are shown in table 4.1. As mentioned earlier, three features, rep-

Table 4.1: Peak temperature rises of a gold nanoparticle generated by pump and probe lasers estimated from pulse fluences.

	σ_{abs}(nm^2)	E_{pulse}(pJ)	E_{abs}(fJ)	ΔT_p(K)
Pump at 785nm	65	26	4.6	28
Probe at 595nm	1470	0.26	1.8	11

resenting the relaxations of electrons, lattice and surrounding liquid are clearly visible in the trace of Fig.4.3. The sharp increase at zero time delay (the time when pump and probe pulses are overlapped in time) stems from the excited hot electrons in the metal, which shift and broaden the surface plasmon resonance of the gold nanoparticle. Coupling between hot electrons and lattice phonons follows, and the two subsystems reach equilibrium in about 2 ps. A subsequent damped oscillation is observed from tens to about one hundred picoseconds because of the excitation of the acoustic breathing mode which periodically shifts the SPR and modulates the transmission at the probe wavelength. The slow decay at longer time scales arises from the cooling of the gold particle due to heat exchange with the surrounding water. The vibration frequency of the breathing mode (0, 0) is about 60 GHz, as shown in the Fourier transform spectrum in the insert of Fig.4.3. It corresponds to an oscillation time of about 16.7 ps. This measured frequency corresponds to the breathing mode of a gold sphere of 54 nm diameter [48].

We fit the oscillatory part in the trace with the following phenomenological equation [95]:

$$\Delta T(t) = A_1 Exp(-\frac{t}{\tau_1}) + A_2 Exp(-\frac{t}{\tau_2}) cos(\frac{2\pi t}{T_{br}} + \varphi), \tag{4.7}$$

where the exponential term reflects the optical contrast of particle cooling and the accompanying heating of the surrounding liquid, and τ_1 is the characteristic time of this exponential decay. The damped cosine term reflects the damped oscillation of the breathing mode. The quantities τ_2, T_{br}, φ are the characteristic decay time, vibrational period and phase of the damped oscillation. The constants A_1 and A_2 are the proportionality constants. Cooling of the particle is controlled by both interfacial thermal resistance between particle and matrix and heat diffusion in the surrounding medium [103]. The interfacial thermal resistance will dominate at short times, and the particle temperature change will decay exponentially [99, 104]. At longer time scales, heat diffusion in the surrounding medium will dominate the cooling [105], and the temperature of the particle should decrease as $t^{-3/2}$ at very long times [106], which is in qualitative agreement with the experimental results in ref.[105]. In the regime governed by the interfacial resistance, the cooling time is proportional to the particle radius [99]. We see a deviation from the exponential fit at long time delays in Fig.4.3, but we nevertheless fit the oscillation part with Eq.4.7 in the following, for simplicity.

We performed pump-probe measurements on single nanoparticles with variable CW heating powers from zero to a power very close to, but lower than the boiling threshold of water. We then extract the parameters of the decay by fit-

ting the damped oscillatory part in a trace with Eq.4.7. The results of two particles are shown in Fig.4.4. As we can see from Fig.4.4 (a, d), for both particles, the

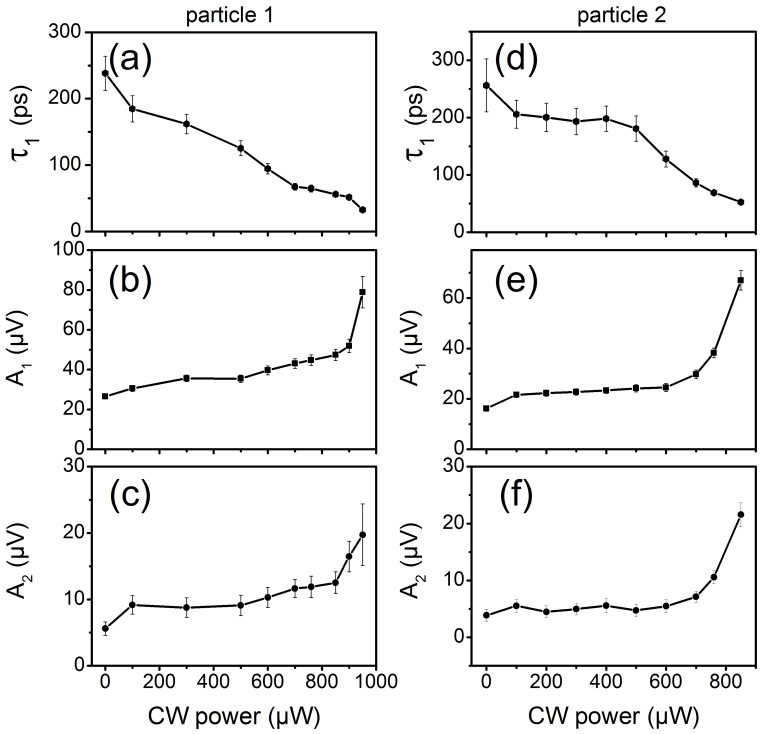

Figure 4.4: Parameters extracted from the fitting of the oscillatory part in the traces under variable CW heating powers. (a, b, c) show the changes of the characteristic decay time τ_1, and of the proportionality coefficients A_1 and A_2 as functions of the CW heating power. Measurements (a,b,c) were done on one particle and (d, e, f) on a second particle. For each particle, the pump and probe fluences remained the same in all measurements. The error bars in the plots represent the fitting uncertainty.

characteristic decay time τ_1 decreases steeply with the increase of CW heating powers. We do not think that this could result from any change of the interfacial thermal resistance at high heating power. The interfacial thermal resistance is related to the acoustic impedance mismatch of two contacting materials: Z_2/Z_1 [103], where $Z = \rho v$ is the acoustic impedance, ρ the density, v is the sound velocity of each material. The acoustic impedance of gold is almost independent of temperature below its melting point, while the acoustic impedance of water only decreases with temperature (both the sound velocity and the density decrease at high temperature). Therefore, we attribute this change in the characteristic decay time (τ_1) to the complexity of the optical signal in the strongly

inhomogeneous medium.

At heating powers less than 800 (600) μW for particle 1 (2), we can see a linear change in the proportionality coefficient A_1 which reflects the continuous heating of nearby liquid around the particle. Above a given threshold around 900 μW for particle 1 and 700 μW for particle 2, the proportionality coefficient A_1 increases suddenly to a much higher value. A similar sudden increase in slope was observed in our photothermal study of vapor nanobubbles [30], and we attributed it to the boiling of the nearby liquid and the formation of a vapor bubble. The estimated temperature of the gold particle from the threshold heating power is also close to the expected boiling temperature of water into a vapor nanobubble, calculated from the simple thermodynamic model (see Chapter 2 and Appendix C). We notice that the optical contrast of the acoustic vibration A_2 also becomes much higher above this threshold. Because we expect the vibration amplitude not to depend too strongly on the density of the medium surrounding the particle (the gold is much heavier than water and water steam), we attribute the change of A_2 to a plasmonic effect. When the bubble forms around the particle, there is a large refractive index change surrounding the particle. This will shift the SPR of the particle and largely change the extinction at probe wavelength. The changes in the extinction are more pronounced when the probe wavelength is on the red wing of the SPR peak, which is the case in our current measurements. Other fitted parameters such as τ_2, T_{br} and φ do not show much dependence on the CW heating power.

4.4.2. Time-resolved trace of vapor bubbles at high heating power

The kinetics of the optical signal upon cooling of the gold nanoparticle strongly suggests that at a high heating power close to the boiling threshold, a vapor bubble forms around the particle under the trigger pulses. Now we will look at the pump-probe traces in this regime of the vapor bubble.

In Fig.4.5, we plot the time-resolved traces of vapor bubbles from -10 ps to 900 ps time delays, as shown by the red curves. The two red traces are recorded with two different gold nanoparticles. The black curves in both plots are the pump-probe trace without CW heating, and are shown for comparison. We confirm the formation of vapor nanobubbles based on the following facts: first, we record traces at different CW heating powers, and we only observe such reproducible bubble traces when the heating power is high enough (see control experiments as the black curves). Second, the temperature rise of the gold particle calculated from the measured powers is close to the expected boiling temperature of water in nanobubble conditions (see details in Chapter 2 and Appendix C). Third, the contrast of the acoustic vibration of the particle be-

comes much stronger. Moreover, the damping decreases, leading to longer decay times, which is expected when the viscous damping of liquid water is removed (compare oscillations in the red and black curves). This could indicate an enhancement of the optical signal (the optical contrast of the acoustic vibration) by the index jump at particle-liquid interface caused by the bubble formation. The appearance of a vapor bubble enhances the extinction (SPR) changes of the gold particle at the probe wavelength. In a way, the bubble acts as an acousto-optical or acousto-plasmonic transducer for particle vibrations. Previous experiments with pump-probe spectroscopy on ensembles of gold nanoparticles in water found related results [107]. Signal enhancement at longer time delays was assigned to vapor bubble formation. The pump fluence found in these experiments also matched the threshold of explosive boiling of surrounding water [107].

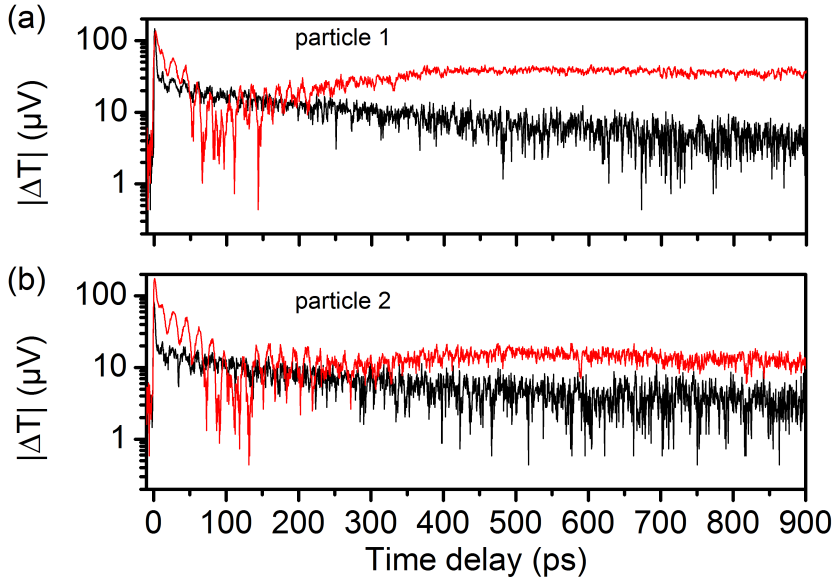

Figure 4.5: Two examples of transient traces of vapor nanobubbles measured by pump-probe spectroscopy for two particles in (a) and (b). The red traces with pronounced oscillations are obtained in the high heating power regime, when the bubble is thought to form (heating power 950 μW in (a), 850 μW in (b)). The black curves with more regular decays are the traces without CW heating for comparison. Note the more complex decay and the enhanced contrast of the breathing oscillations in the bubble traces. In all measurements, the pump and probe fluences remained the same (about 26 pJ per pulse at 785 nm and about 0.4 pJ per pulse at 597 nm). The integration time at each pixel is 30 ms.

We noticed that there is a characteristic interference feature in the bubble traces of Fig.4.5. The optical signal and extinction change sign at around 100 ps

after the pump triggering (zero time delay). Note that in the current measurements, we only record the absolute value (or the modulus) of the changes in the probe intensity which is the amplitude of the lock-in output. We attribute this interference feature to the bubble-size dependence of the total extinction of vapor bubble and gold nanoparticle. We calculated the extinction cross section of a vapor nanobubble around a 50 nm gold sphere at probe wavelength as a function of the vapor thickness using Mie theory, and we found that the extinction cross section first decreases steeply with the bubble thickness, reaches a minimum, and then increases when the bubble becomes much bigger. This can be understood by the fact that when the bubble grows and remains relatively small, the negative relative polarizability of the thin vapor shell will cancel out the positive relative polarizability of the gold nanoparticle. The whole system becomes less polarizable, and the total polarizability will decrease with bubble size. As the bubble grows further and overcomes a certain size where the extinction is minimal, the size of the vapor bubble becomes so large that it will optically "screen" the particle and dominate the extinction. The critical size or bubble thickness is found to be comparable to the size of particle radius. We tried to fit our data with the calculated extinction cross section, assuming the size of the vapor bubble goes linearly with time. We found the fitting can "reproduce" the interference feature very well. So the interference feature observed in the traces results from the dependence of the total extinction on the bubble size.

We also observed that the extinction signal when a vapor bubble forms around the gold particle is not very high, even though it is clearly different from the extinction at low heating powers. This suggests that the bubble is not very extended in size compared to the particle, at least during the first nanosecond. In principle, if a large vapor bubble forms around the gold particle, we expect a large SPR shift and a large scattering/extinction change at the probe wavelength. An alternative explanation for the relative weakness of the transmission change would be that not all pump pulses lead to bubbles, or that a jitter due to nucleation [3] broadens and weakens the transmission change. Pump-probe spectroscopy is based on stroboscopic measurements, which require good synchronization between a trigger pulse and the transient phenomenon under study. However, if the bubble is triggered acoustically by the particle's vibrations, the jitter should be negligible. Indeed, the jitter in our measurements seems not to be significant, as the extinction in Fig.4.5 goes all the way down to the minimum close to zero in both bubble traces of particle 1 and 2. Otherwise the extinction will become flattened if the jitter is large.

At this stage, we do not completely understand the dynamics of the vapor nanobubbles we observe in our experiments, and there are a number of open

questions, which require more detailed studies in the near future. For example, what is the size of the vapor bubble? How to explain the signal changes around 300 ps in Fig.4.5 (b), which is not present in Fig.4.5 (a)? Does the vapor bubble continue to grow or collapse at a certain point? A theoretical modeling of thermodynamics of vapor bubbles considering both pulsed and continuous heating will help understand the temporal profile of vapor bubble, while relating the extinction data measured in experiments with the thermodynamic modeling through Mie theory [108] can provide information such as bubble size, temperature and pressure. However, because this problem requires complex near-field optical simulations and modeling of ultrafast dynamics of soft matter at a phase transition, the calculations required were too complex to be performed within the limited time span of this work.

4.5. Conclusions

Combining pump-probe spectroscopy and continuous heating, we studied vapor bubbles in water around a 50 nm gold sphere with picosecond time resolution for one nanosecond. We found that the acoustic vibration of a gold nanoparticle becomes less damped when a vapor bubble forms around the gold particle. The enhancement of the optical contrast of vibration-induced oscillations confirms that vapor bubbles can indeed enhance acousto-optical transduction. In this chapter, we presented preliminary results and a qualitative discussion. A more detailed theoretical modeling of the bubble's dynamics would shed light on the understanding of our data and of vapor bubble properties.

5

Enhanced photothermal contrast using near-critical xenon as transducing medium

Abstract– *We experimentally show that the photothermal contrast of 20 nm gold nanoparticles can be greatly enhanced up to thousand times using xenon close to the critical point as the transducing medium. The dependence of the photothermal signal on temperature and pressure of xenon as well as on the modulation frequency is examined and compared with the common liquid glycerol. The enhanced photothermal signal could be useful for single-molecule detection since molecules could survive for longer times in studies at lower excitation powers.*

5.1. Introduction

Photothermal microscopy is a high-sensitivity method based on the optical absorption and thermal properties of a sample [40]. Upon optical excitation, molecules absorb energy from incident photons, and subsequent non-radiative energy dissipation (into the local environment) results in sample heating and changes in the temperature, refractive index, and density of the surrounding medium. The heat-induced temperature/index gradient or thermal lens, which can diffract a second incoming beam, is ultimately the basis behind photothermal microscopy. Photothermal microscopy has several advantages when it is used as a detection modality. First, it is only sensitive to the heat that is dissipated by the absorbing centers. Weak scattering in the sample is discriminated from the signal [42]. Second, not all the absorbing molecules are fluorescent when they are excited, but they all dissipate energy from incident photons into their environment. Thus, photothermal microscopy can be used to detect non-fluorescent absorbing nano-objects. For gold nanoparticles, the scattering cross section scales as the sixth power of particle size, while the absorption cross section only goes as the third power of size. Therefore, photothermal microscopy is particularly suitable for probing small gold nanoparticles. Over the past decade, photothermal microscopy has enabled the study of different types of nano-objects such as noble metallic nanoparticles [43, 44, 49], quantum dots [109], single organic molecules [45], and single-wall carbon nanotubes [110].

In principle, the photothermal signal is proportional to the electromagnetic field scattered by the refractive index gradient induced by the modulated heating, and can be written as follows [42]:

$$S \approx \frac{1}{\pi\omega_0} n \left.\frac{\partial n}{\partial T}\right|_p \frac{1}{C_p \lambda^2 \Omega} \frac{\sigma_{abs}}{A} P_{heat} P_{probe} \Delta t, \tag{5.1}$$

where S is the photothermal signal, ω_0 is the focal radius of the probe beam, n is the refractive index of the surrounding medium, λ is the probe wavelength, Ω is the modulation frequency, σ_{abs} is the absorption cross section of the target object, A is the focal area of the heating beam, P_{heat} and P_{probe} are the heating and probe power at the sample respectively, and Δt is the integration time of the lock-in amplifier. If the noise in the experiment is dominated by the shot noise (ideal case), then the signal to noise ratio (SNR) can be written as:

$$SNR \approx \frac{1}{\pi\omega_0} n \left.\frac{\partial n}{\partial T}\right|_p \frac{1}{C_p \lambda^2 \Omega} \frac{\sigma_{abs}}{A} P_{heat} \sqrt{\frac{P_{probe} \Delta t}{h\upsilon}}, \tag{5.2}$$

where h is Planck's constant, υ is the frequency of probe beam. By optimizing the above parameters such as heating and probe powers, integration time and

by choosing a good transducing medium with large $\partial n/\partial T$, the photothermal contrast can be optimized [42].

Common liquids such as water and glycerol typically have $\partial n/\partial T \approx 10^{-4}$ K^{-1} (in the following, we denote the isobaric coefficient as $\partial n/\partial T$). However, close to the critical point, fluids exhibit large changes in compressibility, density, specific heat, and thermal conductivity in response to small changes in temperature or pressure. Thus, $\partial n/\partial T$ of fluids diverges at the critical point. Therefore, we expect a larger photothermal signal if a critical fluid is used as the transducing medium for the photothermal microscopy. Carbon dioxide and water are commonly used as supercritical fluids to dissolve and extract substances [111, 112]. Xenon is an inert gas with its critical point at 289.733 K, 5.842 MPa [65], conditions which are not too difficult to implement experimentally. So we choose (supercritical) xenon in our experiments as the transducing medium.

In this chapter, we show the design of a high-pressure cell which can be integrated onto a conventional confocal microscope with a high N.A. objective, and experimentally demonstrate that photothermal contrast can be greatly enhanced (up to thousand times) using xenon close to its critical point as the transducing medium. We use small gold nanoparticles as the absorbing objects, and characterize the photothermal signals of gold nanoparticles in xenon under variable conditions of temperature and pressure. We also compare the signal in supercritical xenon with that in the common liquid glycerol, and examine the dependence of the photothermal signal on the modulation frequency. Enhanced photothermal contrast could have many applications, such as single-molecule detection, since much less excitation powers can be exploited to get a good photothermal contrast while the molecules do not suffer severe photobleaching.

5.2. Evaluation of $-\partial n/\partial T$ and enhancement factor in xenon

We first evaluate two terms that are important in determining the photothermal signal in the supercritical xenon. Those are the derivative of the refractive index with respect to temperature: $-\partial n/\partial T$, and the ratio between $-\partial n/\partial T$ and the thermal conductivity κ of xenon. We will use the data from the standard chemical database NIST website [65]. The derivative $-\partial n/\partial T$ characterizes the thermal expansion of a transducing medium, while a smaller thermal conductivity κ will lead to a better thermal confinement, and to a larger signal. Therefore, we use the ratio $-(\frac{1}{\kappa})\frac{\partial n}{\partial T}$ to characterize the enhancement in photothermal signal. We call it enhancement factor in what follows.

In Fig.5.1, we plot a set of isobaric curves showing the density of xenon as a

function of temperature at different pressures near the critical point.

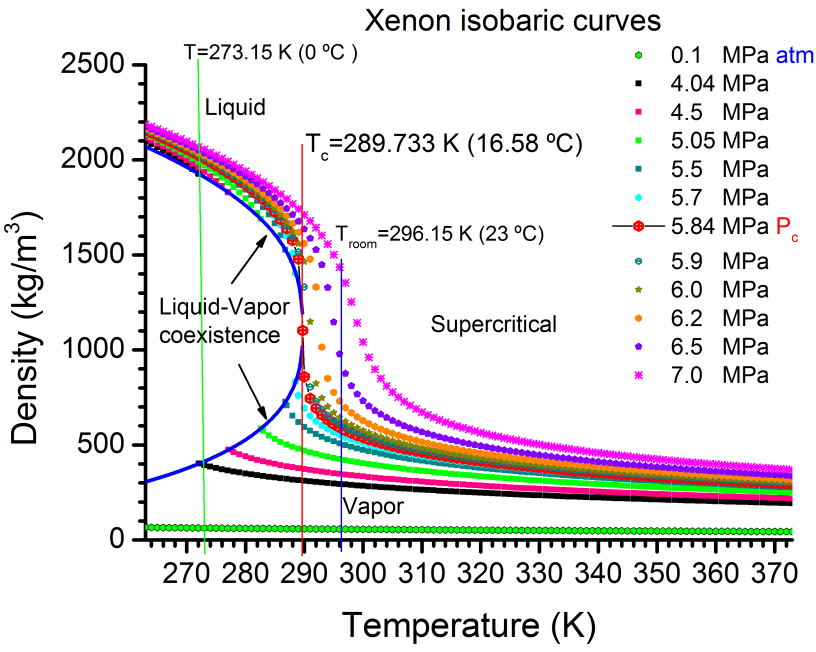

Figure 5.1: A set of isobaric curves (density vs. temperature) of Xe close to the critical point. Different colors and labels represent different pressures. The blue curve is the liquid-vapor coexistence curve. Above this curve, xenon is in the liquid phase; below the coexistence curve xenon is in the vapor phase. To the right of coexistence curve, xenon is in the supercritical state. The three vertical lines are the three typical temperatures: 273.15 K (green), critical temperature of xenon 289.733 K (red), and the ambient temperature 296.15 K (blue). Data are from ref.[65].

The slope of each isobaric curve, representing $\partial\rho/\partial T$ at a particular temperature and pressure, can be evaluated from these curves. $\partial\rho/\partial T$ can be converted to $-\partial n/\partial T$ using the Lorentz-Lorenz function [113]. Then we will get $-\partial n/\partial T$ as a function of temperature at different pressures. The Lorentz-Lorenz function (LL) states that the refractive index n of homogeneous non-polar medium is related to its density ρ and polarizability α. It is written as follows:

$$\frac{n^2-1}{n^2+2}\frac{1}{\rho}=\frac{4\pi N_0\alpha}{3M}=LL, \tag{5.3}$$

where n is the refractive index, ρ is the density in kg m^{-3}, M is molecular weight and N_0 is Avogadro's number. The LL function has been measured in xenon over a wide range of density and was found about 8×10^{-5} kg^{-1}m^3 at the critical point [113]. We will use this number in the following discussions. By differentiating the above equation on both sides with respect to the temperature T, we

can get the following expression [114]:

$$\frac{\partial n}{\partial T} = \frac{3LL}{2\sqrt{(1+2\rho LL)(1-\rho LL)^3}} \frac{\partial \rho}{\partial T}, \tag{5.4}$$

The derivative $-\partial n/\partial T$ and the enhancement factor calculated with Eq.5.4 and the data from Fig.5.1 are shown in Fig.5.2.

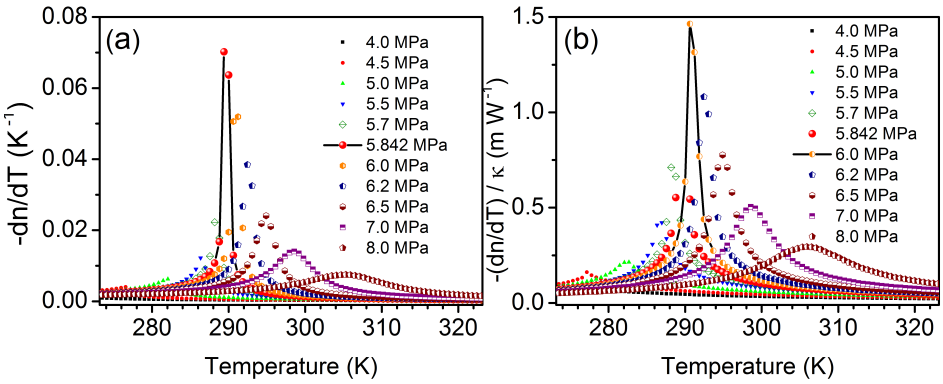

Figure 5.2: A set of isobaric curves showing $-dn/dT$ and enhancement factor in S.I. units as functions of Xe temperatures at different pressures. (a): temperature dependence of $-dn/dT$ under variable pressures (in different colors and labels). The solid curve labels are under the critical pressure, at 5.842 MPa. Because the density and thermal conductivity close to the critical point are not available from NIST, there are less data points plotted on the curves close to the critical point. (b): the enhancement factor in xenon as a function of temperature under variable pressures.

As we can see from Fig.5.2, when temperature and pressure of xenon approach the critical point, both $-\partial n/\partial T$ and the enhancement factor increase and $-\partial n/\partial T$ diverges at the critical point. This is a characteristic property of a supercritical fluid. Close to the critical point, a small change in temperature and pressure can lead to a large difference in density due to the large compressibility of the supercritical fluid. Compared with 10^{-4} K^{-1} values of conventional transducing media, supercritical xenon exhibits at least two orders of magnitude higher $-\partial n/\partial T$. Thus a larger photothermal signal is expected when supercritical xenon is used as the transducing medium. However, we also need to consider the thermal conductivity of Xenon, which defines the thermal diffusion length at a given frequency. Fig.5.2 (b) shows the enhancement factor as a function of temperature at different pressures. We can see that the maximum of the enhancement factor slightly shifts to a higher temperature and pressure compared with the critical point. This is because the thermal conductivity of xenon also increases rapidly as temperature and pressure come close

to the critical point. When the temperature and pressure move away from the optimal conditions (about 5.9 MPa, 290.6 K), the enhancement factor drops significantly but still remains much higher than in normal transducing media such as glycerol and water at ambient conditions.

Note that there are uncertainties in the evaluation of $-\partial n/\partial T$ and enhancement factor in xenon when data from NIST are used, because of the lack of data close to the critical point and the numerical errors in the derivative calculations. So Fig.5.2 should only be seen as a qualitative prediction of the thermal properties of xenon.

5.3. Experimental details

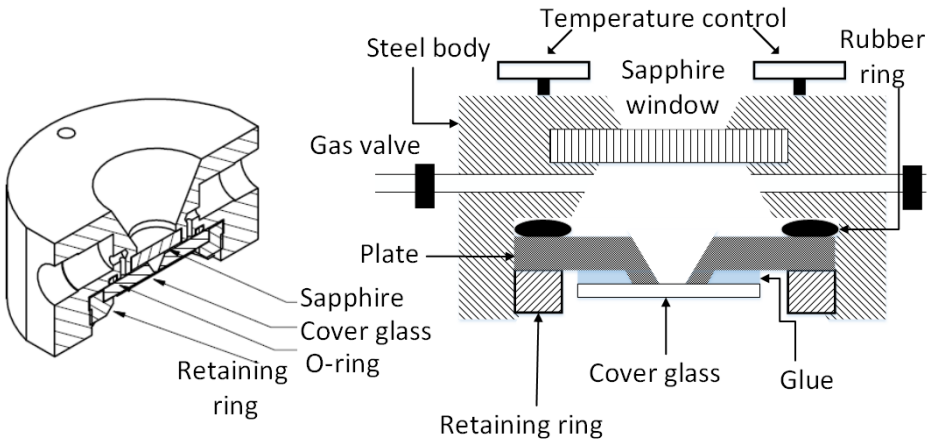

Figure 5.3: Scheme of the pressure cell used for the photothermal measurements in supercritical xenon. Left: top view of the cell; right: the cross section of the cell

The detailed description of the photothermal setup and sample preparation can be found in Chapter 3. Briefly, for sample preparation, single gold nanoparticles with diameter 20 nm are spin-coated on a clean cover glass. We adopt the design of ref.[115] and fabricate a high-pressure cell, which can be integrated into an inverted microscope with a high N.A. objective (Olympus, 60×, N.A.= 1.45). The scheme of the pressure cell is shown in Fig.5.3. The pressure cell body is made of stainless steel. On the top, a thick sapphire plate is glued to the body for alignment and to release unabsorbed light. For the objective side, a steel plate with a hole and a glued thin cover glass is retained onto the body by a metallic ring. The space enclosed by the two plates and the steel body is the gas chamber. Gases can be flushed into the pressure cell through the steel pipes and retained in the cell by the gas valves. The optimal diameter of thin

glass window D is calculated using the following equation [115]:

$$D = 2\,t_g \sqrt{\frac{P_{edge}}{P_{cell} \times 0.75}} \tag{5.5}$$

where t_g is cover glass thickness, P_{edge} is the edge stress of the glass, estimated to be around 58.6 MPa [115], P_{cell} is the working pressure of the pressure cell, and the constant 0.75 is empirically determined [116]. The cover glass we used has an average thickness around 0.18 mm. From the above equation, we can have a working pressure up to 18 MPa if we use a 0.75 mm diameter optical window. For the experiments in supercritical xenon, we need a minimal working pressure of about 6 MPa. Then the maximal diameter of the sample glass window is calculated to be 1.3 mm. We can tune the size of the optical window by changing the hole size of the metallic plate according to the working pressure.

A cover glass (thickness in the range of 0.16-0.19 mm) with coated samples is glued to the home-built high-pressure cell with an optical window of 0.75 mm diameter (See scheme in Fig.5.3). There is also a temperature control on the cell, which allows temperature tuning from about 286 K to ambient temperature 296 K. For the measurements in the pressure cell, first we test the quality of our glued sample by applying high pressure nitrogen to the pressure cell. Once no damage of the sample slide and no gas leakage are found in about one hour, we flush the cell with pure xenon for a few seconds in order to get rid of dust or impurities in the cell. Then we increase or change the pressure of xenon by applying pressure to a piston in a cylinder where xenon is compressed. The high-pressure cell is mounted on a three dimensional scanning piezo stage, and gold particles are located with the photothermal microscope. An intensity-modulated 532 nm CW beam is used to heat the gold nanoparticles, and a CW beam at 815 nm is used as the probe beam for the photothermal detection. A fast photodiode and a lock-in amplifier are used to pick up the photothermal signal. A typical integration time is 10 ms per pixel, and a typical imaging area is $15 \times 15\ \mu m^2$. We vary the pressure and temperature in the xenon cell, then scan the same area and record the photothermal images under same heating and probe powers. Post processing of images includes the subtraction of the background where there are no particles, fitting intensity of each spot with a two-dimensional Gaussian function and statistics such as mean value and distribution of the signals.

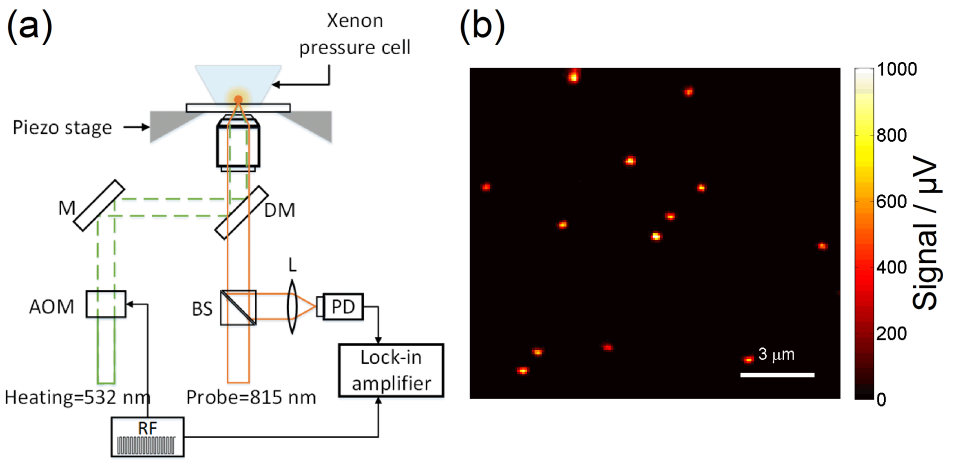

Figure 5.4: Experimental setup and the photothermal image of 20 nm gold nanoparticles on a cover glass in supercritical xenon. (a): scheme of the optical setup. AOM: acousto-optics modulator; DM: dichroic mirror; PD: photodiode; RF: signal generator. (b): photothermal image of 20 nm gold nanoparticles in supercritical xenon. The heating power used is 4 μW at 532 nm; the probe power is 15 mW at a wavelength of 815 nm. All the powers mentioned were measured at the back aperture of the objective. The integration time at each pixel is 10 ms, and the modulation frequency in this case is 50 kHz. The image has been background-corrected by subtracting the average signal over an area where there are no particles. The pressure and temperature in the xenon cell are 6.21 MPa and 287 K respectively.

5.4. Results and discussion

The scheme of the optical setup is shown in Fig.5.4 (a). Fig.5.4 (b) shows the typical photothermal image of 20 nm gold nanoparticles deposited on the glass in the supercritical xenon environment. With only about 4 μW heating power, 15 mW probe power, and 10 ms integration time, we got an averaged photothermal contrast as high as 0.8 mV against the background (3.5 μV, has been subtracted from Fig.5.4.b) for a 20 nm gold particle. Compared with the results formerly reported by our group [42], the photothermal signal normalized by heating and probe powers in supercritical xenon improves by at least a hundred times (note that former measurements were done in glycerol, alignment and modulation frequency are different). The signal to noise ratio (SNR) here is about 400. Normalized by powers and by the integration time, this ratio is about 20 times that in glycerol in Ref.[42]. The noise in the measurements could originate from the power fluctuation of probe intensity, photon noise (shot noise) in the probe due to the quantum nature of photons, and thermal noise in the photodetector. All of them could contribute to the total noise in the photothermal signal and could be "amplified" by the supercritical xenon. Thus, the gain in SNR is

less impressive than the gain in sensitivity (signal with respect to background). However, the big advantage of using supercritical xenon is that much less heating power is required because the photothermal contrast still remains good at low heating power. This will facilitate single-molecule detection because the photobleaching time of the molecules will be accordingly lengthened. The absorbed power in Fig.5.4 (b) is estimated to be around 4 nW, and the temperature rise of the gold particle surface to about 0.8 K.

Under the same powers, integration time, and modulation frequency, we vary the pressure and temperature of the xenon cell to check the signal dependence on these two parameters. We image the same area under each temperature and pressure conditions, and get the averaged photothermal signal in one image. Then we plot the averaged signal as a function of temperature and pressure in a two-dimensional color-coded map, as shown in Fig.5.5.

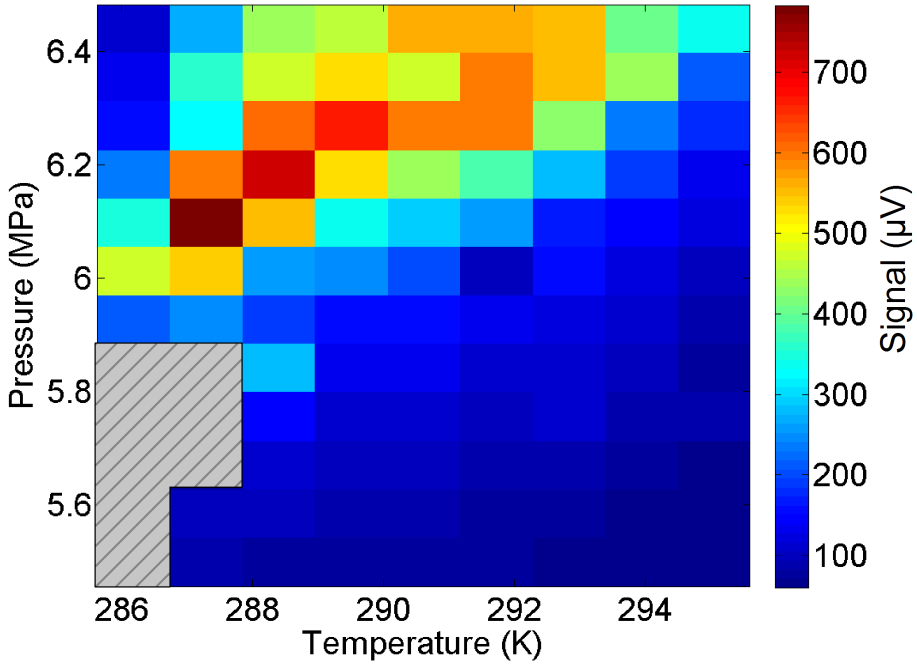

Figure 5.5: Photothermal signal of 20 nm gold particles in xenon under variable temperature and pressure of the xenon cell. Each pixel is the averaged signal over 13 particles in one image. The averaged signals have been corrected by subtracting the background. The heating beam (532 nm) is modulated at 50 kHz, the power at the back focal plane of the objective is 4 μW; the probe power is 15 mW at 815 nm. The integration time is 10 ms. There are no data measured in the hatched region in the left corner from (286 K, 5.5 MPa) to (288 K, 5.8 MPa).

As expected, the photothermal signal indeed significantly increases when

the temperature and pressure of xenon approach to the critical point (5.842 MPa, 289.733 K). The maximal signal in the measurements is found under conditions around 6.1 MPa and 287 K, slightly different from the optimal conditions calculated with NIST data in the Section 5.2 (5.9 MPa, 290.6 K). The slight difference could be due to the following reasons. First, the local temperature of the gold nanoparticle is different from the temperature measured in the experiments (the pressure cell temperature), and the probe beam could also induce some heating of the gold nanoparticle because of the non-negligible absorption at the probe wavelength; Second, xenon purity in the cell might change slightly from measurement to measurement even though the cell is always flushed with xenon before each measurement.

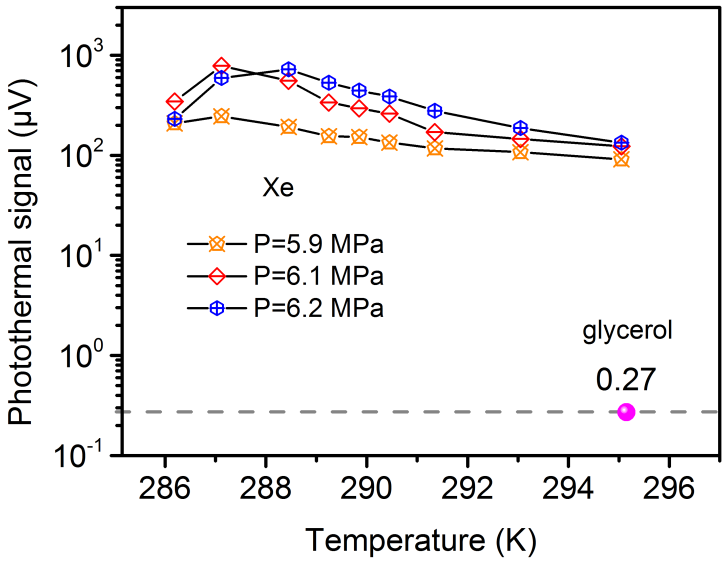

Figure 5.6: Three isobaric curves (in different colors and labels) showing the photothermal signal as a function of temperature of the xenon cell above the critical pressure. Orange circle with cross: at pressure 5.9 MPa; red rhombus: at pressure 6.1 MPa; blue circle with plus: at pressure 6.2 MPa. The pink dot in the right corner represents the typical normalized photothermal signal of 20 nm gold particles averaged over 11 particles when glycerol is used as the transducing medium at ambient conditions.

We cut a number of lines along the temperature axis in Fig.5.5 and get serials of isobaric curves of photothermal signals as a function of the xenon cell temperature, as shown in Fig.5.6. We can see that the signal drops by about a factor of 7 when temperature moves away from the optimal conditions to well above the critical point, even though xenon is in the supercritical state in both cases. We also indicate the photothermal signal of 20 nm gold particles

in glycerol under ambient conditions (295 K, 0.1 MPa), normalized to the same laser powers used in xenon. The maximum photothermal signal in supercritical xenon is three orders of magnitude higher than that in glycerol. Even at the tails of curves where temperature and pressure are away from optimal conditions, photothermal contrast is still much higher than in glycerol because of the relatively large compressibility of the supercritical fluid compared with normal liquids. We can also compare the data of our measurements with the results obtained from NIST data, and a good agreement is found between the two results. (for glycerol, $-dn/dT$ is 2.7×10^{-4} K^{-1}, and thermal conductivity κ is 0.28 W m^{-1} K^{-1}, the $(-dn/dT)/\kappa$ is 9.6×10^{-4} in S. I. units. The maximum enhancement number $(-dn/dT)/\kappa$ from the NIST data in Fig.5.2, is 1.8 in S. I. units. Then the ratio of enhancement factor between Xe and glycerol is $1.8/9.6\times10^{-4}$ = 1900, of the same order of magnitude as we measure.)

We examine the modulation frequency dependence of the photothermal sig-

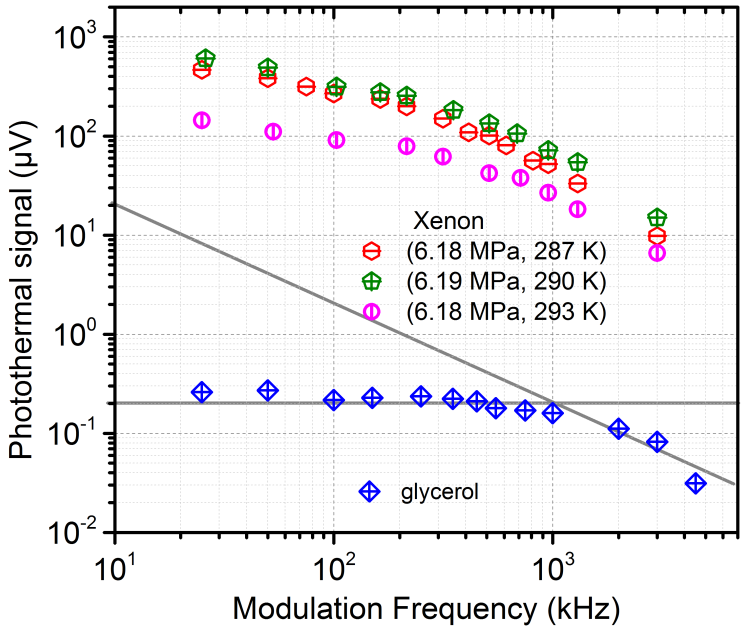

Figure 5.7: Modulation frequency dependence of photothermal signal of 20 nm gold nanoparticles in supercritical xenon and glycerol (blue diamonds). The three scatter plots represent three different temperatures of the xenon cell above critical pressure: (6.18 MPa, 287 K) red hexagons, (6.19 MPa, 290 K) green pentagons and (6.18 MPa, 293 K) pink circles. The heating power used is 4 μW; the probe power is 15 mW; integration time is 10 ms. Again, each point is the average photothermal signal over 13 particles in one image. The blue diamonds are the measurements in glycerol normalized to the same heating and powers as above. The cross point of two gray lines shows the cutoff frequency in glycerol.

nal in supercritical xenon and compare with the case of glycerol. The results are shown in Fig.5.7. The modulation frequency is tuned from 25 kHz to 2 MHz. In both cases of supercritical xenon and glycerol, the photothermal signals show a low-pass behavior, as reported previously in ref.[49]. The heat diffusion length r_{th} is related to the modulation frequency through the equation $r_{th} = \sqrt{2\kappa/C_p\Omega}$ [49], where κ is the thermal conductivity of the medium, C_p is the heat capacity per unit volume, and Ω is the modulation frequency of the heating beam.

At higher frequencies (higher than the corner frequency $\Omega_c = 2D(2\pi n/\lambda)^2$, where D is the thermal diffusivity, n is the refractive index, λ is the incident wavelength), the thermal diffusion length becomes much smaller than the focus waist of the probe beam, and the induced thermal lens is less efficient to scatter the probe beam. Thus the photothermal signal decreases as the modulation frequency increases. At lower modulation frequencies, the scattering object or thermal lens becomes much bigger than the point spread function of the probe beam, but as it efficiently scatters only in the probe focus, the signal saturates. Compared with the frequency dependence in glycerol with a corner frequency at round 1 MHz (see the crossing point of two grey lines in Fig.5.7), the photothermal signal in supercritical xenon does not show any clear corner frequency. Instead, it continues to increase with a lower slope as the modulation frequency decreases, similar to what has been observed in photothermal deflection measurements in supercritical xenon [117]. We assign the further increase of signal at lower frequency to "critical slowing down" effects in the phase transition when a substance approaches/crosses the critical point. The critical slowing down has been observed in many ferromagnetic systems [118]. These effects are related to the absence of clear length and time scales in critical fluids. Response functions such as the compressibility become infinite at the critical point, but only when averaging over long relaxation times. Similarly, the full extent of such fluctuations requires the participation of very long distances. Because of the finite modulation frequency and integration time of the measurements, we actually "catch" only a fraction of $-\partial n/\partial T$ of the fluctuations. The slower we modulate and the longer the integration times we use, the higher this fraction will be and the larger the critical enhancement effect. Based on this, one can, in principle, further increase the photothermal signal of gold nanoparticles in supercritical xenon by lowering the modulation frequency. However, at lower frequencies, all kinds of mechanical and laser intensity noises will become dominant, and the signal to noise ratio would degrade due to the increased noise level. Therefore, in the experiments, we aim for a trade-off between modulation frequency and signal-to-noise ratio in order to optimize measurements.

5.5. Conclusions

In this chapter, we experimentally demonstrated that the photothermal contrast of small gold nanoparticles (20 nm in diameter) can be greatly enhanced when supercritical xenon is used as the transducing medium for photothermal microscopy. We check the signal's dependence on xenon's temperature and pressure, and compare the signal in supercritical xenon with that in glycerol which is frequently used in our previous work. The signal in supercritical xenon is several orders of magnitude higher than that in glycerol near the critical point. The measured enhancement factor shows a qualitative agreement with the results calculated with NIST data. We also examine the modulation frequency dependence of the photothermal signal in supercritical xenon. It shows a continuous increase as the frequency decreases. A possible explanation is offered by the "critical slowing down" effect in a critical fluid. Both length and time scales diverge at the critical point. The enhanced photothermal contrast could be helpful in single-molecule detection, since much lower excitation powers can be used to study the absorption properties of molecules, while photo-bleaching is mitigated at lower power.

6

Simultaneous absorption and emission measurements of single conjugated polymers in near-critical xenon

Abstract– *We simultaneously measure the absorption and emission of single conjugated polymers poly[2-methoxy-5-(2-ethylhexyloxy)-1,4-phenylenevinylene] (MEH-PPV) using supercritical xenon to enhance the photothermal contrast for direct absorption measurements. We obtain a number of useful pieces of information such as the number of monomers in single conjugated polymer molecules and the apparent quantum yield of single-polymer molecules. Simultaneous absorption and emission measurements provide new insight into the exciton behavior in a conjugated polymer molecule under optical excitation.*

6.1. Introduction

Conjugated polymers represent an important class of organic materials widely used in applications such as organic light emitting devices (OLED) [60], solar energy conversion [61], thin-film transistors and chemical sensors [63]. It is widely accepted that the optical and electrical properties strongly depend on the microscopic structure of conjugated polymers chains and on the local surroundings [119]. Over the past decades, with the help of single-molecule fluorescence spectroscopy [120], extensive studies have been carried out aiming to resolve the relationship between the optical properties of the conjugated polymers and their conformation [62]. Barbara's group first applied single-molecule spectroscopy to study single conjugated PPV-PPyV polymers in polystyrene [121]. Surprisingly, they found that a single conjugated polymer that consists of many chromophores behaves like a single emitter. After examining many factors, they concluded that efficient intrachain energy transfer and changes in the quantum yield account for the single-emitter behavior. Since then, many approaches based on single-molecule fluorescence spectroscopy have been proposed and applied to conjugated polymer studies. A common approach is to measure the fluorescence time traces of single polymer chains with different time resolutions [122, 123] and under different experimental conditions, such as different polymer structures, molecular weights, solvents, matrix, sample preparations [122, 124–126]. Another important approach is the fluorescent excitation and emission polarization anisotropy measurements on conjugated molecules, combined with computer simulations [119] to characterize the anisotropic conformation properties [127, 128]. Room temperature [129, 130] and low temperature single-molecule spectroscopy [124, 129, 131] can spectrally resolve the interaction between chromophores in a conjugated polymer, providing a picture of the landscape of energy transfer. Time-resolved measurements can give information on the fast dynamics of excitons during "on" and "off" states, and thus indirectly yield insight into the excitons' migration along a single chain and the population of localization domains [132, 133]. Fluorescence correlation spectroscopy (FCS) has been used to study the solvent effect on the conformation of conjugated polymers in solution [134, 135], and dynamics of excitons under variable excitation power [136]. Combining far-field and near-field microscopy, researchers proposed to measure the absorption ellipsoid of single conjugated polymers [137]. Providing a few nm spatial resolution, AFM can be exploited to resolve the fine structure of some conjugated polymer molecules [138].

Single-molecule fluorescence spectroscopy allows researchers to study the emission and photophysics of a single polymer in great detail. However, directly

probing the absorption and non-radiative decay of excitons is still challenging. Measurements of polarization anisotropy could provide some information on the absorption and orientation of single dipole molecules, but conjugated molecules usually do not absorb and emit as single dipoles and polarization anisotropic measurements might not directly link to the absorption and conformation properties. On the other hand, information on the non-radiative channels of excitons can provide more insight into the quenching and dark states of conjugated molecules, thus clarifying some points of the debates that have arisen in previous studies.

Photothermal microscopy is a very useful tool for probing the local energy dissipation. Spatial sensitivity has been shown down to a 2.5 nm gold nanoparticle [44] and a single dye molecule [45]. Conventional photothermal microscopy relies on high optical excitation powers to reach single-molecule sensitivity [45]. However, such high powers limit the kind of detectable molecules to those resisting photo-bleaching at high excitation powers. In this chapter, we simultaneously measure the absorption and emission of single MEH-PPV conjugated polymers embedded in a PMMA matrix with a reasonably low excitation power using supercritical xenon as the transducing medium for the photothermal microscope. Close to its critical point, xenon exhibits divergent refractive index change with temperature, which greatly enhances the photothermal contrast (see Chapter 5). This allows the simultaneous detection of absorption and emission at much lower power (so that photobleaching becomes less significant). Our results yield for the first time the number of monomers and apparent quantum yield of a single conjugated polymer, and provide valuable information on the radiative and non-radiative decays of excitons in a conjugated molecule.

6.2. Experimental details

6.2.1. Optical setup

Simultaneous absorption and fluorescence measurements were performed on a home-built inverted microscope. A continuous-wave (CW) laser with a wavelength of 488 nm is modulated by an acousto-optic modulator at 53 kHz, and used to excite the conjugated polymer molecules. A CW laser beam with a wavelength of 815 nm is spatially overlapped with the excitation/heating beam. The two beams are both expanded to fill the back aperture of an oil immersion objective (Olympus, 60×, NA=1.45) and are focused on the sample-substrate interface. The reflected probe beam is collected by a photodiode (Femto DHPCA-100-F), and the signal is demodulated by a lock-in amplifier (SR844, Stanford Research Systems). The demodulated voltage signal gives the photothermal contrast. The fluorescence signal of the polymer molecules is collected by a

single-photon-counting avalanche photodetector (SPCM-AQR-16, Perkin-Elmer), and a set of filters are used to remove the excitation and probe beams.

6.2.2. Sample preparation

Cover glasses are cleaned with acetone, ethanol and Milli-Q water, separately. Then they are cleaned with ozone to remove all possible organic contamination. MEH-PPV polymers (with average molecular weight M_n about 150-250 kDa) and PMMA (with molecular weight M_n about 996 kDa) were bought from Sigma-Aldrich, and molecules of large molecular weight are selected by gel permeation chromatography (GPC) with $M_n = 2$ MDa and polydispersity 1.11. The PMMA was cleaned by precipitation in order to get rid of impurities [139]. Then PMMA was dissolved in toluene with concentration of about 1% w/w. High molecular weight fractions of MEH-PPV are dissolved in toluene with concentrations from 10^{-5} to 10^{-4} g/L, and further diluted ten times with PMMA solution. Then the mixture solution was spin-coated on a clean cover glass to obtain a film about 40 nm thick. The cover glass coated with MEH-PPV/PMMA is glued to a home-built high-pressure cell, leaving a clear aperture of about 0.75 mm diameter which is used for optical access. The high pressure is applied to xenon gas through narrow steel tubes and controlled with an auxiliary device (see Appendix B). The temperature of the whole cell is also controlled with a feedback device. We vary the temperature and pressure of xenon close to its critical point to achieve optimal sensitivity, and we use small gold nanoparticles to calibrate the photothermal signal (see Figure 6.1).

6.3. Results and discussion

In order to find the optimal conditions for the photothermal detection of single polymer molecules in xenon, we set out our measurements on small gold nanoparticles (20 nm in diameter) in xenon under variable temperature and pressure. We varied the temperature and pressure of xenon cell and we found that the best conditions for the photothermal contrast arise when the pressure and temperature of the xenon cell are about 6.1 MPa and 288 K, respectively (see Chapter 5 for more details). Note that the optimal conditions may change a bit for different measurements, probably because the purity of xenon in the pressure cell may not be exactly the same every time, even though the cell is flushed with xenon before each measurement. Figure 6.1 shows the histogram of photothermal contrast of 20 nm gold nanoparticles in xenon under 488 nm heating when the pressure and temperature are optimized. The distribution originates from the size deviation from 20 nm and the shape deviation from a sphere [42]. The mean photothermal signal (with respect to the background)

of 12 particles is 109±26 μV. This data will be used as calibration to deduce the absorption cross section of single conjugated polymers, since the absorption cross section of a gold nanosphere can be easily calculated using the Mie theory (for 20 nm gold sphere, the absorption cross section is about 175 nm^2 in xenon close to the critical point at 488 nm wavelength. Refractive index data ($n = 1.1379 \pm 0.0008$) are taken from ref.[113]).

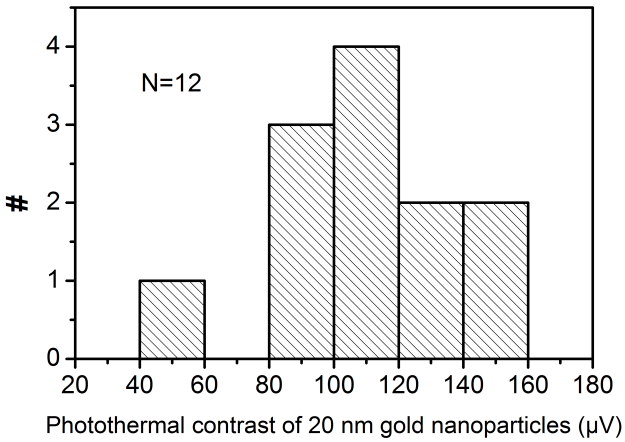

Figure 6.1: The histogram of the photothermal signal of 20 nm gold nanoparticles in near-critical xenon when the pressure and temperature are optimal (pressure is 6.1 MPa, temperature is 288 K). The heating power is 5 μW with a wavelength of 488 nm and linear polarization. The probe power is 15 mW at 815 nm. Powers are measured at the back focal plane of the objective (the objective transmission was not taken into account). Integration time is 10 ms, and heating modulation frequency is 53 kHz.

We simultaneously measured the absorption and emission of single MEH-PPV polymers embedded in PMMA using the enhanced photothermal setup. Typical confocal images are shown in Fig.6.2 (a) and (b). The excitation beam at 488 nm is circularly polarized in all the measurements discussed below. Single polymers show both fluorescence and absorption signals, and the big spots in both images are well correlated with each other. We scanned several different areas on the same sample, and we found 123 spots in the fluorescence image, 75 spots in the photothermal image and 60 correlated spots shown in both images. Some dimmer spots in the fluorescence image are not present in the photothermal image (one example is indicated by the dashed circles), probably because they have smaller molecular weight and low photothermal contrast which is beyond our current detection limit. Some spots that are present in the photothermal image do not show up in the fluorescence image, as shown in the dashed rectangular frame. This is possibly because of the photobleaching

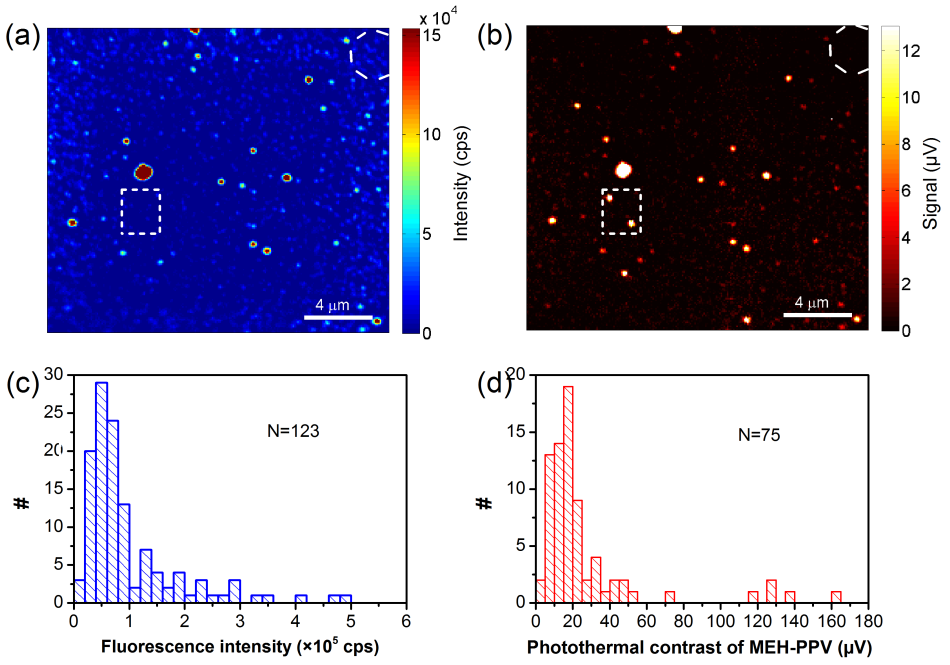

Figure 6.2: Simultaneous measurements of the emission and absorption of single MEH-PPV conjugated polymers under 488 nm excitation with circular polarization. a) confocal image of MEH-PPV's emission/fluorescence under 3.5 μW excitation power; b) simultaneous photothermal image of the same area. The heating power is 3.5 μW, the probe power is 15 mW, integration time per pixel is 10 ms. The pressure and temperature of the xenon cell are 6.1 MPa and 289 K respectively. c,d) the histogram of fluorescence intensity c) and photothermal signal d).

of molecules during the laser scanning. The excitation/heating power used is approximately 3 μW, corresponding to a power density of roughly 2 kW cm^{-2} (assuming the focused spot is diffraction-limited). The photothermal contrast of these polymer molecules is good enough, with average signal to noise ratio of about 55. We measured the two signals simultaneously on many spots, and plot the histograms of emission and absorption in Fig.6.2 (c) and (d). Both the emission and absorption show wide distributions probably due to the large molecular weight distribution and conformation heterogeneity, even though gel permeation chromatography (GPC) has been applied to sort out the polymers with relatively large molecular weight (see experimental details). Actually the molecular weight (MW) obtained from GPC does not truly reflect the molecular weight of the polymers in the matrix, as found and discussed in ref.[139]. This is because the concentration in these single-molecule experiments is much lower than that used in GPC, and the molecular weight of large conjugated

molecules is often overestimated in GPC due to the chain aggregation. The larger signals in the tail might be from some clusters and aggregates.

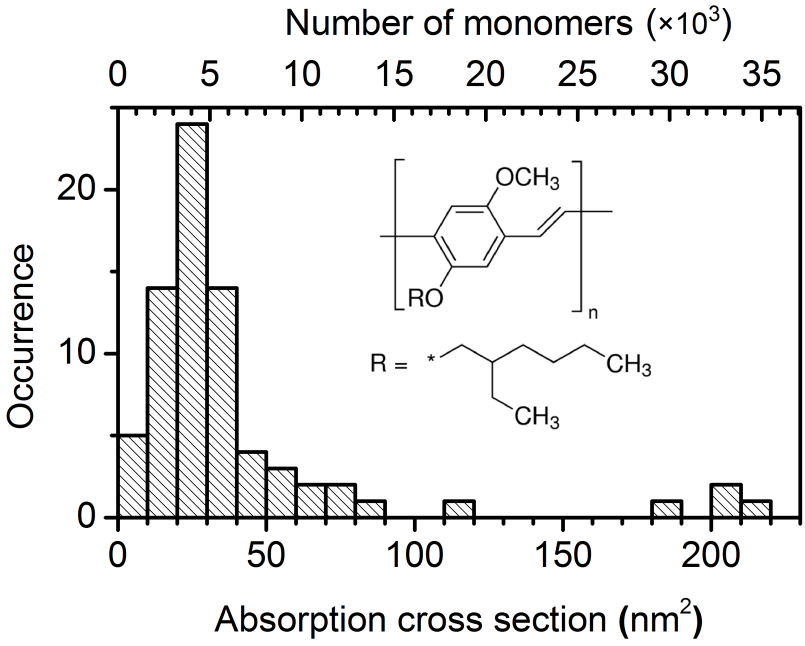

Figure 6.3: Estimation of the absorption cross section (lower axis)and the monomer numbers (top axis) of single MEH-PPV conjugated polymers in PMMA matrix based on the photothermal signal. Insert: chemical structure of the conjugated MEH-PPV molecule.

Now we can deduce the absorption cross section of a single polymer and the number of monomers in each polymer, based on the photothermal signal of polymer molecules and on the calibration data of 20 nm gold particles in Fig.6.1. Figure 6.3 shows the histogram of absorption cross sections of 75 polymer molecules. The mean value is about 40 nm^2 for the sample used. The wide distribution again reflects the size heterogeneity and/or aggregation of chains. Note that the histogram in Fig.6.3 may not fully reflect the distribution of the absorption cross section of these molecules because of the detection limit of current photothermal measurements. In order to have a reasonable photothermal signal, the SNR should not be smaller than 10 [42]. Then we estimate the minimum detectable absorption cross section to be around 8 nm^2 under current conditions. Since the absorption cross section of a monomer is about 6.2×10^{-3} nm^2 [140], the number of monomers in a single polymer molecule can be deduced from the absorption cross section, as shown on the top axis of Fig.6.3. The number of a few thousand monomers in a molecule is as ex-

pected from the sample preparation. To our best knowledge, our results are the first quantitative measurement of the monomer numbers in single conjugated polymers by photothermal microscopy. This useful information will help us to better estimate the quantum yield of a single polymer molecule.

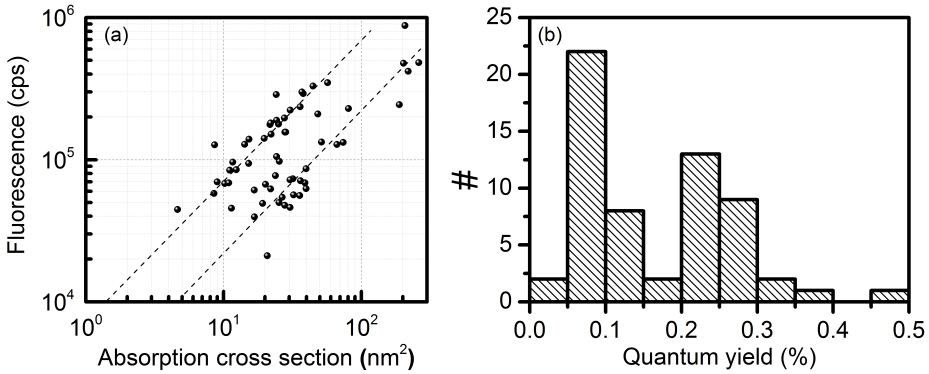

Figure 6.4: (a) Correlation plot of fluorescence brightness with absorption cross section. The dashed lines are guides for the eye with slope 1, where the data points are densely distributed. (b) Apparent quantum yield deduced from the correlated signals of (a).

With the knowledge of absorption and emission of a single conjugated polymer at hand, we can correlate these two signals and estimate the quantum yield of single polymers. In Fig.6.4 (a), we plot the fluorescent brightness as a function of the absorption cross section of polymer molecules. Each point represents a single polymer molecule that appears in both confocal images, 60 of them in the plot. There is a positive correlation between emission brightness and absorption cross section. The brighter the fluorescence is, the higher the absorption cross section of the polymer. The useful conclusion drawn here is that the brightness of fluorescence goes linearly with the number of monomers in a conjugated polymer molecule when the excitation power is low, as for our current measurements. Note that at high excitation powers, nonlinear behaviors of chromophores in a molecule such as singlet-singlet annihilation, singlet-triplet quenching and triplet-triplet annihilation will show up and become dominant. As the excitation power increases, fluorescence might get saturated or even decrease because of the build-up of long-lived triplet states and of increased possibilities of singlet-triplet quenching and singlet-singlet annihilation between chromophores [136, 141]. In the range of powers where these nonlinear effects take place, the dependence of the fluorescence on the number of monomers might not be linear any more. Additional measurements of the power dependence of both absorption and emission of polymer films and single molecules would be instructive to find out the linear power range. These

experiments are planned in the near future.

The quantum yield (QY) of an emitter is the ratio between the number of photons emitted and the number of photons absorbed under optical excitation, as written in Eq.6.1.

$$QY = \frac{N_{emit}}{N_{abs}}, \tag{6.1}$$

The total number of photons emitted N_{emit} in Eq.6.1 is the fluorescent signal divided by the detection efficiency of the setup (taking into account the transmission of all optics in the detection path and the efficiency of photon detectors), while the number of photons absorbed by a molecule N_{abs} is written as the ratio between absorbed power and incident photon energy:

$$N_{emit} = \frac{N_{fluo}}{\eta_{det}}, \tag{6.2}$$

$$N_{abs} = \frac{\sigma_{abs} I_{exc}}{h\nu_{exc}}, \tag{6.3}$$

where N_{fluo} is the measured fluorescence signal from a conjugated polymer molecule (counts per second); η_{det} is the detection efficiency of our current setup, and is estimated to be about 5% [141]; σ_{abs} is the absorption cross section of a single polymer molecule, deduced from the photothermal signal; I_{exc} and ν_{exc} are the excitation intensity at 488 nm and excitation frequency; h is the Planck constant.

In Fig.6.4 (b), we plot the histogram of apparent quantum yields for 60 molecules under 488 nm excitation. From the plot, two pieces of information are clearly visible. First, the distribution shows two peaks, possibly because two conformations dominate in the measured sample; Second, the quantum yields of these conjugated molecules are pretty low, a fraction of one percent, implying that there could be many "dark states" and non-radiative channels in the molecules under study. Greenham *et al.* [142] measured the absolute photoluminescence (PL) quantum efficiency of several conjugated polymers films, and the PL efficiency of MEH-PPV films is found to be in the range of (0.1-0.15) ± 0.01 under 488 nm excitation, and efficiency decreases with time under ambient laboratory conditions. The storage condition could account for the low quantum yield we find since our spin-coated samples were stored under ambient conditions and measured several days after preparation. Lin *et al.* [143] have shown that for larger molecular weight MEH-PPV polymers, the fluorescence yield of individual molecules decreases, and the exciton's funneling model is not fully appropriate for these bigger molecules since a large fraction of the polymer chains are the "dark" regions. They do absorb light, but they do not participate in the radiative emission. This could be one of the reasons

for the low quantum yield we find from the simultaneous measurements. Excitation power could also play a role in the quantum yield measurement, as observed in the study of organic dye nanoparticles in ref.[141]. At high excitation rate, strong interactions between singlet and triplet excitons among chromophores in a molecule can cause severe singlet-triplet quenching, singlet-singlet and triplet-triplet annihilations of excitons. As a consequence, the fluorescence and the apparent quantum yield will decrease in response to high excitation powers.

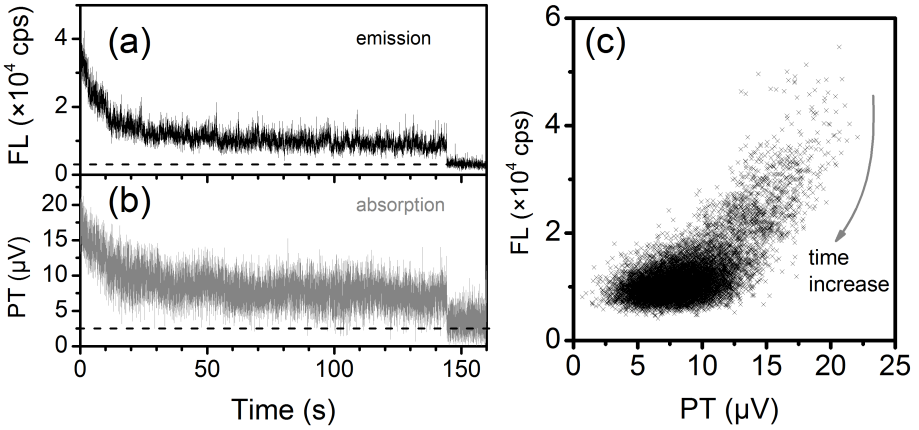

Figure 6.5: Transient traces of absorption and emission of a conjugated polymer molecule measured simultaneously. (a) fluorescence (FL) of the molecule; (b) photothermal signal (PT) of the same molecule measured simultaneously; (c) scatter plot of FL and PT showing different decay rates. The curved arrow indicates the time. The excitation power is about 3 μW, the probe power is 15 mW and the integration time is 10 ms. The pressure and temperature of the xenon cell in the measurement is about 6.3 MPa and 288 K. The black dashed lines are the background levels. At about 140s, the sharp step is because the focuses are manually shifted to a region where there are no molecules in order to record the background.

We can also have a look at the simultaneous transient traces of absorption and emission from individual polymer molecules. We did our measurements in the following sequence: first we image the polymer samples in the field of view with low excitation power (typically below 1 μW at the entrance of objective), and check single molecules by recording the transient blinking trace of fluorescence at low power. Then we go to slightly higher excitation power to record the simultaneous signals in absorption and emission while keeping the rate of photo-bleaching as low as possible. Under continuous illumination, we observed that most molecules in our current samples show continuous decrease simultaneously in both signals within a few seconds with different decay rates, as shown in Fig.6.5. The correlated continuous decays in both signals may re-

sult from the continuous bleaching of monomer absorbers. Two types of fluorescence signals have been extensively reported in many papers [122, 127, 144], and are attributed to the conformational heterogeneity of conjugated polymers in the host matrix. i) For the first type of polymer fluorescence, big polymer molecules behave like fluorescent beads. They tend to have extended conformations. There is no energy transfer or funneling between the chromophores, they absorb and emit photons independently. In this case, the time traces normally show an exponential decay of the fluorescence brightness with illumination time. ii) The second type of conjugated polymer fluorescence is attributed to collapsed conformations leading to strong intrachain interactions. Excitons created upon photon absorption by the chromophores can now migrate along the conjugated chain, and relax towards low-energy traps due to the "funneling" effect. In this second case emission mostly takes place from a few low-energy sites [121]. At high excitation power, singlet-triplet quenching, singlet to singlet and triplet to triplet annihilation are also expected to be more efficient in limiting the fluorescence [136]. The decays shown in Fig.6.5 seem to point to the first kind, with extended conformations. Yet, at this stage, we lack sufficient statistics for a reliable analysis of the decays of fluorescence and absorption. Further experiments need to be done to investigate this in more detail.

6.4. Conclusions and outlook

We measured the absorption and emission of individual conjugated MEH-PPV polymers simultaneously with an improved photothermal setup. We showed for the first time direct measurements of the absorption cross sections, the number of monomers and the apparent quantum yield of single conjugated polymer molecules. The quantum yield of the current samples is quite low and widely distributed. The conformation of conjugated polymers is closely related to their molecular weight, the polarity of the solvents used and the properties of the host matrix. Future simultaneous measurement on the absorption and emission will provide more insight into how these factors influence the optical properties of single conjugated polymer molecules.

6.5. Acknowledgments

We would like to acknowledge Dr. Yuxi Tian and Prof. Ivan Scheblykin for their efforts in making all the polymer samples used in this chapter and for helpful discussions about polymer properties. Advice from Dr. Subhasis Adhikari on polymer measurements are also kindly acknowledged. Mr Harmen van der Meer and guest Ms Tina Ding built the pressure cell used in the measurements. We gratefully acknowledge their support.

Bibliography

[1] H. Stanley. *Introduction to Phase Transitions and Critical Phenomena*. Oxford University Press, 1971.

[2] Wikipedia. Phase diagram, 2015.

[3] C. Brennen. *Cavitation and Bubble Dynamics*. Oxford University Press, New York, 1995.

[4] W. Lauterborn and T. Kurz. Physics of bubble oscillations. *Reports on Progress in Physics*, 73:106501, 2010.

[5] M. P. Brenner, S. Hilgenfeldt, and D. Lohse. Single-bubble sonoluminescence. *Reviews of Modern Physics*, 74(2):425–484, 2002.

[6] D. Lapotko. Plasmonic nanoparticle-generated photothermal bubbles and their biomedical applications. *Nanomedicine*, 4(7):813–845, 2009.

[7] Y. Wang, X. Li, Y. Zhou, P. Huang, and Y. Xu. Preparation of nanobubbles for ultrasound imaging and intracelluar drug delivery. *International Journal of Pharmaceutics*, 384(1-2):148–153, 2010.

[8] E. Boulais, R. Lachaine, A. Hatef, and M. Meunier. Plasmonics for pulsed-laser cell nanosurgery: Fundamentals and applications. *Journal of Photochemistry and Photobiology C: Photochemistry Reviews*, 17:26–49, 2013.

[9] E. Y. Lukianova-Hleb, K. M. Campbell, P. E. Constantinou, J. Braam, J. S. Olson, R. E. Ware, J. Sullivan, D. J., and D. O. Lapotko. Hemozoin-generated vapor nanobubbles for transdermal reagent- and needle-free detection of malaria. *Proceedings of the National Academy of Sciences of the United States of America*, 111(3):900–905, 2014.

[10] A. S. Goy and J. W. Fleischer. Resolution enhancement in nonlinear photoacoustic imaging. *Applied Physics Letters*, 107(21):211102, 2015.

[11] J. R. Adleman, D. A. Boyd, D. G. Goodwin, and D. Psaltis. Heterogenous catalysis mediated by plasmon heating. *Nano Letters*, 9(12):4417–4423, 2009.

[12] M. Blander and J. L. Katz. Bubble nucleation in liquids. *American Institute of Chemical Engineers Journal*, 21(5):833–848, 1975.

[13] E. Lukianova-Hleb, Y. Hu, L. Latterini, L. Tarpani, S. Lee, R. A. Drezek, J. H. Hafner, and D. O. Lapotko. Plasmonic nanobubbles as transient vapor nanobubbles generated around plasmonic nanoparticles. *ACS Nano*, 4(4):2109–2123, 2010.

[14] O. M. F. R. S. Lord Rayleigh. On the pressure developed in a liquid during the collapse of a spherical cavity. *Philosophical Magazine Series 6*, 34(200):94–98, 1917.

[15] M. S. Plesset and A. Prosperetti. Bubble dynamics and cavitation. *Annual Review of Fluid Mechanics*, 9:145–185, 1977.

[16] J. Lombard, T. Biben, and S. Merabia. Kinetics of nanobubble generation around overheated nanoparticles. *Physical Review Letters*, 112(10):105701, 2014.

[17] M. Minnaert. On musical air-bubbles and the sounds of running water. *The London, Edinburgh, and Dublin Philosophical Magazine and Journal of Science*, 16(104):235–248, 1933.

[18] L. Stricker, B. Dollet, D. Fernández Rivas, and D. Lohse. Interacting bubble clouds and their sonochemical production. *The Journal of the Acoustical Society of America*, 134(3):1854–1862, 2013.

[19] F. Gilmore. The growth or collapse of a spherical bubble in a viscous compressible liquid. Report, Hydrodynamics Laboratory, California Institute of Technology, 1952.

[20] K. de Graaf, I. Penesis, and P. Brandner. Comparison of the Rayleigh-Plesset and Gilmore equations and additional aspects for the modelling of seismic airgun bubble dynamics. In *18th Australasian Fluid Mechanics Conference*. Leishman Associates, 2012.

[21] G. Ahlers, S. Grossmann, and D. Lohse. Heat transfer and large scale dynamics in turbulent Rayleigh-Bénard convection. *Reviews of Modern Physics*, 81(2):503–537, 2009.

[22] D. Lohse and X. Zhang. Surface nanobubbles and nanodroplets. *Reviews of Modern Physics*, 87(3):981–1035, 2015.

[23] G. Nagayama, T. Tsuruta, and P. Cheng. Molecular dynamics simulation on bubble formation in a nanochannel. *International Journal of Heat and Mass Transfer*, 49(23-24):4437–4443, 2006.

[24] M. de Saint Victor, C. Crake, C. C. Coussios, and E. Stride. Properties, characteristics and applications of microbubbles for sonothrombolysis. *Expert Opinion on Drug Delivery*, 11(2):187–209, 2014.

[25] E. Y. Lukianova-Hleb and D. O. Lapotko. Experimental techniques for imaging and measuring transient vapor nanobubbles. *Applied Physics Letters*, 101(26):264102, 2012.

[26] V. Kotaidis, C. Dahmen, G. von Plessen, F. Springer, and A. Plech. Excitation of nanoscale vapor bubbles at the surface of gold nanoparticles in water. *The Journal of Chemical Physics*, 124(18):184702, 2006.

[27] B. H. T. Goh, Y. D. A. Oh, E. Klaseboer, S. W. Ohl, and B. C. Khoo. A low-voltage spark-discharge method for generation of consistent oscillating bubbles. *Review of Scientific Instruments*, 84(1):014705, 2013.

[28] G. Nagashima, E. V. Levine, D. P. Hoogerheide, M. M. Burns, and J. A. Golovchenko. Superheating and homogeneous single bubble nucleation in a solid-state nanopore. *Physical Review Letters*, 113(2):024506, 2014.

[29] R. Lachaine, E. Boulais, and M. Meunier. From thermo- to plasma-mediated ultrafast laser-induced plasmonic nanobubbles. *ACS Photonics*, 1(4):331–336, 2014.

[30] L. Hou, M. Yorulmaz, N. R. Verhart, and M. Orrit. Explosive formation and dynamics of vapor nanobubbles around a continuously heated gold nanosphere. *New Journal of Physics*, 17(1):013050, 2015.

[31] E. Y. Lukianova-Hleb and D. O. Lapotko. Influence of transient environmental photothermal effects on optical scattering by gold nanoparticles. *Nano Letters*, 9(5):2160–2166, 2009.

[32] A. Siems, S. A. L. Weber, J. Boneberg, and A. Plech. Thermodynamics of nanosecond nanobubble formation at laser-excited metal nanoparticles. *New Journal of Physics*, 13:043018, 2011.

[33] E. V. Shashkov, M. Everts, E. I. Galanzha, and V. P. Zharov. Quantum dots as multimodal photoacoustic and photothermal contrast agents. *Nano Letters*, 8(11):3953–3958, 2008.

[34] M. T. Carlson, A. J. Green, and H. H. Richardson. Superheating water by CW excitation of gold nanodots. *Nano Letters*, 12(3):1534–1537, 2012.

[35] O. Neumann, A. S. Urban, J. Day, S. Lal, P. Nordlander, and N. J. Halas. Solar vapor generation enabled by nanoparticles. *ACS Nano*, 7(1):42–49, 2012.

[36] J. P. Padilla-Martinez, C. Berrospe-Rodriguez, G. Aguilar, J. C. Ramirez-San-Juan, and R. Ramos-Garcia. Optic cavitation with CW lasers: A review. *Physics of Fluids*, 26(12):122007, 2014.

[37] G. Baffou and H. Rigneault. Femtosecond-pulsed optical heating of gold nanoparticles. *Physical Review B*, 84(3):035415, 2011.

[38] C. U. Chan and C.-D. Ohl. Total-internal-reflection-fluorescence microscopy for the study of nanobubble dynamics. *Physical Review Letters*, 109(17):174501, 2012.

[39] Z. Fang, Y.-R. Zhen, O. Neumann, A. Polman, F. Javier Garcia de Abajo, P. Nordlander, and N. J. Halas. Evolution of light-induced vapor generation at a liquid-immersed metallic nanoparticle. *Nano Letters*, 13(4):1736–1742, 2013.

[40] E. S. Bialkowski. *Photothermal Spectroscopy Methods for Chemical Analysis*, volume 134. John Wiley and Sons, Inc, 1996.

[41] M. Selmke, M. Braun, and F. Cichos. Photothermal single-particle microscopy: Detection of a nanolens. *ACS Nano*, 6(3):2741–2749, 2012.

[42] A. Gaiduk, P. V. Ruijgrok, M. Yorulmaz, and M. Orrit. Detection limits in photothermal microscopy. *Chemical Science*, 1(3):343–350, 2010.

[43] S. Berciaud, L. Cognet, G. A. Blab, and B. Lounis. Photothermal heterodyne imaging of individual nonfluorescent nanoclusters and nanocrystals. *Physical Review Letters*, 93(25):257402, 2004.

[44] D. Boyer, P. Tamarat, A. Maali, B. Lounis, and M. Orrit. Photothermal imaging of nanometer-sized metal particles among scatterers. *Science*, 297(5584):1160–1163, 2002.

[45] A. Gaiduk, M. Yorulmaz, P. V. Ruijgrok, and M. Orrit. Room-temperature detection of a single molecule's absorption by photothermal contrast. *Science*, 330(6002):353–356, 2010.

[46] A. Arbouet, C. Voisin, D. Christofilos, P. Langot, N. D. Fatti, F. Vallée, J. Lermé, G. Celep, E. Cottancin, M. Gaudry, M. Pellarin, M. Broyer, M. Maillard, M. P. Pileni, and M. Treguer. Electron-phonon scattering in metal clusters. *Physical Review Letters*, 90(17):177401, 2003.

[47] K. Lindfors, T. Kalkbrenner, P. Stoller, and V. Sandoghdar. Detection and spectroscopy of gold nanoparticles using supercontinuum white light confocal microscopy. *Physical Review Letters*, 93(3):037401, 2004.

[48] M. A. v. Dijk. *Nonlinear optical studies of single gold nanoparticles*. Thesis, Leiden University, 2007.

[49] S. Berciaud, D. Lasne, G. A. Blab, L. Cognet, and B. Lounis. Photothermal heterodyne imaging of individual metallic nanoparticles: Theory versus experiment. *Physical Review B*, 73(4):045424, 2006.

[50] F. V. Ignatovich and L. Novotny. Real-time and background-free detection of nanoscale particles. *Physical Review Letters*, 96(1):013901, 2006.

[51] M. A. van Dijk, M. Lippitz, D. Stolwijk, and M. Orrit. A common-path interferometer for time-resolved and shot-noise-limited detection of single nanoparticles. *Optics Express*, 15(5):2273–2287, 2007.

[52] B. Simons. Phase transitions and collective phenomena, 2011. Lecture notes. http://www.tcm.phy.cam.ac.uk/ bds10/phase.html.

[53] Wikipedia. Supercritical fluid, 2016.

[54] E. C. Dreaden, A. M. Alkilany, X. Huang, C. J. Murphy, and M. A. El-Sayed. The golden age: gold nanoparticles for biomedicine. *Chemical Society Reviews*, 41(7):2740–2779, 2012.

[55] A. O. Govorov and H. H. Richardson. Generating heat with metal nanoparticles. *Nano Today*, 2(1):30–38, 2007.

[56] G. Lu, L. Hou, T. Zhang, J. Liu, H. Shen, C. Luo, and Q. Gong. Plasmonic sensing via photoluminescence of individual gold nanorod. *The Journal of Physical Chemistry C*, 116(48):25509–25516, 2012.

[57] Q. Wang, G. Lu, L. Hou, T. Zhang, C. Luo, H. Yang, G. Barbillon, F. H. Lei, C. A. Marquette, P. Perriat, O. Tillement, S. Roux, Q. Ouyang, and Q. Gong. Fluorescence correlation spectroscopy near individual gold nanoparticle. *Chemical Physics Letters*, 503(4-6):256–261, 2011.

[58] P. Zijlstra, P. M. R. Paulo, and M. Orrit. Optical detection of single non-absorbing molecules using the surface plasmon resonance of a gold nanorod. *Nature Nanotechnology*, 7(6):379–382, 2012.

[59] H. Yuan, S. Khatua, P. Zijlstra, M. Yorulmaz, and M. Orrit. Thousand-fold enhancement of single-molecule fluorescence near a single gold nanorod. *Angewandte Chemie International Edition*, 52(4):1217–1221, 2013.

[60] J. H. Burroughes, D. D. C. Bradley, A. R. Brown, R. N. Marks, K. Mackay, R. H. Friend, P. L. Burns, and A. B. Holmes. Light-emitting diodes based on conjugated polymers. *Nature*, 347(6293):539–541, 1990.

[61] S. Günes, H. Neugebauer, and N. S. Sariciftci. Conjugated polymer-based organic solar cells. *Chemical Reviews*, 107(4):1324–1338, 2007.

[62] M. Vacha and S. Habuchi. Conformation and physics of polymer chains: a single-molecule perspective. *NPG Asia Materials*, 2:134–142, 2010.

[63] D. Hu, J. Yu, and P. F. Barbara. Single-molecule spectroscopy of the conjugated polymer MEH-PPV. *Journal of the American Chemical Society*, 121(29):6936–6937, 1999.

[64] P. Debenedetti. *Metastable Liquids: Concepts and Principles*. Princeton University Press, 1996.

[65] P. J. Linstrom and W. G. Mallard. National Institute of Standards and Technology (NIST) Chemistry WebBook, NIST Standard Reference Database Number 69, 2011. http://webbook.nist.gov/chemistry/.

[66] S. Merabia, P. Keblinski, L. Joly, L. Lewis, and J.-L. Barrat. Critical heat flux around strongly heated nanoparticles. *Physical Review E*, 79(2):021404, 2009.

[67] H. Carslaw and J. Jaeger. *Conduction of Heat in Solids*. Clarendon Press, 1986.

[68] Wikipedia. Knudsen number, 2016.

[69] K. Yang, Y. Zhou, Q. Ren, J. Y. Ye, and C. X. Deng. Dynamics of microbubble generation and trapping by self-focused femtosecond laser pulses. *Applied Physics Letters*, 95(5):051107, 2009.

[70] A. Vogel, N. Linz, and S. Freidank. Femtosecond-laser-induced nanocavitation in water: implications for optical breakdown threshold and cell surgery. *Physical Review Letters*, 100(3):038102, 2008.

[71] V. Kotaidis and A. Plech. Cavitation dynamics on the nanoscale. *Applied Physics Letters*, 87(21):213102, 2005.

[72] V. Zharov and D. Lapotko. Photothermal sensing of nanoscale targets. *Review of Scientific Instruments*, 74(1):785–788, 2003.

[73] E. Boulais, R. Lachaine, and M. Meunier. Plasma mediated off-resonance plasmonic enhanced ultrafast laser-induced nanocavitation. *Nano Letters*, 12(9):4763–4769, 2012.

[74] T. Katayama, K. Setoura, D. Werner, H. Miyasaka, and S. Hashimoto. Picosecond-to-nanosecond dynamics of plasmonic nanobubbles from pump-probe spectral measurements of aqueous colloidal gold nanoparticles. *Langmuir*, 30(31):9504–9513, 2014.

[75] G. Baffou, J. Polleux, H. Rigneault, and S. Monneret. Super-heating and micro-bubble generation around plasmonic nanoparticles under cw illumination. *The Journal of Physical Chemistry C*, 118(9):4890–4898, 2014.

[76] A. Heber, M. Selmke, and F. Cichos. Metal nanoparticle based all-optical photothermal light modulator. *ACS Nano*, 8(2):1893–1898, 2014.

[77] X. Zhang, D. Y. C. Chan, D. Wang, and N. Maeda. Stability of interfacial nanobubbles. *Langmuir*, 29(4):1017–1023, 2012.

[78] X. Zhang, H. Lhuissier, C. Sun, and D. Lohse. Surface nanobubbles nucleate microdroplets. *Physical Review Letters*, 112(14):144503, 2014.

[79] E. Y. Lukianova-Hleb, X. Ren, R. R. Sawant, X. Wu, V. P. Torchilin, and D. O. Lapotko. On-demand intracellular amplification of chemoradiation with cancer-specific plasmonic nanobubbles. *Nature Medicine*, 20(7):778–784, 2014.

[80] J. Yao, L. Wang, C. Li, C. Zhang, and L. V. Wang. Photoimprint photoacoustic microscopy for three-dimensional label-free subdiffraction imaging. *Physical Review Letters*, 112(1):014302, 2014.

[81] A. Gaiduk, M. Yorulmaz, and M. Orrit. Correlated absorption and photoluminescence of single gold nanoparticles. *ChemPhysChem*, 12(8):1536–1541, 2011.

[82] P. Zijlstra and M. Orrit. Single metal nanoparticles: optical detection, spectroscopy and applications. *Reports on Progress in Physics*, 74(10):106401, 2011.

[83] P. V. Ruijgrok, N. R. Verhart, P. Zijlstra, A. L. Tchebotareva, and M. Orrit. Brownian fluctuations and heating of an optically aligned gold nanorod. *Physical Review Letters*, 107(3):037401, 2011.

[84] I. U. Vakarelski, N. A. Patankar, J. O. Marston, D. Y. C. Chan, and S. T. Thoroddsen. Stabilization of Leidenfrost vapour layer by textured superhydrophobic surfaces. *Nature*, 489(7415):274–277, 2012.

[85] B. Gompf and R. Pecha. Mie scattering from a sonoluminescing bubble with high spatial and temporal resolution. *Physical Review E*, 61(5):5253–5256, 2000.

[86] R. G. Holt, D. F. Gaitan, A. A. Atchley, and J. Holzfuss. Chaotic sonoluminescence. *Physical Review Letters*, 72(9):1376–1379, 1994.

[87] D. Lide. *CRC Handbook of Chemistry and Physics (Internet Version 2005)*. CRC Press, Boca Raton, FL, 2005.

[88] The triisopropylbenzene is the main component of oil, sound velocities in some related compounds is about 1350 m/s, data from a commercial website (https://www.flexim.com).

[89] E. Y. Lukianova-Hleb, Y.-S. Kim, I. Belatsarkouski, A. M. Gillenwater, B. E. O'Neill, and D. O. Lapotko. Intraoperative diagnostics and elimination of residual microtumours with plasmonic nanobubbles. *Nature Nanotechnology*, advance online publication, 2016.

[90] D. A. Boyd, L. Greengard, M. Brongersma, M. Y. El-Naggar, and D. G. Goodwin. Plasmon-assisted chemical vapor deposition. *Nano Letters*, 6(11):2592–2597, 2006.

[91] H. H. Richardson, M. T. Carlson, P. J. Tandler, P. Hernandez, and A. O. Govorov. Experimental and theoretical studies of light-to-heat conversion and collective heating effects in metal nanoparticle solutions. *Nano Letters*, 9(3):1139–1146, 2009.

[92] S. Hashimoto, D. Werner, and T. Uwada. Studies on the interaction of pulsed lasers with plasmonic gold nanoparticles toward light manipulation, heat management, and nanofabrication. *Journal of Photochemistry and Photobiology C: Photochemistry Reviews*, 13(1):28–54, 2012.

[93] D. Lapotko. Optical excitation and detection of vapor bubbles around plasmonic nanoparticles. *Optics Express*, 17(4):2538–2556, 2009.

[94] A. Plech, V. Kotaidis, M. Lorenc, and M. Wulff. Thermal dynamics in laser excited metal nanoparticles. *Chemical Physics Letters*, 401(4-6):565–569, 2005.

[95] P. V. Ruijgrok, P. Zijlstra, A. L. Tchebotareva, and M. Orrit. Damping of acoustic vibrations of single gold nanoparticles optically trapped in water. *Nano Letters*, 12(2):1063–9, 2012.

[96] D. Werner and S. Hashimoto. Improved working model for interpreting the excitation wavelength- and fluence-dependent response in pulsed laser-induced size reduction of aqueous gold nanoparticles. *The Journal of Physical Chemistry C*, 115(12):5063–5072, 2011.

[97] Z. Lin, L. V. Zhigilei, and V. Celli. Electron-phonon coupling and electron heat capacity of metals under conditions of strong electron-phonon nonequilibrium. *Physical Review B*, 77(7):075133, 2008.

[98] M. Strasser, K. Setoura, U. Langbein, and S. Hashimoto. Computational modeling of pulsed laser-induced heating and evaporation of gold nanoparticles. *The Journal of Physical Chemistry C*, 118(44):25748–25755, 2014.

[99] A. Plech, V. Kotaidis, S. Grésillon, C. Dahmen, and G. von Plessen. Laser-induced heating and melting of gold nanoparticles studied by time-resolved X-ray scattering. *Physical Review B*, 70(19):195423, 2004.

[100] H. Lamb. On the vibrations of an elastic sphere. *Proceedings of the London Mathematical Society*, s1-13(1):189–212, 1881.

[101] C. Voisin, D. Christofilos, N. Del Fatti, and F. Vallée. Environment effect on the acoustic vibration of metal nanoparticles. *Physica B: Condensed Matter*, 316-317:89–94, 2002.

[102] K. Yu, P. Zijlstra, J. E. Sader, Q.-H. Xu, and M. Orrit. Damping of acoustic vibrations of immobilized single gold nanorods in different environments. *Nano Letters*, 13(6):2710–2716, 2013.

[103] V. Juvé, M. Scardamaglia, P. Maioli, A. Crut, S. Merabia, L. Joly, N. Del Fatti, and F. Vallée. Cooling dynamics and thermal interface resistance of glass-embedded metal nanoparticles. *Physical Review B*, 80(19):195406, 2009.

[104] O. M. Wilson, X. Hu, D. G. Cahill, and P. V. Braun. Colloidal metal particles as probes of nanoscale thermal transport in fluids. *Physical Review B*, 66(22):224301, 2002.

[105] M. Hu and G. V. Hartland. Heat dissipation for Au particles in aqueous solution: Relaxation time versus size. *The Journal of Physical Chemistry B*, 106(28):7029–7033, 2002.

[106] F. Cooper. Heat transfer from a sphere to an infinite medium. *International Journal of Heat and Mass Transfer*, 20(9):991–993, 1977.

[107] M. Hu, H. Petrova, and G. V. Hartland. Investigation of the properties of gold nanoparticles in aqueous solution at extremely high lattice temperatures. *Chemical Physics Letters*, 391(4-6):220–225, 2004.

[108] K. Setoura, D. Werner, and S. Hashimoto. Optical scattering spectral thermometry and refractometry of a single gold nanoparticle under CW laser excitation. *The Journal of Physical Chemistry C*, 116(29):15458–15466, 2012.

[109] S. Berciaud, L. Cognet, and B. Lounis. Photothermal absorption spectroscopy of individual semiconductor nanocrystals. *Nano Letters*, 5(11):2160–2163, 2005.

[110] S. Berciaud, L. Cognet, P. Poulin, R. B. Weisman, and B. Lounis. Absorption spectroscopy of individual single-walled carbon nanotubes. *Nano Letters*, 7(5):1203–1207, 2007.

[111] S. Li, L. Guo, C. Liu, and Y. Zhang. Application of supercritical fluid extraction coupled with counter-current chromatography for extraction and online isolation of unstable chemical components from rosa damascena. *Journal of Separation Science*, 36(13):2104–2113, 2013.

[112] P. M. Rentzepis and D. C. Douglass. Xenon as a solvent. *Nature*, 293(5828):165–166, 1981.

[113] D. H. Garside, H. V. Molgaard, and B. L. Smith. Refractive index and Lorentz-Lorenz function of xenon liquid and vapour. *Journal of Physics B: Atomic and Molecular Physics*, 1(3):449, 1968.

[114] R. A. Leach and J. M. Harris. Supercritical fluids as spectroscopic solvents for thermooptical absorption measurements. *Analytical Chemistry*, 56(8):1481–1487, 1984.

[115] L. Pagliaro, F. Reitz, and J. Wang. An optical pressure chamber designed for high numerical aperture studies on adherent living cells. *The Undersea and Hyperbaric Medicine*, 22(2):171–181, 1995.

[116] S. Timoshenko and S. Woinowsky-Krieger. *Theory of Plates and Shells*. McGraw-Hill College; 2 edition, New York, 1987.

[117] M. E. Briggs and R. W. Gammon. Photothermal deflection in a supercritical fluid. *International Journal of Thermophysics*, 16(6):1439–1453, 1995.

[118] D. L. Huber. Critical slowing down in an anisotropic ferromagnet. *Physics Letters A*, 28(9):644–645, 1969.

[119] D. Hu, J. Yu, K. Wong, B. Bagchi, P. J. Rossky, and P. F. Barbara. Collapse of stiff conjugated polymers with chemical defects into ordered, cylindrical conformations. *Nature*, 405(6790):1030–1033, 2000.

[120] M. Orrit and J. Bernard. Single pentacene molecules detected by fluorescence excitation in a *p* -terphenyl crystal. *Physical Review Letters*, 65(21):2716–2719, 1990.

[121] D. A. V. Bout, W.-T. Yip, D. Hu, D.-K. Fu, T. M. Swager, and P. F. Barbara. Discrete intensity jumps and intramolecular electronic energy transfer in the spectroscopy of single conjugated polymer molecules. *Science*, 277(5329):1074–1077, 1997.

[122] T. Huser, M. Yan, and L. J. Rothberg. Single chain spectroscopy of conformational dependence of conjugated polymer photophysics. *Proceedings of the National Academy of Sciences of the United States of America*, 97(21):11187–11191, 2000.

[123] K. Becker and J. M. Lupton. Efficient light harvesting in dye-endcapped conjugated polymers probed by single molecule spectroscopy. *Journal of the American Chemical Society*, 128(19):6468–6479, 2006.

[124] F. Schindler, J. M. Lupton, J. Feldmann, and U. Scherf. A universal picture of chromophores in pi-conjugated polymers derived from single-molecule spectroscopy. *Proceedings of the National Academy of Sciences of the United States of America*, 101(41):14695–14700, 2004.

[125] J. K. Grey, D. Y. Kim, B. C. Norris, W. L. Miller, and P. F. Barbara. Size-dependent spectroscopic properties of conjugated polymer nanoparticles. *The Journal of Physical Chemistry B*, 110(51):25568–25572, 2006.

[126] Y. J. Lee, D. Y. Kim, and P. F. Barbara. Effect of sample preparation and excitation conditions on the single molecule spectroscopy of conjugated polymers. *The Journal of Physical Chemistry B*, 110(20):9739–9742, 2006.

[127] Y. Ebihara and M. Vacha. Relating conformation and photophysics in single MEH-PPV chains. *The Journal of Physical Chemistry B*, 112(40):12575–12578, 2008.

[128] H. Kobayashi, S. Onda, S. Furumaki, S. Habuchi, and M. Vacha. A single-molecule approach to conformation and photophysics of conjugated polymers. *Chemical Physics Letters*, 528:1–6, 2012.

[129] J. Yu, D. Hu, and P. F. Barbara. Unmasking electronic energy transfer of conjugated polymers by suppression of O_2 quenching. *Science*, 289(5483):1327–1330, 2000.

[130] J.-J. Liang, J. D. White, Y. C. Chen, C. F. Wang, J. C. Hsiang, T. S. Lim, W. Y. Sun, J. H. Hsu, C. P. Hsu, M. Hayashi, W. S. Fann, K. Y. Peng, and S. A. Chen. Heterogeneous energy landscapes of individual luminescent conjugated polymers. *Physical Review B*, 74(8):085209, 2006.

[131] J. G. Müller, U. Lemmer, G. Raschke, M. Anni, U. Scherf, J. M. Lupton, and J. Feldmann. Linewidth-limited energy transfer in single conjugated polymer molecules. *Physical Review Letters*, 91(26):267403, 2003.

[132] H. Lin, S. R. Tabaei, D. Thomsson, O. Mirzov, P.-O. Larsson, and I. G. Scheblykin. Fluorescence blinking, exciton dynamics, and energy transfer domains in single conjugated polymer chains. *Journal of the American Chemical Society*, 130(22):7042–7051, 2008.

[133] T.-Q. Nguyen, V. Doan, and B. J. Schwartz. Conjugated polymer aggregates in solution: Control of interchain interactions. *The Journal of Chemical Physics*, 110(8):4068–4078, 1999.

[134] S. Onda, H. Kobayashi, T. Hatano, S. Furumaki, S. Habuchi, and M. Vacha. Complete suppression of blinking and reduced photobleaching in single MEH-PPV chains in solution. *The Journal of Physical Chemistry Letters*, 2(21):2827–2831, 2011.

[135] D. Wang, Y. Yuan, Y. Mardiyati, C. Bubeck, and K. Koynov. From single chains to aggregates, how conjugated polymers behave in dilute solutions. *Macromolecules*, 46(15):6217–6224, 2013.

[136] J. Yu, R. Lammi, A. J. Gesquiere, and P. F. Barbara. Singlet-triplet and triplet-triplet interactions in conjugated polymer single molecules. *The Journal of Physical Chemistry B*, 109(20):10025–10034, 2005.

[137] Y. Ebihara and M. Vacha. A method for determining the absorption ellipsoid of single conjugated polymer molecules and single luminescent nanoparticles. *The Journal of Chemical Physics*, 123(24):244710, 2005.

[138] K.-i. Shinohara, T. Kitami, and K. Nakamae. Direct measurement of structural diversity in single molecules of a chiral helical π-conjugated polymer. *Journal of Polymer Science Part A: Polymer Chemistry*, 42(16):3930–3935, 2004.

[139] Y. Tian, M. V. Kuzimenkova, J. Halle, M. Wojdyr, A. Diaz de Zerio Mendaza, P.-O. Larsson, C. Müller, and I. G. Scheblykin. Molecular weight determination by counting molecules. *The Journal of Physical Chemistry Letters*, 6(6):923–927, 2015.

[140] O. Mirzov and I. G. Scheblykin. Photoluminescence spectra of a conjugated polymer: from films and solutions to single molecules. *Physical Chemistry Chemical Physics*, 8(47):5569–5576, 2006.

[141] A. Gaiduk, M. Yorulmaz, E. Ishow, and M. Orrit. Absorption, luminescence, and sizing of organic dye nanoparticles and of patterns formed upon dewetting. *ChemPhysChem*, 13(4):946–951, 2012.

[142] N. C. Greenham, I. D. W. Samuel, G. R. Hayes, R. T. Phillips, Y. A. R. R. Kessener, S. C. Moratti, A. B. Holmes, and R. H. Friend. Measurement of absolute photoluminescence quantum efficiencies in conjugated polymers. *Chemical Physics Letters*, 241(1-2):89–96, 1995.

[143] H. Lin, Y. Tian, K. Zapadka, G. Persson, D. Thomsson, O. Mirzov, P.-O. Larsson, J. Widengren, and I. G. Scheblykin. Fate of excitations in conjugated polymers: Single-molecule spectroscopy reveals nonemissive "dark" regions in MEH-PPV individual chains. *Nano Letters*, 9(12):4456–4461, 2009.

[144] E. N. Hooley, A. J. Tilley, J. M. White, K. P. Ghiggino, and T. D. M. Bell. Energy transfer in PPV-based conjugated polymers: a defocused widefield fluorescence microscopy study. *Physical Chemistry Chemical Physics*, 16(15):7108–7114, 2014.

Appendices

A

Thermodynamic and optical data of some common substances

Table A.1: Thermodynamic and optical data of some common substances at ambient temperature and pressure*

Substance	n	$10^4 \times \frac{\partial n}{\partial T}$ (K^{-1})	ρ ($g \cdot cm^{-3}$)	κ ($Wm^{-1}K^{-1}$)	$10^{-3} \times C_p$ ($Jkg^{-1}K^{-1}$)	$10^3 \times \gamma$ ($N \cdot m^{-1}$)	$10^3 \times \mu$ ($Pa \cdot s$)	$T_b(T_m)$ (C°)	v_l ($m \cdot s^{-1}$)	v_s ($m \cdot s^{-1}$)
water(25 $C°$)	1.33	-0.91	0.997	0.61	4.18	71.99	0.89	100	1497	-
glycerol	1.47	-2.7	1.261	0.28	2.4	63	1495	290	1904	-
n-pentane	1.36	-5.5	0.626	0.11	2.31	15.49	0.22	36.1	1008	-
methanol	1.31	-3.94	0.792	0.202	2.46	22.07	0.59	64.6	1121	-
ethanol	1.36	-3.7	0.789	0.167	2.36	21.97	1.203	78.2	1162	-
toluene	1.50	-5.68	0.87	0.135	1.69	27.73	0.56	110.6	1304	-
acetone	1.36	-5.42	0.8	0.19	2.18	22.72	0.295	56	1203	-
BK7 glass	1.52	-0.13	2.51	1.114	0.86	-	-	557	5100	2840
SiO_2	1.46	-0.12	2.2	1.38	0.703	-	-	1600	5968	3764
gold	0.27+2.95i	unknown	19.3	318	0.129	-	-	1064	3240	1200
PMMA	1.49	-1.2	1.19	0.17-0.19	1.4-1.5	-	-	160	unknown	unknown
air	1	-0.01	0.001	0.026	1.01	-	0.018	-	346	-
water steam (100 $C°$)	1	unknown	0.001	0.025	2.08	-	0.012	-	472	-

(*The tabulated constants for each material are the refractive index n at 589.3 nm, the derivative of refractive index with respect to temperature $\frac{\partial n}{\partial T}$, the density ρ, the thermal conductivity κ, the heat capacity C_p, the surface tension (of liquid) γ, the viscosity μ, the boiling point T_b for liquids, the melting point T_m for solids, the velocity of longitudinal sound waves v_l, and the velocity of shear waves v_s. The data are from the CRC Handbook of Chemistry and Physics (90^{th}), National Institute of Standards and Technology (NIST), and Photothermal Spectroscopy Methods for Chemical Analysis [40]. The "unknown" means the data are not found in the above resources.)

B

Scheme of the pressure system

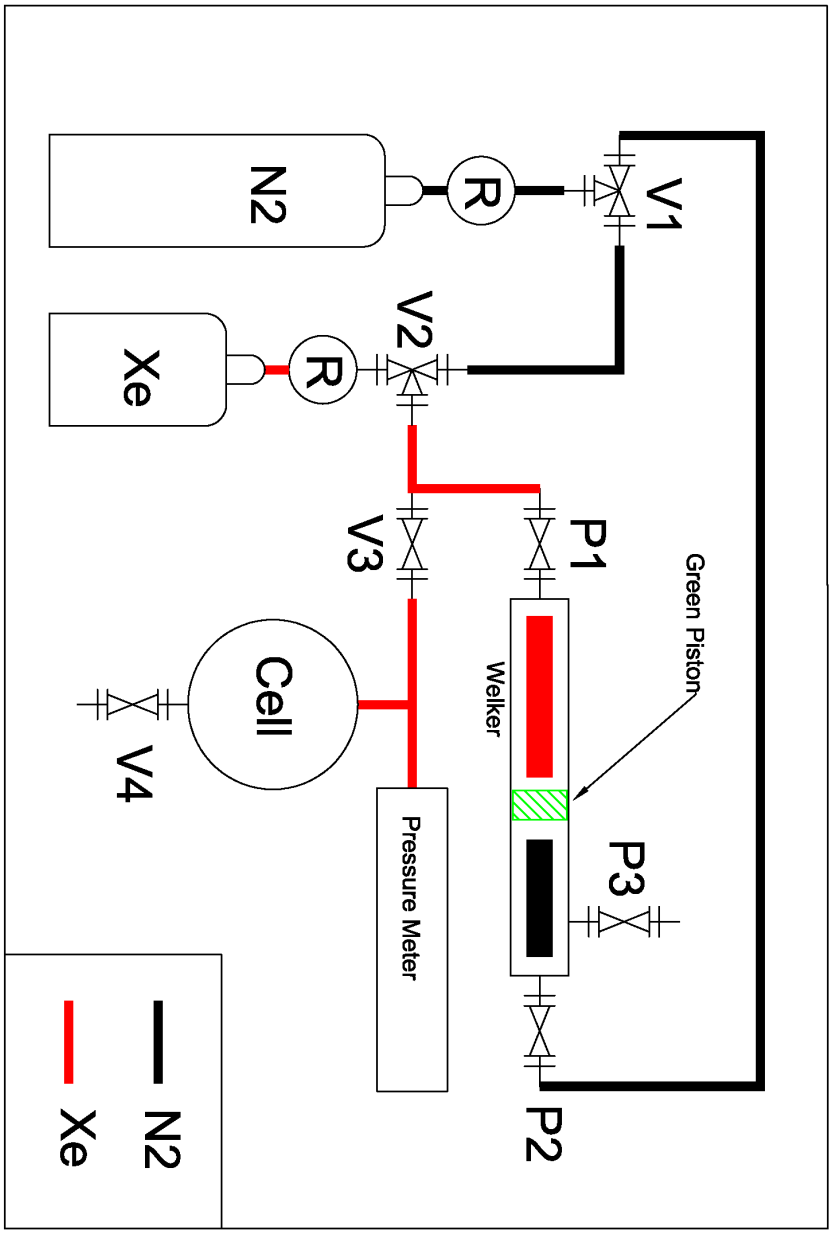

Figure B.1: Scheme of the pressure system used for the measurements in near-critical xenon. V1, V2, V3 and V4 are the gas valves; P1, P2 and P3 are the valves on the compression cylinder. Pressure chamber is labeled as "Cell"; "R" is the pressure regulator.

C

Comparison of calculated boiling temperature with experiments

We compare the theoretical value of the critical powers for the boiling as found in Fig.2.3 in Chapter 2 to the experimental critical powers found in Fig.3.2 of Chapter 3 and in Chapter 4. In Chapter 3, we find that the critical absorbed power for a particle with 40 nm radius (80 nm diameter) in water is 62.1 μW from Fig.2.3. This is calculated for a particle in water, but in our experiments we have particles in water on a silica substrate. To correct for this we use the average value of the thermal conductivity of water (0.65 $\mathrm{Wm^{-1}K^{-1}}$) and silica (1.38 $\mathrm{Wm^{-1}K^{-1}}$). Then we find:

$$P_{abs.}^{crit.} = \frac{\frac{1}{2}(0.65+1.38)}{0.65} \times 62.1(\mu W) = 97(\mu W) \tag{C.1}$$

Based on the diffraction-limited microscope's point spread function we estimate the size/diameter of the focus of the heating beam to be:

$$d = 1.22 \times \frac{\lambda}{N.A.} = 1.22 \times \frac{532}{1.45}(nm) = 448(nm) \tag{C.2}$$

Taking the refractive index of the medium surrounding a gold nanosphere to be the average of the refractive index of water and glass, we can use Mie theory to estimate the absorption cross section of the particle. We find $\sigma_{abs} = 1.7 \times 10^4$ $\mathrm{nm^2}$ at 532 nm. We can now relate the critical absorbed power for the formation of a nanobubble to the critical power *in the focus:*

$$P_{crit.}^{focus}\Big|_{80nm} = \left(\frac{A_{focus}}{\sigma_{abs}}\right) \times P_{abs.}^{crit.} = \left[\frac{\pi(448/2)^2}{1.7\times10^4}\right] \times 97(\mu W) = 0.9(mW) \tag{C.3}$$

This should be compared to critical powers measured in experiments, which depended on the conditions. For water on a BK7 glass substrate (Fig.3.6 in Chapter 3), the critical power was about 1.0 mW, in good agreement with the above estimate. On a fused silica substrate, because of the aberrations introduced by the poor index matching with the objective, the critical power rose to about 3 mW (see Fig.3.2, where the power is not corrected for objective transmission). A similar reduction of local intensity was found by Ruijgrok et al. [83] in the calculated and measured values of the intensity at the focus of a high numerical-aperture objective and attributed to spherical aberrations. For pentane on BK7 glass, the critical power was much lower, about 100 μW (Fig.3.5 in Chapter 3, insert).

In Chapter 4, we use a 50 nm diameter gold sphere in water and BK7 glass substrate. The critical absorbed power for the boiling in water around a 50 nm gold sphere is about 42.3 μW from Fig.2.3 in Chapter 2. If we consider the substrate, the critical absorbed power becomes:

$$P_{abs.}^{crit.}\Big|_{50nm} = \frac{\frac{1}{2}(0.65+1.11)}{0.65} \times 42.3(\mu W) = 57.3(\mu W) \tag{C.4}$$

The N.A. of the objective used in Chapter 4 is 1.4, so the diffraction-limited diameter of the focus of the CW heating beam (532 nm) is:

$$d = 1.22 \times \frac{\lambda}{N.A.} = 1.22 \times \frac{532}{1.4}(nm) = 464(nm) \tag{C.5}$$

The absorption cross section of a 50 nm diameter gold sphere on a BK7 substrate in water, taking into account the BK7 substrate, is calculated to be about 7650 nm^2 at 532 nm. Using the same equation as Eq.C.3, we find the critical power *in the focus* for the formation of a vapor nanobubble around a 50 nm gold sphere:

$$P_{crit.}^{focus}\Big|_{50nm} = \left(\frac{A_{focus}}{\sigma_{abs}}\right) \times P_{abs.}^{crit.}\Big|_{50nm} = \left[\frac{\pi(464/2)^2}{7646}\right] \times 57.3(\mu W) = 1.3(mW) \tag{C.6}$$

The critical power found in such calculations is close to, but a bit higher than the CW heating power found in our pump-probe experiments when the vapor bubble forms. Note that in the pump-probe experiments, both the pump and probe pulses contribute to the temperature rise of gold nanoparticle. More importantly, the acoustic vibration of the gold nanoparticle can behave as a trigger to tear the hot liquid molecules apart and initiate a vapor bubble.

D

Energies involved in the vapor bubble growth

To understand bubble growth and instability better, we have estimated the main energy contributions involved in the explosion. Although this process appears to follow an inertial regime, we neglected kinetic energy, which can be considered in a future dynamic model. The three main contributions mentioned in the main text of Chapter 3 were calculated as follows, assuming the non-evaporated overheated liquid is pushed mechanically by the created vapor, without heat conduction through the interfaces:

i) Surface energy: it is calculated for varying bubble radius from the surface tension which is temperature dependent. The temperature is assumed to be the equilibrium one, although this is certainly not true during the expansion.

ii) Latent heat and heat capacity: this energy is calculated from the internal energy of liquid and gas, as a function of bubble diameter.

iii) Overheated liquid thermal energy: this is the heat stored in the overheated layer, integrating all layers of liquid whose temperature exceeds the equilibrium curve between regimes I and II (dashed line in Figure D.1). The temperature profiles of the liquid immediately before the explosion (blue solid curve) and for two different bubble diameters (red curves) are presented in Fig.D.1. Liquid layers with temperature above the dashed curve are in principle able to give energy to the vapor shell and to feed the expansion.

The three energy contributions above are plotted as functions of the bubble radius in Fig.D.2. Only half of the overheated liquid energy has been used to heat the bubble, the other half was assumed to dissipate into the colder outer layers. The net energy contribution, plotted in Fig.D.3 against bubble radius, is

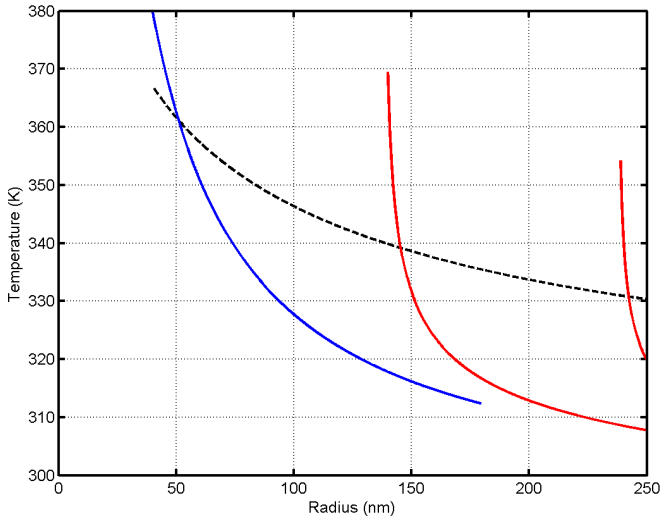

Figure D.1: Temperature profiles along the radial direction. The solid blue curve shows the initial temperature profile. The dashed black curve (phase diagram) gives the surface temperature of the vapor shell as found from the Laplace pressure. The solid blue curve crosses the dashed black curve at a radius of about 50 nm, corresponding to an overheated liquid between 40 nm and 50 nm. The solid red curves show the temperature of the liquid after it has been pushed out by the vapor shell. The part of the solid red curves above the black dashed curve at the vapor shell radius (i.e. the start of the red curves) represents excess energy partly available to feed the explosion.

negative for small radius, driving bubble expansion. Its slope, corresponding to the driving force, changes sign for 150 nm, creating an effective potential resisting expansion. In the absence of friction and heat diffusion, the maximum bubble diameter would be 230 nm. However, dissipation soon cools the surface bubble and suppresses overheating, entailing the collapse of the bubble until heating by the nanoparticle can start a new explosion.

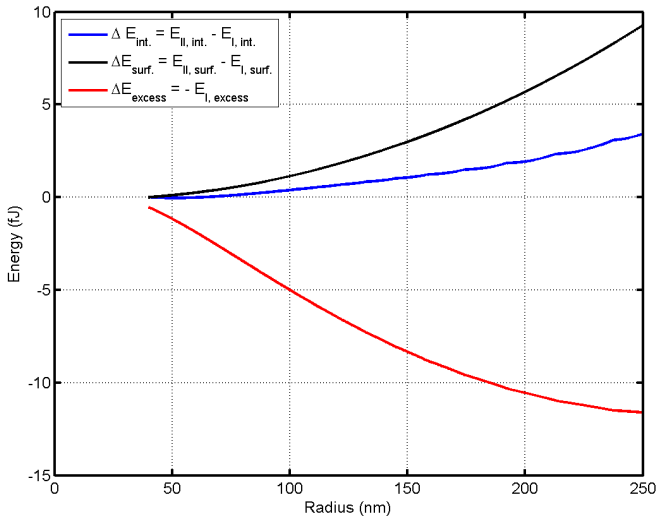

Figure D.2: Variations in internal energy (blue curve), surface energy (black curve) between state I and state II, and excess overheating energy (red curve; only half this energy is available for the bubble heating, the rest is assumed to diffuse to the cold outside liquid layers).

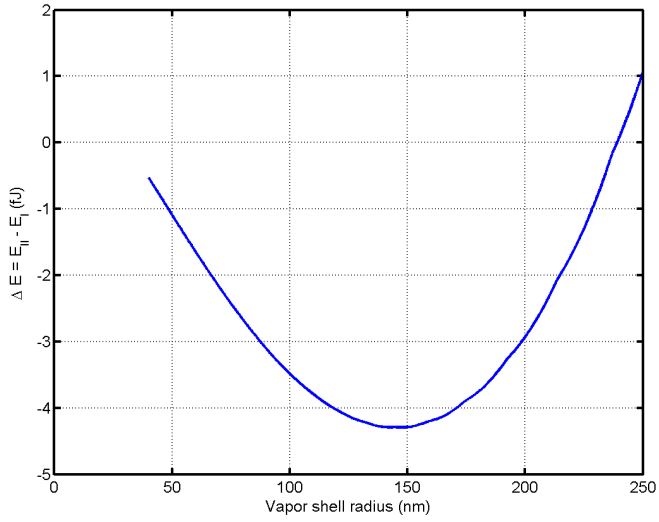

Figure D.3: The energy difference between state I and state II as a function of vapor shell radius. In principle there is enough excess energy to expand the vapor shell up to about 240 nm radius, much beyond the steady state radius of about 50 nm.

E

Analysis of delay time between two successive explosions

In order to understand the details of the delay time between two successive explosions in Chapter 3, we plot the delay time as a function of event number (red dots) as well as a histogram of the delay times (green histogram) in Fig.E.1. We attribute the strong correlation between successive delay times observed in these plots to the slow drift of the laser power, during which bubbles appeared, maintained a high repetition rate, and eventually subsided (blue trace in insert). Indeed, upon selecting a part of the data from n=800 to 2600 where laser power drift appears negligible, the data shows essentially no correlation between successive delay times. We fit the histogram of the selected delay times from n=800 to 2600 with a Gaussian distribution function as follows:

$$p(\tau) = \frac{A}{\omega\sqrt{\pi/2}} exp\left[-\frac{2(\tau-\tau_c)^2}{\omega^2}\right] \tag{E.1}$$

The fitted results are shown in Fig.3.3 (d) in Chapter 3.

To further illustrate the absence of correlation between successive delay times we simulated random delay times using the fitted Gaussian distribution. We created scatter plots of successive delay times for both the experimental data and simulation (in which correlation is absent), see Fig.E.2. By comparing the two scatter plots, we conclude that the delay time data in the central part of Fig.E.1, which we think is governed solely by the nanobubble system and not by drift of the laser power, is essentially uncorrelated.

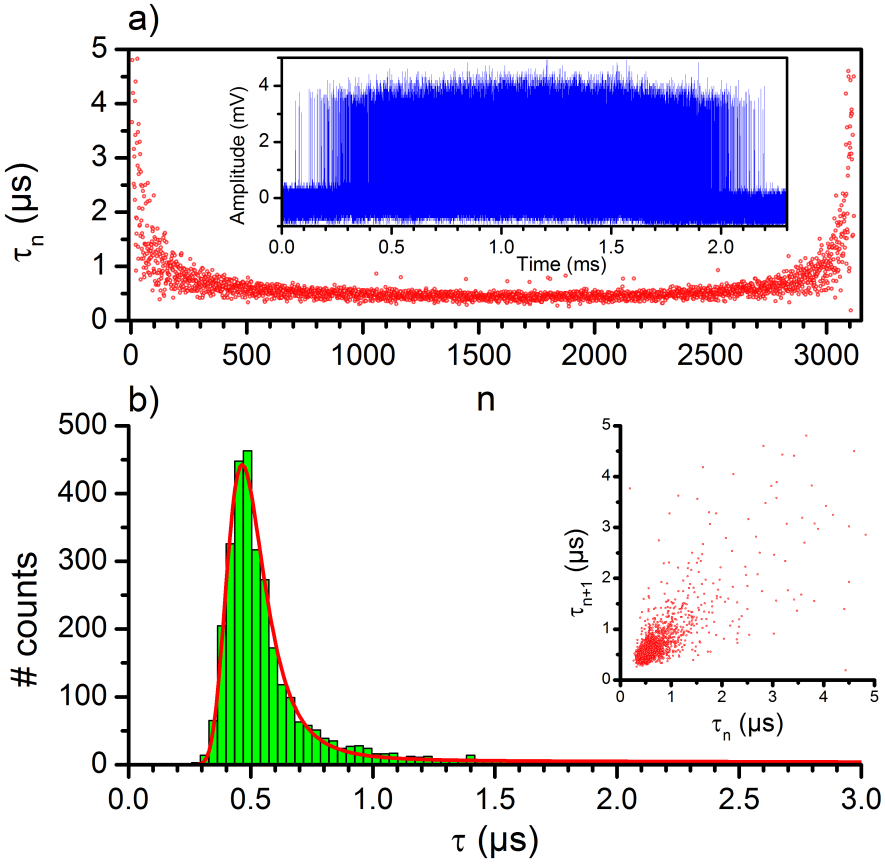

Figure E.1: a) The delay time between two successive explosions as a function of the event number n. Insert: time trace of the intensity of the scattered probe light; b) Histogram of the delay time distribution. The red line is a fitted curve. Insert: the scatter plot of τ_{n+1} and τ_n.

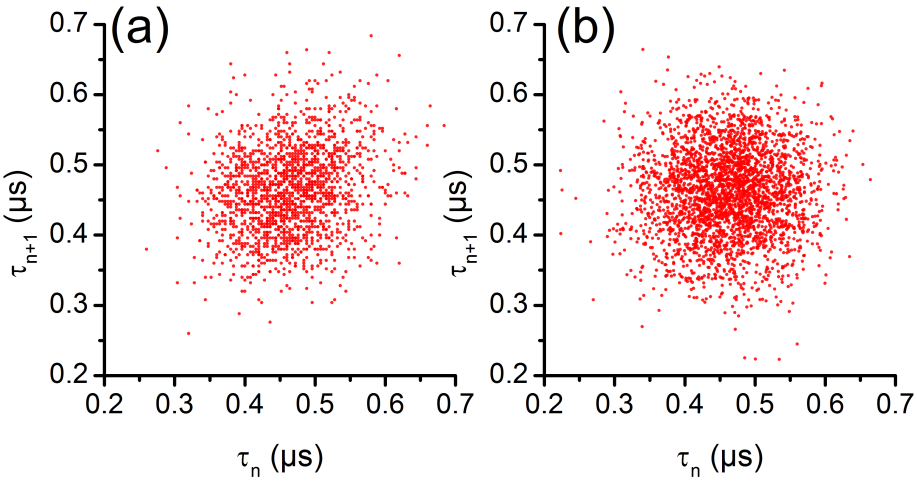

Figure E.2: a) A scatter plot of τ_{n+1} and τ_n using the experimental data; b) A scatter plot of simulation of a random succession of delay times drawn from the Gaussian distribution that is used to fit to the data from n=800 to 2600.

F

Triggering a second explosion by a sound wave

Hereafter, we briefly speculate about the mechanism of after-burst triggering by the echo. If enough energy is left in the hot liquid and in the gold nanoparticle after the first explosion, and if the returning cooled water has enough contact time with the nanoparticle to become overheated again, the system may be reloaded for a new explosion, although the temperature profile is much less extended than that before the main explosion. The heat diffusion length for a time of 150 ns, the time interval between the main bubble collapse and the arrival of the echo, is 100 nm ($D_{pentane} = 6 \times 10^{-8}$ m^2/s). For a 1 μs time it's about 2.5 times larger, 250 nm. For a long enough waiting time, a second explosion can take place, with a reduced amplitude as there is less energy stored in the overheated water to feed the expanding after-bubble. Sometimes, we even observe a third after-burst, which appears again 150 ns after the second one (see Figure F.1). This delay of 150 ns corresponds to twice the propagation time in the oil gap ($2 \times 100 \mu$m at 1350 m/s). Indeed, the first echo from the far side of the coverslip arrives 60 ns after the explosion, while the bubble just contracted and not enough energy has been transferred to the liquid yet. The echo from the objective surface arrives 150 ns later still (see Fig.3.4.c in Chapter 3) and finds enough hot water to trigger a second explosion or after-burst. In some conditions two or more afterbursts can be observed (see Fig.F.1). In these events, the nanobubble performs as an amplifier fed back on itself, producing damped relaxation oscillations. A similar phenomenon observed in water is shown in Chapter 3. However, in this latter case, the oscillation period is about 30 ns and is too short to arise from an acoustic echo. We attribute this instability to bub-

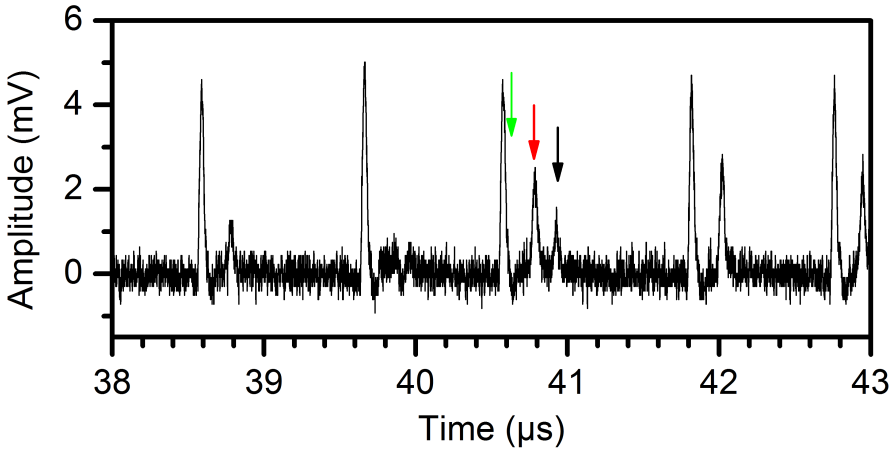

Figure F.1: The time trace including a third after-burst (black arrow). The experimental conditions are the same as Fig.3.4 in Chapter 3. The gold nanoparticle is immersed in n-pentane.

ble dynamics itself. These observations highlight the remarkable sensitivity of the nanobubble to extremely weak multiple acoustic reflections from interfaces more than 100 μm away.

G

Single-shot time trace of a persistent nanobubble

In Fig.G.1, we present a single-shot time trace of the signal of a nanobubble formed by raising the heating power above the critical value. This event is a typical one taken out of the long time trace with hundreds of explosions, shown together with the heating intensity profile. The bubble starts with a small explosion clearly visible in Fig.G.1.a, and is followed by a persistent phase before disappearing about a microsecond later when the power is decreased again. The histogram of Fig.G.1 (c) shows the jitter delays Δ between the heating pulse and the time of the explosion, taken at the mid-rising edge of the explosion signal. These delays are all positive, confirming that the explosions are all caused by the heating increase. Moreover, we see that the histogram is almost 0.5 μs broad, comparable to the spread of inter-explosion delays in the time traces in Chapter 3 with constant heating.

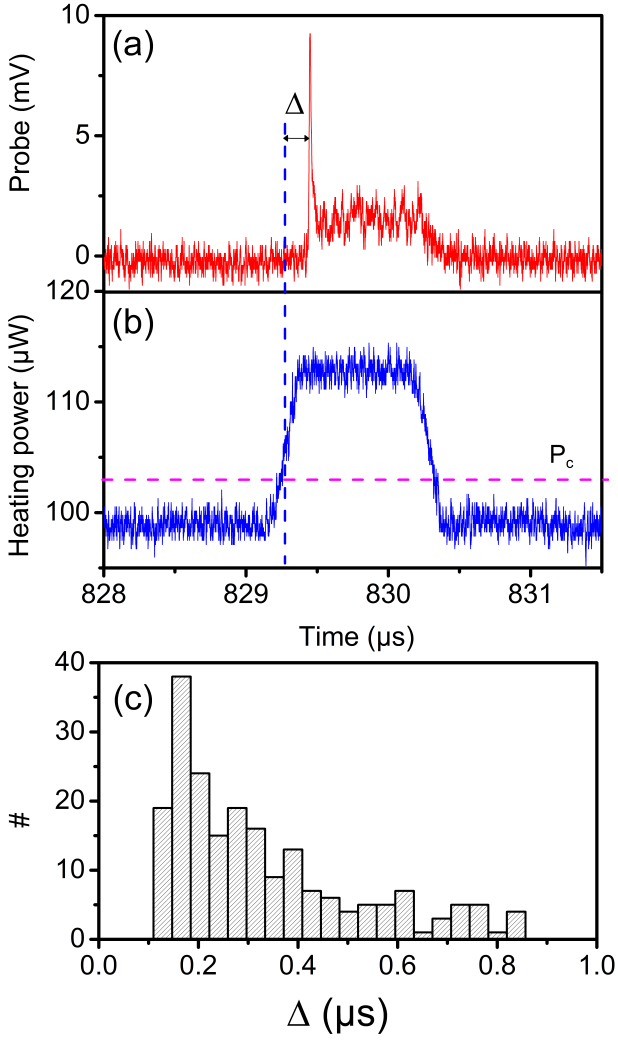

Figure G.1: The non-averaged time trace showing the improvement of nanobubble stability. a) Probe signal; b) Heating power; The heating beam is modulated by AOM, using a block pulse profile with a frequency of 100 kHz, and a duty cycle of 10% (1 μs on-time in a 10 μs period); c) The histogram of the jitter delay between the probe rise edge and heating rise edge. The gold nanoparticle is immersed in n-pentane in these measurements.

Summary

Photothermal microscopy is a highly sensitive method based on the absorption of a sample. It can be exploited to detect the energy and heat dissipation of small absorbers after optical excitation. In this thesis, we use photothermal microscopy and time-resolved pump-probe spectroscopy to study the dynamics of vapor nanobubbles around a continuously laser-heated single gold nanoparticle and the optical properties of single conjugated polymers poly[2-methoxy-5-(2-ethylhexyloxy)-1,4-phenylenevinylene] (MEH-PPV). The main observations and conclusions in this thesis are summarized as follows.

In order to gain some knowledge of vapor nanobubbles around an optically heated gold nanoparticle, we start our discussions in chapter 2 on the thermal properties of a vapor nanobubble under steady state. Based on the data from the National Institute of Standards and Technology (NIST), we calculate the minimal boiling temperature and pressure as a function of bubble size, and the temperature profile along the radial direction. Results obtained from such calculations show that boiling temperature and pressure of a vapor nanobubble shift to a much higher value compared with ambient conditions due to the large Laplace pressure at the nano scale. The temperature of the gold nanoparticle also shoots up once a vapor nanobubble forms around the particle. This is because of the small thermal conductivity of the vapor shell, which thermally isolates the particle from the contacting liquid. Because of the optical method used in our experiments, we also calculate the optical powers that are required to form a vapor nanobubble around a gold nanoparticle, and the changes in the photothermal signal due to the formation of a vapor nanobubble.

In chapter 3, we use photothermal microscopy to investigate the dynamics of vapor nanobubbles around a continuously laser-heated gold nanosphere, with time resolution from millisecond to nanosecond. We observed a number of interesting phenomena such as explosive formation of vapor nanobubbles, instability of vapor bubbles under constant heating and echo-triggered explosions. We speculate on the mechanism of bubble instability under constant heating, and conclude that the hot liquid layer around the particle at high heating power plays an important role. Thermal energy is stored in the hot liquid layer and superheating of the liquid above the saturation temperature is involved. We also observed that vapor nanobubbles are very sensitive to weak perturbations such as acoustic waves. Vapor nanobubbles can release acoustic

waves when they form. The released acoustic wave can be reflected by nearby interfaces and trigger new explosions. Under current experimental conditions, we showed that by engineering the intensity profile of the heating beam, it is possible to keep a persistent vapor bubble for about 1 μs.

The study of vapor bubbles shown in chapter 3 indicates that the dynamics of the vapor nanobubble is fast, typically on the timescale of nanoseconds. The rise time of vapor nanobubbles during expansion is close to the response time of our photodetector. In order to better resolve the dynamics of vapor bubbles during the initial stage, we use time-resolved pump-probe spectroscopy, in combination with continuous laser heating, to investigate the behavior of vapor bubbles with picosecond time resolution in chapter 4. Continuous-wave laser heating establishes a temperature of the particle close to the boiling threshold of liquid water, while the short pulses trigger bubble explosions. In our experiments, we observed that the optical contrast of acoustic vibrations of a single gold nanosphere is enhanced when the vapor bubble forms around the particle, and the damping of the acoustic vibration decreases, leading to longer decay times. These observations can be seen as an experimental proof that vapor bubbles can enhance the acousto-optical transduction. Our preliminary results show for the first time the detection of vapor bubbles with picosecond time resolution and on the single particle level.

The photothermal signal is related to the thermal properties of the transducing medium around the absorbers. In chapter 5, we use near-critical xenon to enhance the photothermal contrast of 20 nm gold particles. Close to the critical point, supercritical xenon exhibits large compressibility and large refractive index changes in response to small changes in temperature and pressure, and thus is expected to enhance the photothermal signal. Based on the standard data from NIST, we estimate the refractive index change of xenon over temperature and the enhancement factor in xenon under different temperatures and pressures near the critical point. We introduce a home-built pressure cell for the photothermal measurements in near-critical xenon. We experimentally characterize the enhancement factor of the photothermal signal of 20 nm gold particles in xenon at different temperatures and pressures, and compare the results with glycerol that was commonly used in our experiments. We found an enhancement of the photothermal signal up to thousand times in near-critical xenon when the temperature and pressure are optimized. We also examine the dependence of the photothermal signal on the modulation frequency in supercritical xenon, and we find a continuous increase of the photothermal signal at lower frequencies. We attribute this observation to the critical slowing down effect in the near-critical fluid.

The enhanced photothermal signal in near-critical fluid means that much

less heating (excitation) powers are required for the detection of weak absorbers. In chapter 6, we demonstrate the photothermal detection of single conjugated polymer molecules in near-critical xenon. We measure the absorption and emission of single conjugated polymer molecules simultaneously in near-critical xenon, and we get useful information such as the number of monomers in a single conjugated molecule and its apparent quantum yield. The thousand monomers in single conjugated molecules found in our measurements agree with what is expected from sample preparation. Low quantum yield and wide distribution of the absorption cross section are observed as well, which could originate from conformational heterogeneity. Further experiments will be carried out in the near future to investigate how photo-physical properties of single conjugated polymers change with matrix, molecular weight and preparation conditions.

Samenvatting

Fotothermische microscopie is een zeer gevoelige techniek gebaseerd op de absorptie van een preparaat. Het kan gebruikt worden om de energie en warmte dissipatie van kleine absorberende deeltjes als gevolg van optische excitatie te meten. In dit proefschrift gebruiken we fotothermische microscopie en tijdopgeloste 'pump-probe' spectroscopie om de dynamica van nanodampbelletjes rondom een gouden nanodeeltje en de optische eigenschappen van individuele poly[2-methoxy-5-(2-ethylhexyloxy)-1,4-phenylenevinylene] (MEH-PPV) geconjugeerde polymeer moleculen te bestuderen. De belangrijkste conclusies van dit proefschrift worden hieronder samengevat.

Om kennis te vergaren over nanodampbelletjes rond een optisch verhit gouden nanodeeltje, bespreken we in hoofdstuk 2 de stationaire toestand. Gebaseerd op de data van het National Institute of Standards and Technology (NIST), berekenen we de minimale temperatuur en druk als functie van de doorsnede van het nanodampbelletje evenals het temperatuurprofiel in de radiële richting. De resultaten verkregen uit dit soort berekening laten zien dat het kookpunt van een nanodampbelletje verschuift naar een veel hogere druk en temperatuur dan men zou verwachten onder normale omstandigheden, dit als gevolg van de Laplace-druk op nanoschaal. Bovendien schiet de temperatuur van een gouden nanodeeltje omhoog zodra er zich een dampbelletje omheen vormt. Dit komt door de lage warmtegeleiding van het dampbelletje, die het gouden nanodeeltje thermisch isoleert van de vloeistof erom heen. Omdat we optische technieken gebruiken in onze experimenten berekenen we ook het optisch vermogen dat nodig is om een nanodampbelletje rondom een gouden nanodeeltje te vormen en de verandering in het fotothermisch signaal die optreedt als gevolg van de vorming van zo'n dampbelletje.

In het daarop volgende hoofdstuk 3 gebruiken we fotothermische microscopie om de dynamica van nanodampbelletjes die zich vormen rondom continu met een laser verhitte gouden nanodeeltjes te bestuderen met een tijdsresolutie van milliseconden tot nanoseconden. We nemen een aantal interessante fenomenen waar zoals de explosieve vorming van de dampbelletjes, de instabiliteit van de dampbelletjes onder continue verhitting, en explosies die door een echo worden veroorzaakt. We speculeren over de mechanismen achter de instabiliteit van de belletjes onder continue verhitting en concluderen dat de hete laag vloeistof om het gouden nanodeeltje bij hoge verhitting

een belangrijke rol speelt. Thermische energie opgeslagen in de hete vloeistoflaag en oververhitting van de vloeistof boven de verzadigingstemperatuur spelen een belangrijke rol. Ook hebben we waargenomen dat nanodampbelletjes zeer gevoelig zijn voor kleine verstoringen zoals akoestische golven. Bij de vorming van nanodampbelletjes kunnen akoestische golven vrijkomen. Deze akoestische golven kunnen worden gereflecteerd door nabijgelegen oppervlakken en vervolgens nieuwe explosies veroorzaken. Onder de huidige experimentele omstandigheden hebben we aangetoond dat het met behulp van een speciaal ontworpen intensiteitspatroon voor de verhittingslaser mogelijk is om een nanodampbelletje gedurende 1 μs te behouden.

De studie van nanodampbelletjes in hoofdstuk 3 laat zien dat de dynamica van nanodampbelletjes zeer snel is. Typisch gaat het om een tijdschaal van nanoseconden. De stijgtijd van nanodampbelletjes gedurende de expansiefase ligt dichtbij de reactietijd van onze fotodiode. Om de dynamica van deze fase met hogere tijdsresolutie te kunnen bestuderen gebruiken we in hoofdstuk 4 tijdopgeloste 'pump-probe' spectroscopie in combinatie met continue laserverhitting om het gedrag van de nanodampbelletjes met picoseconde tijdsresolutie te onderzoeken. Continue laserverhitting zorgt voor een temperatuur van het nanodeeltje die net onder het kookpunt van water ligt, terwijl de korte laserpulsen de explosies veroorzaken. In onze experimenten observeren we dat het optisch contrast als gevolg van akoestische vibraties van een gouden nanodeeltje versterkt wordt wanneer er zich een dampbelletje vormt rondom het deeltje en dat de demping van de akoestische vibraties afneemt wat leidt tot langere vervaltijden. Deze waarnemingen kunnen worden gezien als experimenteel bewijs dat dampbelletjes de akoestisch-optische transductie kunnen versterken. Onze voorlopige resultaten laten voor de eerste keer de detectie van dampbelletjes met picoseconden tijdsresolutie zien.

Het fotothermische signaal is gerelateerd aan de thermische eigenschappen van het transductiemedium rondom de absorberende deeltjes. In hoofdstuk 5 gebruiken we xenon nabij het kritische punt om het fotothermisch contrast van gouden nanodeeltjes met een diameter van 20 nm te vergroten. Dicht bij het kritische punt heeft xenon een grote compressibiliteit en een brekingsindex met een grote temperatuur- en drukafhankelijkheid en dus verwacht men een versterking van het fotothermische signaal. Gebaseerd op standaard data van NIST, schatten we de verandering van de brekingsindex van xenon met de temperatuur en de versterkingsfactor van het fotothermische signaal voor verschillende waarden van de druk en temperatuur. We introduceren een eigengemaakte drukcel voor de fotothermische metingen in xenon nabij het kritische punt. We bepalen op experimentele wijze de versterkingsfactor van het fotothermisch signaal voor 20nm gouddeeltjes in xenon bij verschillende tempera-

tuur en druk en vergelijken deze resultaten met resultaten verkregen in glycerol dat we regelmatig gebruikten in voorgaande experimenten. We vinden versterkingen tot een factor duizend voor het fotothermische signaal in kritisch xenon onder geoptimaliseerde druk en temperatuur. We onderzoeken eveneens de afhankelijkheid van het fotothermische signaal van de modulatiefrequentie in superkritisch xenon en we vinden een continue toename van het fotothermisch signaal bij lagere frequenties. We wijzen dit effect toe aan de kritische vertraging die optreedt in de vloeistof nabij het kritische punt.

De versterking van het fotothermische signaal in vloeistoffen nabij het kritische punt betekent dat veel minder verhittingsvermogen nodig is voor de detectie van kleine absorberende deeltjes. In hoofdstuk 6 demonstreren we de fotothermische detectie van één enkel geconjugeerd polymermolecuul in bijna kritisch xenon. We meten tegelijkertijd de absorptie en emissie van individuele geconjugeerde polymeermoleculen in bijna kritisch xenon en verkrijgen zo nuttige informatie zoals het aantal monomeren in een geconjugeerd polymeermolecuul en het kwantumrendement. De ongeveer duizend monomeren die we in één geconjugeerd polymeermolecuul vinden komt overeen met wat we verwachten op basis van de preparatie van het monster. Verder nemen we een laag kwantumrendement en een brede verdeling van absorptiedoorsnedes waar die mogelijk het gevolg zijn van conformationele heterogeniteit. In de nabije toekomst zullen verdere experimenten worden uitgevoerd om vragen over de invloed van de matrix, het moleculaire gewicht en de preparatie op de fotofysische eigenschappen van individuele geconjugeerde polymeermoleculen te beantwoorden.

Curriculum Vitæ

Lei HOU was born on July 11, 1987 in Liaoning province, China. From September 2005 to July 2009, he studied at Changchun Institute of Optics and Fine Mechanics, China, and obtained his Bachelor degree in Applied Physics in July 2009. Later he enrolled in a Master project in the State Key Laboratory of Artificial Microstructure and Mesoscopic Physics at Peking University, China, under the supervision of Dr. Guowei Lu. He obtained his Master degree in July 2012 with the Master thesis titled "Preparation and sensing application of gold nanoparticles". In August 2012, he was awarded a scholarship from the China Scholarship Council and started his PhD research projects on the optical studies of vapor nanobubbles and single conjugated polymers at Leiden University, under the supervision of Prof. dr. Michel Orrit.

List of Publications

1. Q. Wang, G. Lu, **L. Hou**, T. Zhang, C. Luo, H. Yang, G. Barbillon, F. H. Lei, C.A. Marquette, P.Perriat, O. Tillement, S. Roux, Q. Ouyang, Q. Gong. *Fluorescence correlation spectroscopy near individual gold nanoparticle*, Chemical Physics Letters, **503(4)**: 256-261 (2011).

2. G. Lu, T. Zhang, W. Li, **L. Hou**, J. Liu, Q. Gong. *Single-molecule spontaneous emission in the vicinity of an individual gold nanorod*, The Journal of Physical Chemistry C, **115(32)**: 15822-15828 (2011).

3. G. Lu, **L. Hou**, T. Zhang, J. Liu, H. Shen, C. Luo, Q. Gong. *Anisotropic plasmonic sensing of individual or coupled gold nanorods*, The Journal of Physical Chemistry C, **115(46)**: 22877-22885 (2011).

4. G. Lu, W. Li, T. Zhang, S. Yue, J. Liu, **L. Hou**, Z. Li, Q. Gong. *Plasmonic-enhanced molecular fluorescence within isolated bowtie nano-apertures*, ACS Nano, **6(2)**: 1438-1448 (2012).

5. G. Lu, **L. Hou**, T. Zhang, W. Li, J. Liu, P. Perriat, Q. Gong. *Plasmonic sensing via photoluminescence of individual gold nanorod*, The Journal of Physical Chemistry C, **116(48)**: 25509-25516 (2012).

6. **L. Hou**, M. Yorulmaz, N.R. Verhart, M. Orrit. *Explosive formation and dynamics of vapor nanobubbles around a continuously heated gold nanosphere*, New Journal of Physics, **17(1)**: 013050 (2015).

7. T.X. Ding, **L. Hou**, H. van der Meer, A.P. Alivisatos, M. Orrit. *Hundreds fold sensitivity enhancement of photothermal microscopy in near-critical xenon*, (submitted)

Acknowledgements

During my PhD period, I received large support from my colleagues and friends who contributed to the results presented in this thesis. I would like to acknowledge them sincerely.

First and foremost, I would like to thank my supervisor Michel Orrit, for giving me the opportunity to study at Leiden. As a kind and patient supervisor, his insights into physics and broad knowledge across disciplines leave me a deep impression. I benefit a lot from the discussions with him.

Secondly, I am grateful to the mechanical technician Harmen van der Meer and the electronic technician Bert Crama. Without their help on the technical issues, I would not have overcome the troubles I met in the experiments. The help and the interaction with my colleagues was essential. I would like to thank two persons in particular: Dr. Peter Zijlstra and Dr. Mustafa Yorulmaz, for their help at the beginning of my research projects and the advice throughout my PhD period. I want to show my gratitude to Nico Verhart who helped me with the theoretical calculations on vapor bubbles. I thank Dr. Yuxi Tian, Prof. Ivan Scheblykin and Dr. Subhasis Adhikari, for their help with the sample preparation and helpful discussion on the conjugated polymer project. I am grateful to Prof. Edgar Groenen, Prof. Detlef Lohse and Prof. Eric Eliel who helped me improve the text of my thesis. I would like to acknowledge Henriëtte van Leeuwen for the administrative work she did for me. I am thankful to all other group members for their kind help and sharing experience. I would like to thank Dr. Qiang Wang, Biswajit Pradhan, Dr. He Meng, Ke Liu, Yujie Zhou and Dapeng Ding for inspiring discussions and sharing a fantastic time with me during my PhD period.

Last but not least, my thanks go to all my family members for their support, their understanding and endless love to me.